Ву

Seyed Mohammad H Hojjatzadeh

A dissertation submitted in partial fulfillment of the requirements for the degree of

Doctor of Philosophy

(Mechanical Engineering)

at the

UNIVERSITY OF WISCONSIN - MADISON

2023

Date of final oral examination: May 1st, 2023

The dissertation is approved by the following members of the Final Oral Committee: Lianyi Chen, Assistant Professor, Mechanical Engineering Frank Pfefferkorn, Professor, Mechanical Engineering Dan Thoma, Professor, Materials Science and Engineering

Xiaoping Qian, Assistant Professor, Mechanical Engineering

Tim Osswald, Professor, Mechanical Engineering

i

Acknowledgements

To *Rezvan* and *Sophia*, I offer my deepest gratitude for their love, support, and patience.

Rezvan, my beloved wife, has been my rock throughout my academic journey. Her unwavering support, patience, and understanding have been an immense source of comfort and strength. She has always been there for me, providing endless support, encouragement, and motivation when I needed it most. Her selfless sacrifices and tireless efforts in taking care of our family and home allowed me to devote myself fully to my research.

My little daughter Sophia, who has been the light of my life, has been a constant source of joy and inspiration. Her joyful laughter and insatiable curiosity about the world around her have reminded me of the importance of pursuing knowledge and continuous learning.

I would like to express my sincere gratitude and appreciation to my advisor, Lianyi Chen, for his invaluable guidance, support, and encouragement throughout my PhD journey. His expertise, dedication, and passion for research have been a constant source of inspiration and motivation to me.

Professor Chen's unwavering commitment to my academic and personal development has been instrumental in helping me overcome the many challenges that I faced during my PhD. His constructive feedback and insightful comments have helped me refine my research, develop my critical thinking skills, and enhance my writing abilities.

I would also like to extend my heartfelt gratitude to my committee members, Frank Pfefferkorn, Dan Thoma, Xiaoping Qian, and Tim Osswald, and for their invaluable insights, constructive criticism, and encouragement. Their feedback and suggestions helped me to refine my research, and their expertise and knowledge were instrumental in shaping the direction of my work. I am grateful for their time and effort in reviewing my work, and for challenging me to think critically and creatively. Their commitment to excellence and dedication to ensuring the quality of my research has been deeply appreciated.

Table of Contents

Acknowledgements	I
Table of Contents	ii
List of Figures	iv
List of Tables	xii
Nomenclature and Acronyms	xiii
Chapter 1: Introduction	3
1.1. Laser Powder Bed Fusion	3
1.2. Pore formation in LPBF	4
1.3. Pore Dynamics and Evolution	6
1.4. Pore and Solidification Crack Prediction	7
1.5. Objectives of This Work	9
Chapter 2: In-situ X-ray Imaging Methods and Materials	11
2.1. In-Situ Synchrotron X-ray Imaging	11
2.2. Materials and Sample Preparation	12
2.3. Image Processing using ImageJ	13
Chapter 3: Pore Formation during the LPBF process	15
3.1. Pore Formation from Feedstock Powder	15
3.2. Keyhole Induced Pore	16
3.3. Surface Fluctuation induced Pore	19
3.3.1 Mechanisms of Pore Induced by Surface Fluctuation	20
3.4. Pore Formation from Shallow Depression Zone	21
3.5. Crack Induced Pore	22
3.6. Pore Formation around the Melting Boundary during Laser Heating	24
3.7. Summary of Pore Formation Mechanisms	26
Chapter 4: Pore Dynamics and Elimination	28
4.1. Experimental Design and Methods for Studying the Dynamics and Elimination	
4.1.1 Monitoring the Dynamics of Pore Evolution and Elimination	28
4.1.2 Melt Flow Characterization to Estimate the Drag Force	29
4.1.3 Force Calculation	30
4.1.4 Multi Physics Simulation	31
4.1.5 X-Ray Micro Computed Tomography (μ-CT)	32
4.2. Dynamics of Pore Motions within Melt Pool	33

4.3. Driving Forces for Pore Motion and Elimination	34
4.4. Mechanisms of Pore Dynamics and Elimination	39
4.5. Eliminating Pores using Thermocapillary Force	41
4.6. Printing a Pore-free Part	43
4.7. Summary of Pore Dynamics and Elimination Results	45
Chapter 5: Defects Prediction during Metal Additive Manufacturing	47
5.1. Experiment Design	47
5.1.1 In-Situ X-Ray Experiment	47
5.1.2 Image Processing	47
5.1.3 Finding Peaks and Valleys	49
5.1.4 The Method to Capture Solidification Front Evolution during the LPBF Prod	ess50
5.1.5 Multiphysics Modelling	51
5.2. Pore Prediction	52
5.3. Pore Size Prediction	59
5.4. Solidification Cracking Dynamics	62
5.5. The Mechanism of Formation of a Curved Interface	65
5.6. Hot Cracking Sensitivity	67
5.7. Peak Position Matching for Crack Prediction	71
5.8. Summary of Defects Prediction during Metal Additive Manufacturing	72
Chapter 6: Conclusions of this work	74
Chapter 7: Recommendations for Future Work	78
References	80
Appendices	93
Appendix A - Copyright Permissions	93
Appendix B – Extended Data	94

List of Figures

Figure 1. Schematic of in-situ high-speed X-ray imaging experiments. (a) Laser scanning.
(b) Stationary laser melting
Figure 2. Image processing to reveal the melt pool boundary. (a) the original X-ray image.
The result of image processing using (a) first (b) second and (c) third method. The X-ray
image is captured during the LPBF process of Al6061 using laser power of 416 W, and
scan speed of 0.4 m/s
Figure 3. Pore formation from feedstock powders. (a-d) X-ray image sequence showing
the transfer of pores from the powder bed into the melt pool and then, residing in the
solidified track during the LPBF process at 310 W laser power and 0.6 m/s scan speed.
Traced pores in the powder layer are indicated by orange arrows in the first frame (to).
The transfer path of pores from the powder bed to the melt pool is indicated by a yellow
dotted arrow in (c). The substrate material is Ti-6Al-4V
Figure 4. Keyhole-induced pore. (a-d) Pore formation due to keyhole collapse, during the
LPBF process of AlSi10Mg at $520\mathrm{W}$ laser power and $0.45\mathrm{m/s}$ scan speed. (e-h) Creation
of a ledge and resulting pore at the vapor depression rear wall during the LPBF process
of Ti-6Al-4V at 520 W laser power and 0.3 m/s scan speed. (i-I) Pore formation when the
laser was switched off at the end of the track during the LPBF process of Al6061 at 470
W laser power and 0.4 m/s scan speed
Figure 5. Pore trapped by surface fluctuation of molten pool. (a-d) Dynamic X-ray images
showing the pore trapping mechanism by protrusion on the surface of the melt pool during
the laser melting of Ti-6Al-4V. (e-h) Dynamic X-ray images showing the pore trapping
mechanism by droplet during the laser melting of Ti-6Al-4V. Trapped pores are indicated
by dotted circles. The laser power was 365 W and the laser scan speed 0.4 m/s 20 $$
Figure 6. The mechanism of pore induced by surface fluctuation. (a-c) Dynamic X-ray
images showing the pore trapped by surface protrusion during laser melting of Ti-6Al-4V,
at a laser power of 365 W and the scan velocity of 0.4 m/s. (d) Mechanism of pore induced
from surface ripple. (e-h) Schematic showing the mechanism of gas entrapment under an
impact of a droplet onto a liquid pool21

Figure 7. Pore formation due to depression zone fluctuation in transition regime. (a-c)
Dynamic X-ray images showing g pore formation due to depression zone fluctuation
during laser melting of Al6061 bare plate at 520 W laser power and 0.5 m/s scan speed.
The pore is indicated by a dotted circle
Figure 8. Pore formation from cracks. (a) X-ray image showing Al6061 substrate and a
crack. (b-d) Dynamic X-ray images showing the pore formation from the crack. The cracks
are delineated by red arrows in (a). In (d), spherical pores are indicated by white arrows.
The laser power was 470 W and the laser scan speed was 0.4 m/s
Figure 9. SEM image showing the top view of the sample with a crack after laser melting.
The material is Al6061. The laser power was 310 W, and the laser scan speed was 0.4
m/s. Red arrows indicate the crack propagation on the top surface24
Figure 10. Pore formation at the melting boundary. (a-c) Ultra-fast (frame rate of 2 MHz)
X-ray image sequence of laser melting of aluminum bare substrate showing the pore
formation and growth along the melting boundary (indicated by red dotted line) at 470 W
laser power and 1 m/s scan speed. (d-f) Ultra-fast (frame rate of 2 MHz) X-ray image
sequence of laser melting of aluminum bare substrate showing the pore formation and
growth along the melting boundary (indicated by red dotted line) at 470 W laser power
and 0.5 m/s scan speed. (g) Pore formation along the melting boundary and (h, i) pore
trapping after the laser was switched off for stationary laser melting at 520 W laser power.
Nucleated pores are indicated by dotted circles. The material was aluminum (99.99%).
Figure 11. The summary of pore formation mechanisms observed in this work. The first
row depicts the pore formation induced by the material and second row shows those
induced by processing conditions
Figure 12. In-situ characterization of pore dynamics during LPBF process. (a) Schematic
illustration of the in-situ high-speed X-ray imaging experiment. (b) Representative cuboid
(300 μm × 200 μm × 200 $\mu m)$ reconstructed from X-ray computed tomography data
showing the size and distribution of pores inside an additively manufactured AISi10Mg
plate. (c) Representative single-pulse X-ray image revealing micro-pores as well as the
melt pool and depression zone beneath the surface of the powder bed (laser power of
360 W, scan speed of 1 m s-1 and laser beam diameter (D4 σ) of 100 μ m). The boundaries

of the men poor and the depression zone are indicated by a write dashed line, and the
position of the laser is indicated by a red arrow. The scale bar in (c) is 50 μm 29
Figure 13. Dynamic pore motions within melt pool. (a-d) X-ray images showing pore
dynamics during the LPBF process. The thickness of powder layer is 100 μm. (e-h) X-ray
images showing pore dynamics during laser melting of a bare substrate. Dotted arrows
indicate the future trajectories of the pores (time \leq 30 μ s), while solid arrows mark the
history of pore trajectories (after time = 150 μs). Pores follow circular patterns at the
circulation domain (a, e), while pores in the laser interaction domain move toward
depression zone and escape from the melt pool (d, h). In the transition domain (b, c, f and
g), pores exhibit irregular moving behavior, sometimes moving toward the melt pool
surface and escaping (c, g), and sometimes circulating in the melt pool (b, f). The laser
beam diameter (D4 σ) is 100 μm , the laser power is 360 W, and the scan speed is 1 m
s ⁻¹ . All scale bars are 50 μm34
Figure 14. Driving forces for pore motion and elimination. (a-c) X-ray images showing
trajectories (indicated by red arrows) of the tracing particles (tungsten microparticles,
marked by white dotted circles), which indicate the melt flow at the circulation domain (a)
transition domain (b) and laser interaction domain (c) inside the melt pool during the LPBF
process. (d) Temperature gradient inside the melt pool during LPBF process, obtained by
multiphysics modeling with laser processing parameters the same as the in-situ
experiments in Figure 13. The magnitude and direction of temperature gradient are
indicated by color and black arrows, respectively. The white arrow in d indicates the
temperature gradient increases from the solid-liquid interface (melting front) to the
depression zone front wall. (e) Ratio of thermocapillary force (F_t) to drag force (F_d) for a
pore with a diameter of 10 μ m. In (a-c), the laser power is 360 W, the scan speed is 1 m/s
and the thickness of powder layer is 100 μm. Scale bars in (a-c) are 50 μm36
Figure 15. The mechanism of pore movement due to the temperature gradient inside the
liquid. Solid red arrows indicate the direction of pore movement, while black dotted arrows
indicate the direction of liquid. The color map illustrates the temperature gradient inside
the liquid37
Figure 16. Increase of acceleration as pores move toward depression zone wall. a

Variation of temperature gradient, G, from the melting front to the depression zone wall

(indicated by the white arrow in Figure 14d). The temperature gradient increases towards the depression zone wall. (b) Velocity, as a function of time, as pores move toward depression zone wall. (c) Acceleration, as a function of time, as pores move toward depression zone wall. The data in (b and c) are collected during laser melting of an Figure 17. Mechanisms of pore dynamics and elimination. Schematic illustration showing the dynamics of pore motion and pore elimination within the melt pool during the LPBF process.......40 Figure 18. Force analysis. Comparison of drag force, buoyant force and thermocapillary force at the circulation domain (a) and the laser interaction domain (b) for the pore size range studied in this work. (c-d) Forces as a function of pore dimeter. The critical pore size for buoyant force to overcome drag force is 2.5 mm at the circulation domain (c) and 11 mm at the laser interaction domain (d), which are even larger than the size of a typical melt pool in the LPBF process. The critical pore size for the buoyant force to exceed the thermocapillary force is even larger, requiring a pore size of at least 10 mm in the Figure 19. Eliminating pores using thermocapillary force. (a-d) Dynamic X-ray images showing elimination of pores in feedstock powders. The thickness of powder layer is 100 µm. In (b), w and d indicate the depression zone width and depth, respectively, and t represents the thickness of the liquid layer around the depression zone. (e-h) Dynamic X-ray images showing elimination of pores in the previously built layer. Traced pores are indicated by dotted circles. Pore moving trajectories are indicated by yellow arrows. The melt pool and depression zone boundaries are outlined by green and white dashed lines, respectively. Time indicated in the picture represents the time after laser turning on. The powder and substrate are Ti-6Al-4V. The laser beam diameter (D4 σ), laser power, and scan speed are 75 µm, 210 W, and 0.6 m/s, respectively. All scale bars are 50 µm..... 43 Figure 20. Pores distribution inside AlSi10Mg powders and as-printed AlSi10Mg samples. (a) One slice from x-ray tomography data showing pores inside AlSi10Mg powders. (b-c) Representative reconstructed x-ray computed tomography cuboids (300 μm × 200 μm ×200 μm) showing the size and distribution of pores inside the as-printed AlSi10Mg sample built by commercial machine (Renishaw AM250) (b) and our

customized laser powder bed system using parameters designed based on
thermocapillary force driven pore elimination mechanism (c). b and c share the same
scale bar44
Figure 21. Workflow for automatic detection of the keyhole and pore and the prediction
based on peak position matching. The Ti-6Al-4V experiment was cited from [72] 49
Figure 22. Measured keyhole geometries using image processing. The results of
measurement for (a) keyhole depth, (b) width, (c) aspect ratio and (d) area49
Figure 23. Solid-liquid interface evolution and method for determining the solidification
rate. (a) Original X-ray image showing the keyhole and solid liquid interface during LPBF
process of Al6061. (b)The result of image processing to reveal the melt pool boundary.
(c) The result of curve fitting on the tracked solid-liquid interface using polynomial
equation. (c) Higher magnification of (b) showing the growth trajectories of the solid-liquid
interface from to to t351
Figure 24. Defect Prediction during LPBF Process. (a) X-ray images capturing the
keyhole dynamics during pore formation, showing the transition of the keyhole aspect
ratio (depth/width) from a valley to a peak between time t_1 and t_3 . (b) Application of the
peak position matching approach for predicting the occurrence of pores and cracks during
the LPBF process. In (a,t_2) , the yellow-purple colors indicate the image processing using
k-means clustering method that is overlaid on the original X-ray image. The experiment
in (a) is the LPBF process of Ti-6Al-4V under laser power of 382 W, scan speed of 0.5
m/s, beam size of 90 $\mu m,$ and a frame rate of 50 kHz, which was cited from Zhao et al.
(videos S1) [72]
Figure 25. Keyhole geometry and peak position matching for pore prediction.
Quantification of keyhole (a) depth, (b) width and (c) aspect ratio; (d) Implementation of
the peak position matching. The in-situ X-ray experiment was captured during the LPBF
process of Al6061, under a laser power of 501 W, scan speed of 0.4, beam size of 90
um, and frame rate of 140 kHz. The frames in which pores are observed are indicated
with red color in a-c. In (d), the arrows indicate the frames in which pores are predicted
to form based on peak position matching54
Figure 26. Pore prediction based on peak position matching. (a) X-ray frames of the
predicted pore moments based on peak position matching; (b) X-ray frames on which the

pore is observed. Pores are indicated by the arrows in the X-ray images. The experiment
was captured during the LPBF process of Al6061, with a laser power of 501 W, scan
speed of 0.4, beam size of 90 um, and frame rate of 140 kHz. All scale bars are 50 µm.
Figure 27. (a) In-situ X-ray images showing the frames where pore formation is predicted
by peak position matching. (b) In-situ X-ray images showing the frames where pores are
visible. The material used is Al6061, with laser power of 261 W, scan speed of 0.4 m/s,
beam size of 50 $\mu m,$ and frame rate of 140 kHz. The arrows in (b) indicate the pores. The
scale bar is 50 µm
Figure 28. The accuracy of pore prediction based on peak position matching. (a)
Precision and (b) recall values as function of frame rate calculated for different average
keyhole depth (d) in Al6061 experiments
Figure 29. Pore formation and reattachment to the keyhole when the keyhole is deep. In
this process, the keyhole pore is formed at $t=7~\mu s$ and then merges into the keyhole from
t=14 to t=21 μ s. The pore starts to detach from the keyhole again at t=49 μ s. The
experiment was captured during the LPBF process of Al6061 with a laser power of 600
W, scan speed of 0.4 m/s, beam size of 50 $\mu m,$ and frame rate of 140 kHz. The scale
bars in all images are 50 µm58
Figure 30. Pore prediction using peak position matching for Experiment S3. (a) In-situ X-
ray images displaying the predicted pore frames based on peak position matching, and
(b) in-situ X-ray images of the frames in which the pores are observed within the track.
The in-situ X-ray experiment was conducted during the laser melting of Ti-6Al-4V at a
laser power of 382 W, scan speed of 485 mm/s, beam size of 100 μm , and a frame rate
of 50 kHz. The data was sourced from Zhao et al. [72]. In panel (b), the orange arrows
show the pores59
Figure 31. (a) The dynamic X-ray images showing the evolution of the keyhole from its
minimum aspect ratio to the peak aspect ratio. The change in (b) keyhole depth, (c)
keyhole aspect ratio, and (d) in keyhole topmost width and length (l) of the cavity at the
bottom prior to pore formation. Blue arrows denote the approximate location of the
traveling recoil pressure. The black arrows in b and c show the peak position matching

for the pore formation. The experiment is the LPBF process of Ti-6Al-4V at laser power
of 365 W, scan speed of 0.4 m/s and the frame rate of 140 kHz61
Figure 32. Relationship between pore diameter and Peak to Valley ratio (PVR) for
keyhole pore instances observed during the in-situ X-ray experiment of LPBF process of
(a) Al6061 and (b) Ti-6Al-4V as predicted by our analysis62
Figure 33. The dynamics of solid-liquid interface during solidification cracking. (a) X-ray
image shows the formation of solidification crack after the solid-liquid interface has moved
away from the crack initiation site. (b) Evolution of solid-liquid interface using the ninth-
order polynomial fit. (c) Solidification velocity along P ₁ . (d) Solidification velocity along P ₁
and keyhole depth fluctuations. (e) Solidification velocity along P1 and keyhole aspect
ratio. (f) Melt pool depth as a function of time. The experiment is the LPBF process of
Al6061 at laser power of 468, scan speed of 0.4 m/s, laser beam size of 90 μ m, and frame
rate of 50 kHz63
Figure 34. The variation of solidification velocity along P2-P5 and fluctuation of keyhole
depth over time. The highlighted area in pink shows the time when solidification velocity
is not harmonious with the keyhole fluctuations, while the area highlighted in yellow shows
the harmony between keyhole and solidification65
Figure 35. (a) The average keyhole depth (b) the average melt pool depth, and (c) the
difference between the melt pool depth and keyhole depth. The in-situ X-ray experiment
is the same experiment shown in Figure 3366
Figure 36. FLOW-3D multiphysics simulation of the LPBF process of Al6061 when the
keyhole depth changes from shallow to deep. (a-d) The melt flow streamlines (shown in
white lines) and the magnitude (shown with colormap) within the melt pool. (e-h) The
direction and magnitude of the melt flow (indicated with white arrows) and amount of solid
fraction (indicated with color map) at different locations in the melt pool. The size of the
arrows in e-h corresponds to the magnitude of the melt flow velocity. The laser parameters
used for simulation and in-situ X-ray experiments were laser power of 368 W, scan
velocity of 0.4 m/s, and beam size of 90 µm66
Figure 37. Schematics of the RDG model showing the formation of hot tear in between
columnar dendrites. The figure in [83] was used as a basis for reproducing this figure. 69

Figure 38. The formation of pore near the crack area captured during the in-situ	X-ray
experiment of the LPBF process of Al6061, under a laser power of 501 W, laser	scan
speed of 0.4 m/s, beam size of 90 um, and frame rate of 140 kHz.	72

List of Tables

Table 1. Pore volume fraction of as-printed AlSi10Mg reported in the lite	erature 45
Table 2. The results of precision and recall for LPBF process of Ti6Al4	√. S1, S2 and S3
were cited from [72]	59

Nomenclature and Acronyms

3D = Three-dimensional

AM = Additive manufacturing

LPBF = Laser powder bed fusion

SEM = Scanning electron microscope/microscopy

FPS = Frame per second

RDG = Rappaz-Drezet-Gremaud

Abstract

Laser powder bed fusion (LPBF) additive manufacturing (AM) is a 3D printing technology that can create parts with complex geometries in a layer-by-layer manner, which is impossible with conventional manufacturing methods. Currently, LPBF is increasingly applied in various industrial sectors, including biomedical, aerospace, and defense. However, the formation of defects, such as pores and cracks, in LPBF-printed parts has hindered its wider industrial application. Pores and cracks can weaken the mechanical performance of the parts, particularly under cyclic loadings. As the metal substrates used in LPBF are optically opaque, in-process probes of subsurface phenomena, such as vapor depression geometry, melt pool dynamics, and defects formation and evolution, via conventional optical and acoustic methods are somewhat limited and indirect.

To address this challenge, our research utilized the in-situ high-speed, high-energy, and high-resolution X-ray imaging to study the dynamics of defects formation and evolution during the LPBF process. Chapter 3 explores different mechanisms of pore formation during the LPBF by performing in-situ X-ray imaging on different substrate materials and under different laser processing conditions. Chapter 4 investigates the different mechanisms and driving forces for pore motion and elimination during the LPBF process. This quantification resulted in the discovery of a new mechanism induced by temperature gradient for rapid pore elimination from the substrate and powder bed. Chapter 5 presents a novel approach for predicting the formation of pores and solidification cracks by analyzing changes in the keyhole geometry. For the first time, it also establishes a relationship to determine the size of pores based on changes in keyhole geometry.

Furthermore, new insights on the mechanism of solidification cracking will also be provided. Overall, this research provides valuable insights into the dynamics of defect formation and evolution during the LPBF process, as well as addressing the challenge of defect prediction. Moreover, these findings can serve as a guide for process monitoring and optimization to achieve defect-free parts, while also providing insights that can be applied to the development and validation of high-fidelity simulation models.

Chapter 1: Introduction

This chapter discusses the principles of laser powder bed fusion (LPBF) additive manufacturing (AM) process and reviews the state-of-art in the studies of pore formation and pore evolution. In the end, it presents the objectives of this work, aiming to address the challenges met by the previous research.

1.1. Laser Powder Bed Fusion

Laser powder bed fusion (LPBF) additive manufacturing relies on a successive melting of a thin layer of powders to produce a 3D part in a layer by layer [1,2]. In a typical LPBF process, a layer of powder with a thickness of around 50-100 µm is selectively scanned by a laser beam. The laser melts the powder particles and the top layer of the substrate, creating a melt pool with a typical width of around 200 µm [3]. The subsequent cooling of the molten material results in a new layer of solid metal. The LPBF process involves extremely rapid heating and cooling rates, which give rise to complex dynamics and transient phenomena. These can include the melting and partial vaporization of powders, flow of molten metal, powder ejection and redistribution, rapid solidification, and non-equilibrium phase transitions [4,5]. The LPBF technology has become increasingly popular in recent years due to its ability to fabricate complex parts while minimizing material waste and time to market, thereby reducing costs and increasing efficiency in the manufacturing industry [6].

While LPBF technology offers unique advantages in directly fabricating parts with complex geometries, the presence of pores and cracks can still pose significant challenges that impact the performance of the final product, including its fatigue life [7]. Extensive research efforts have advanced the understanding and control of the defects

[8–10]. However, how these defects are formed under different processing conditions and then how they evolve within the micron-sized melt pool have remained obscure because the relevant spatiotemporal scales of the defect formation require subnanosecond temporal resolution, micrometer spatial resolution, and megahertz frame rates. That necessitates the implementation of in situ X-ray tools to probe subscale dynamics of the melt pool and defects in real time.

1.2. Pore formation in LPBF

A Pore is a major defect in the parts manufactured by the LPBF process. Since a pore can be a strong stress riser, it can lead to parts failure, especially under fatigue loading [11]. The size, morphology, and the location of pores are the primary variables that affect mechanical performance of a printed part. For example, additively manufactured specimens, with a higher pore density, have shorter fatigue lives and pores closer to the surface have a more detrimental effect on fatigue performance [12]. Currently, hot isostatic pressing (HIP) is used to reduce or eliminate pores. However, the pores on the surface cannot be eliminated by HIP and the gas pores can reopen and regrow when the sample is subjected to subsequent heat treatment [13,14]. To prevent the formation of pores in the LPBF process, it is important to identify the root causes of pore formation and take measures to mitigate their formation.

Researchers have conducted extensive studies to gain a better understanding of the mechanisms that contribute to pore formation during the LPBF process. To achieve this, they have employed various post-characterization techniques, including cross-section analysis [9], bulk density measurements [15], and X-ray computed tomography [16]. These techniques enable researchers to analyze the as-printed samples and gain insights

into the spatial distribution and morphology of the pores inside the parts after being built. A number of possible pore formation mechanisms in LPBF process have been identified by these characterization techniques, which can be loosely categorized into raw materials-related pores and laser processing-related pores [14].

A frequent cited source of raw materials-related pore is the gas (usually argon) trapped in the powder during the powder manufacturing process. A common type of processing-related pore is induced by the depression zone. The depression zone is a vapor cavity that forms under the laser spot due to the recoil pressure induced by the localized vaporization [17]. At high energy density (high laser power and low scan speed), the depression zone becomes deep and narrow. When the aspect ratio (depth/width) of the depression zone is over 0.5, it is called a keyhole. During laser melting, the keyhole easily becomes unstable and fluctuates to create pores [18].

Even though a lot of valuable information has been obtained from the post characterization techniques, further understanding of the subscale dynamics, including pore formation needs observation of the process in real time. The direct observation of the subsurface phenomena necessitates implementation of in-situ techniques, because the metals substrates used in LPBF are optically opaque and the pores form and move very fast [19].

Recent in situ X-ray studies focused on LPBF process have substantiated the dynamics of spatter [20], pore [21], melt flow [22], melt track evolution [23], fracture [24], solidification and phase transformation [25] in real time. Studies of pore formation mechanisms in LPBF AM using in-situ X-ray have invested much effort on high speed phenomena related to keyhole dynamics and keyhole pore formation [25–28]. It has been

revealed that the keyhole can become unstable and can induce pores in the melt pool when the laser is running [26], at the end of the track when the laser is switched off, and at the laser turning point [25–27]. Pore transferred from the feedstock powder has been also recently probed using X-ray imaging in real time [29], where Marangoni convection was highlighted as the driving force for pore entrainment from the feedstock powder to the melt pool. To develop further fundamental insight into pore formation mechanisms during the LPBF process, the next and critical step is the application of state of art in-situ X-ray imaging as a diagnostic tool to identify all other mechanisms by which pores form during laser-metal interaction.

1.3. Pore Dynamics and Evolution

During the laser melting, pores in the melt pool cannot be effectively eliminated by buoyant force [30], a commonly known mechanism that eliminates pores from liquid [31], because the high drag force, that is induced by the strong melt flow in the LPBF process, traps the pores within the melt pool [32]. Thus, pores have been ubiquitously observed in as-printed parts [4]. In addition, it is very challenging to completely eliminate pores in the printed parts by post processing of parts. For example, the hot isostatic pressing (HIP) cannot close the surface pores [11]; and the gas pores closed by HIP can reopen and grow during subsequent heat treatment [33].

Understanding the dynamics of pores in the melt pool during printing is crucial to produce high-quality, as-printed parts with very low or zero porosity in the LPBF process. By gaining insights into how pores move and eliminate, necessary measures can be taken to prevent their formation during the printing process. This can help to produce parts with

very low or zero porosity, which is essential for ensuring their optimum mechanical performance.

1.4. Pore and Solidification Crack Prediction

Despite the manufacturing advantages offered by LPBF AM, the repeatability and reliability of printed parts are still limited due to the formation of structural defects in the as-printed parts. These defects are preventing the technology from being adopted for a much wider range of applications. Despite extensive process optimization to control defects, the formation of defects in LPBF is liable to occur due to the stochastic and extreme thermal conditions intrinsic to the LPBF process. These conditions can instigate transient thermal conditions and complex structural dynamics [2]. Predicting the formation of defects is therefore essential in overcoming the technical challenges before LPBF can reach its full potential as a disruptive manufacturing technology. It is also vital for developing in-situ monitoring tools that eliminate the need for costly and time-consuming post-qualification procedures.

In the laser powder bed fusion (LPBF) process, high-energy density laser (using high laser power and slow scan speed) is often employed to increase the process build rate. However, excessive laser energy density can result in the formation of a narrow and deep vapor depression, known as a keyhole, which can lead to porosity formation during the printing process. This porosity is commonly referred to as a keyhole pore and is caused by perturbative keyhole oscillation under unstable conditions [34]. By predicting the keyhole pore generation in real-time, we can anticipate the need for local variations during the build process and adjust the process parameters accordingly.

The solidification cracking or hot tearing is another common defect phenomenon observed in a number of metallic systems such as aluminum [35] and nickel-based alloys [36]. The hot cracking sensitivity of the metal is related to both the material composition and processing parameters. Alloys that are prone to solidification cracking tend to have a large mushy zone, which means they have a broad solidification range between the liquidus and solidus temperatures. At high fractions of solid, there is a sharp turnover in the solidification curves, often due to the presence of strengthening solute that partitions into the liquid during solidification. During solidification, thermal shrinkage can occur and cause tearing and cavitation in thin films of interdendritic liquid present at high solid fraction [37]. Temperature gradient and solidification growth rate are two key factors that contribute to solidification cracking during laser processing. These factors are primarily controlled by the laser processing condition [38]. Accurate quantification of the solid-liquid interface velocity during the LPBF process, especially near the location of the crack, is crucial for understanding the underlying mechanisms of solidification cracking. This information is also vital for developing prediction models that can anticipate the occurrence of solidification cracking based on laser processing conditions.

Currently, optical [39] and acoustic sensors [40] are widely used to monitor the melt pool and keyhole from the top. Post-data analysis approaches, such as machine learning, have been developed to correlate melt pool process signatures with defects. However, these approaches can only identify defect formation after it has occurred and often require a significant amount of data over a prolonged time window. Despite their potential, predicting defects using melt pool signatures before they form inside the structure is not yet deterministic.

1.5. Objectives of This Work

In this work, in-situ high-speed high-energy high-resolution X-ray imaging technique with high temporal and spatial resolution will be used to address the challenges encountered by previous research to characterize the process dynamics during the LPBF process of metals. Chapter 3 will give an insight into pore formation mechanisms by direct observation of the LPBF process. We reconfirm three pore formation mechanisms, i.e., pore transferred from feedstock powder and different types of keyhole pore and pore formation along the melting boundary during laser melting from vaporization of a volatile substance or an expansion of a tiny amount of trapped gas, which were revealed by previous in-situ X-ray studies. For the first time ever, three new pore formation mechanisms: (1) pore trapped by surface fluctuation, (2) pore formation due to depression zone fluctuation, when the depression zone is shallow, (3) pore formation from crack will be uncovered. The findings of this study could inspire and guide the 3D printing community to develop new approaches to reduce pore density and improve part reliability. Some laser processing conditions investigated in Chapter 3 (i.e., high energy density laser beam is applied on a bare substrate) are similar to the situations in high energy density laser welding. Thus, the results obtained also have implications for deep penetration laser welding.

Chapter 4 will present mechanisms of pore dynamics in the melt pool and uncovers a mechanism for effectively eliminating pores in 3D printing of metals by synergistically combining in-situ experiments and multiphysics modeling. The pore elimination mechanism uncovered in Chapter 4 also has implications for a broad range of research and engineering fields where pore evolution is important and a temperature gradient

exists, such as laser polishing [41], laser cladding [42], welding [43], melt spinning [44], reactions in nuclear reactors [45], and chemical reactors [46].

In Chapter 5 we will utilize high-speed in-situ X-ray imaging with a frame rate of up to 140 kHz to demonstrate a novel approach for early prediction of keyhole pore and solidification crack during the LPBF process. This approach is based solely on keyhole geometry, depth, and width, and can precisely predict the occurrence of keyhole pores and cracks. Moreover, we will show that this approach is capable of predicting the size of pores, representing the first time such an achievement has been demonstrated.

The research findings shed light on the mechanisms and dynamics of Laser Powder Bed Fusion (LPBF), which can provide critical insights for developing defect-free 3D printing parts and unlocking the full potential of this technology. Additionally, the experimental results are vital for creating high-fidelity computational models, which can further advance the field of additive manufacturing.

Chapter 2: In-situ X-ray Imaging Methods and Materials

This chapter provides an overview of the general experimental methods utilized in this research work, including the in-situ X-ray imaging setup, materials and general image processing techniques.

2.1. In-Situ Synchrotron X-ray Imaging

High-speed, high-resolution X-ray imaging, located at beamline 32-ID-B, Advanced Photon Source, Argonne National Laboratory, was used in this work to study pore formation and evolution during the LPBF process in real-time. The experimental setup is schematically shown in Figure 1.

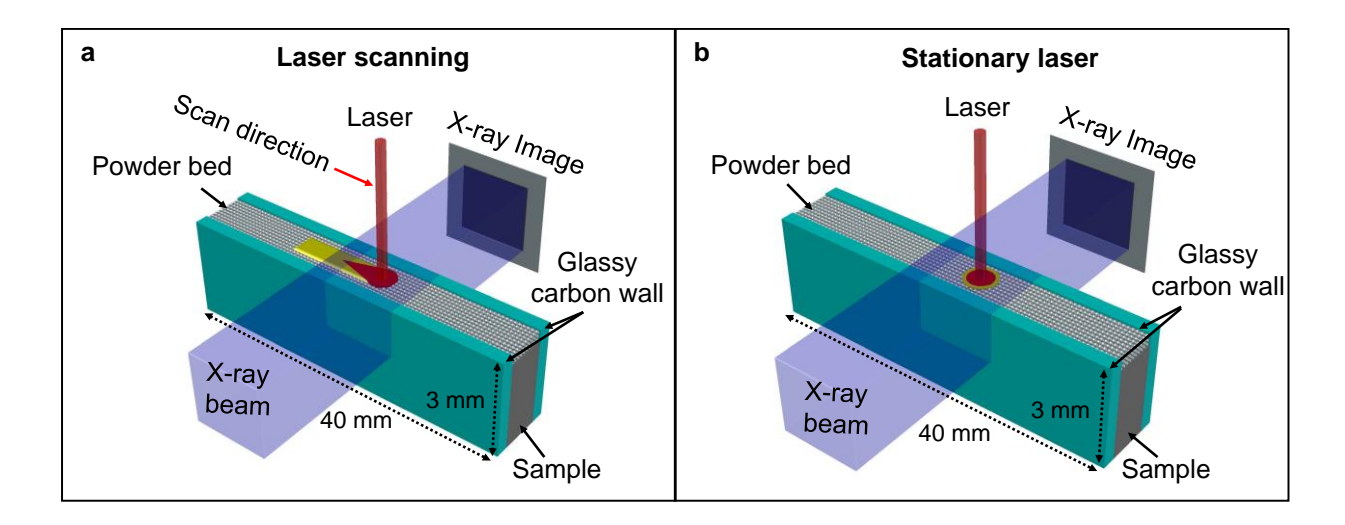


Figure 1. Schematic of in-situ high-speed X-ray imaging experiments. (a) Laser scanning. (b) Stationary laser melting.

The X-ray imaging system is composed of a miniature powder bed system clamped between two glassy carbon walls. A pseudo pink X-ray beam, with 1st harmonic energy at (24.7~25.3) keV, was used to penetrate through the metal sample for imaging. The transmitted X-ray beam was captured by a detection system downstream, where the X-ray signal was converted into a visible light image, and then recorded by a high-speed

camera with a 10x objective lens. A continuous-wave (CW) ytterbium fiber laser (IPG YLR-500-AC, IPG Photonics, Oxford, USA, wavelength of 1070 nm, maximum output power of 520 W) and a galvo scanner (IntelliSCANde 30, SCANLAB GmbH., Germany) were integrated to perform single track laser melting (when scan speed was perpendicular to X-ray beam [Figure 1a] and stationary laser melting [Figure 1b] on both powder bed and bare substrate under various laser powers (from 100-520 W) and scan speeds (0.3-1.5 m s⁻¹). The experiments without metal powder ensured maximum clarity for imaging near the surface. The experiments were conducted using a laser beam diameter ($D4\sigma$) ranging from 90 to 100 µm.

The nominal spatial resolution of the image was 2 μ m/pixel. For more details about the in-situ X-ray imaging experiment, we refer the readers to the previous publications [20,21,25,47]. In this work, a recording frame rate from 50 kHz to 2 MHz was used. The experiments were performed in a stainless-steel chamber, under argon protection of 1 atm.

2.2. Materials and Sample Preparation

Four types of materials, including Ti-6Al-4V (from Titanium Industries), Al6061 (from Central Steel & Wire), pure aluminum with purity of 99.99% (from Laurand), and AlSi10Mg (as-casted and printed), were used as the substrates. Three types of powders including AlSi10Mg (15–45 µm, from LPW Technology), Ti-6Al-4V (average particle size of 53-106 µm, from PRAXAIR) and Ti-6Al-4V (average particle size of 15-45 µm, from TEKMAT) were used. The substrate materials were cut using wire electrical discharge machining (EDM) with dimensions 40 mm long × 3 mm wide × 0.4-1 mm thickness and then polished

down to 0.3-1 mm thick using silicon carbide sand papers. In the experiments with the powder bed, the powder layer was spread manually with the thickness of ~100 µm.

2.3. Image Processing using ImageJ

The main image processing in this work was performed using ImageJ [48]. To identify the melt pool and vapor depression boundary from pores, the raw X-ray images were processed to reduce noise and enhance contrast. To reveal the melt pool boundary or the solid-liquid interface, we primarily tested three methods so that the motionless part in the image was converted to blank background. In the first method, the image intensity at each pixel of frame (i+1) was divided by the intensity of the corresponding pixel in frame (i). In the second method, the image intensity at each pixel of frame (i+2) was divided by the intensity of the corresponding pixel in frame (i). In the third method, the image intensity at each pixel of frame (i+3) was divided by the intensity of the corresponding pixel in frame (i). The results of the three image processing methods are shown in Figure 2, revealing an increase in the contrast and thickness of the solid-liquid interface from method one to method three. However, an increased in the thickness is not beneficial as it can cause errors in identifying the location of the interface when tracing it manually. The trajectory of the solid-liquid interface in each frame was tracked using two methods simultaneously. Method 1 was utilized to trace the interface at points further from the depression zone, while Method 2 was employed to identify the interface near the depression zone.

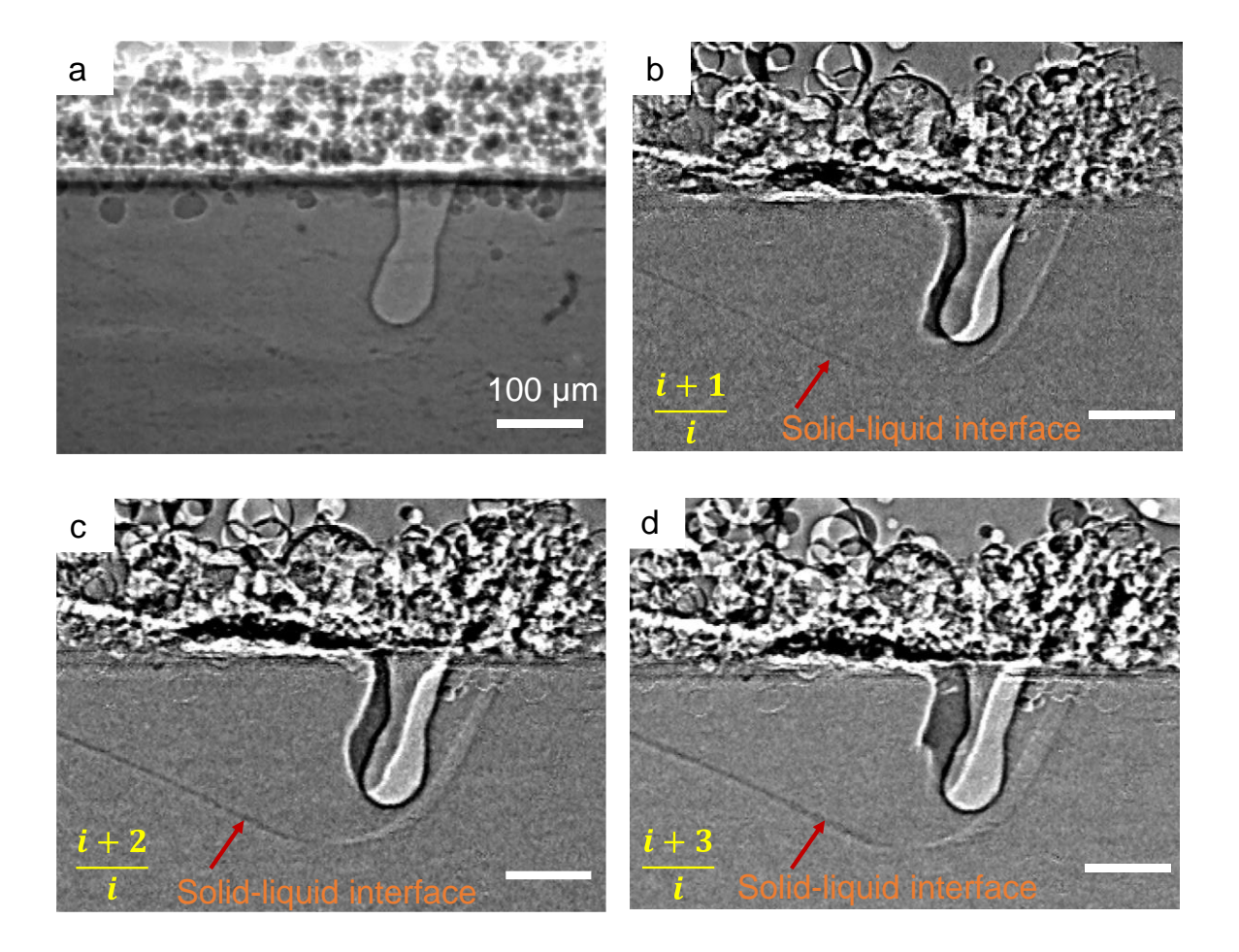


Figure 2. Image processing to reveal the melt pool boundary. (a) The original X-ray image. The result of image processing using (a) first (b) second and (c) third method. The X-ray image is captured during the LPBF process of Al6061 using laser power of 416 W, and scan speed of 0.4 m/s.

The trajectory of pores was traced manually frame by frame by recording the X and Y components of the pore location in each frame.

Chapter 3: Pore Formation during the LPBF process

This chapter presents the results and discussions published in in the following work: S.M.H. Hojjatzadeh et al. Direct observation of pore formation mechanisms during LPBF additive manufacturing process and high energy density laser welding. International Journal of Machine Tools and Manufacture 153 (2020) 103555. [48]

The publication rights for this section are given in Appendix A. Appropriate recognition is given to the relevant citation for the material in which it was originally published. The presented material represents my contributions and material collected with or by a collaborator has been highlighted as such.

Six pore formation mechanisms were observed in over 1,000 experiments on different materials and under various processing parameters during the LPBF process. In the experiments, different substrate materials were utilized to observe pore formation phenomena, as they are more visible in some materials than others. For example, while pore formation from the powder was observed in all tested materials, the transfer of pores from the powder into the melt pool during the LPBF process of Ti-6Al-4V was reported as evidence of pore formation from the feedstock powder. This was facilitated by the sharp contrast between the pores and the titanium substrate, which made it easier to observe.

3.1. Pore Formation from Feedstock Powder

An example of pore formation in LPBF process of Ti-6Al-4V using feedstock powders is depicted in Figure 3. The Ti-6Al-4V powder (from PRAXAIR) used in the experiment was a gas atomized metal powder that contained many gas pores. Two traced pores in the powders were indicated by the yellow arrows before the laser comes into the X-ray

image's field of view to melt the powder layer, as shown in Figure 3a. At $t_0 + 760 \,\mu s$ [Figure 3b], the depression zone is located below the position of the traced pores in the powder bed, just before their subsequent entrainment inside the melt pool by the liquid melt flow. At $t_0 + 820 \,\mu s$ [Figure 3c], the pores have been drawn in by the strong melt flow along the indicated pathway into the liquid melt pool to a position behind the depression zone rear wall. After solidification, the pores are trapped in the solidified track [Figure 3d, $t_0 + 2220 \,\mu s$].

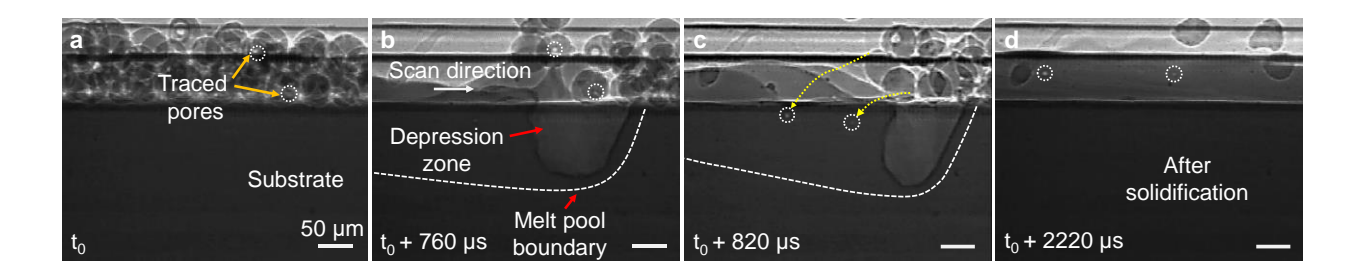


Figure 3. Pore formation from feedstock powders. (a-d) X-ray image sequence showing the transfer of pores from the powder bed into the melt pool and then, residing in the solidified track during the LPBF process at 310 W laser power and 0.6 m/s scan speed. Traced pores in the powder layer are indicated by orange arrows in the first frame (t_0). The transfer path of pores from the powder bed to the melt pool is indicated by a yellow dotted arrow in (c). The substrate material is Ti-6Al-4V.

3.2. Keyhole Induced Pore

The second pore formation mechanism that was observed is the pore formation from the keyhole. Three types of pore formation mechanisms from the keyhole during the LPBF process were observed. The dynamics of the pore formation from the keyhole are shown in Figure 4(a-d) reveal the first type of keyhole pore formation mechanism that was captured during the LPBF process of AlSi10Mg. This pore formation mechanism was observed when the laser was running under the laser power of 415 W and the scan

velocity of 0.45 m/s. A sudden decrease in the width of the depression zone, accompanied by its collapse at the first frame [Figure 4a, t_0] leads to the separation of two pores from the bottom of the keyhole [Figure 4b, t_0 + 20 μ s]. The larger pore subsequently undergoes contraction and spheroidization within 40 μ s during its movement along the melt pool boundary [Figure 4(c and d)].

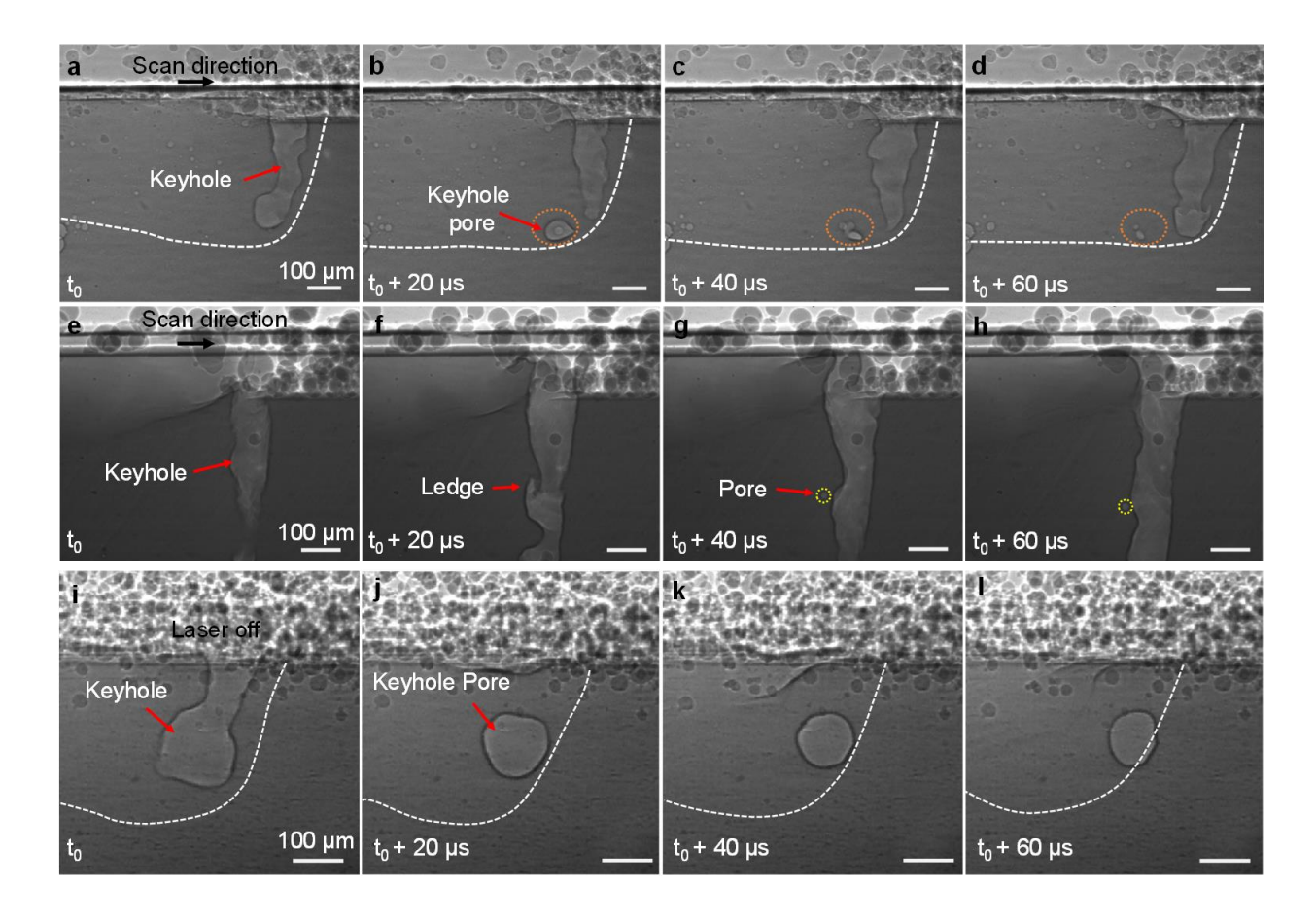


Figure 4. Keyhole-induced pore. (a-d) Pore formation due to keyhole collapse, during the LPBF process of AlSi10Mg at 520 W laser power and 0.45 m/s scan speed. (e-h) Creation of a ledge and resulting pore at the vapor depression rear wall during the LPBF process of Ti-6Al-4V at 520 W laser power and 0.3 m/s scan speed. (i-l) Pore formation when the laser was switched off at the end of the track during the LPBF process of Al6061 at 470 W laser power and 0.4 m/s scan speed.

The second type of keyhole pore formation mechanism was captured during the LPBF process of Ti-6Al-4V, at the laser power of 520 W and scan speed of 0.3 m/s, as shown in Figure 4(e-h). The base of the keyhole is not observed in the X-ray images because the keyhole longer than the height of the field view. A ledge is resolved on the rear wall of the depression zone at $t_0 + 20~\mu s$. In the subsequent frame ($t_0 + 40~\mu s$), the ledge detaches from the keyhole to form a pore near the keyhole rear wall. This pore formation mechanism was observed in all tested materials, under high energy density, when the keyhole was very deep. Such a pore was also observed to be eliminated almost immediately after its formation by moving back towards the depression zone wall. As a result, the contribution of this pore formation mechanism to entrain pores inside the melt pool is insignificant.

The formation of keyhole pore when the laser was switched off at the end of the track is shown in Figure 4(i-l). The initial frame (t₀) is the last frame when the laser was on. Within 20 µs, after the laser is switched off, the keyhole collapses due to a rapid decrease in the vapor pressure, and its bottom part remains as a large gas filled pore in the melt pool. One side of the pore, which is closer to the melt pool boundary, is pinned by the solid-liquid interface after 20 µs, while the other side remains in the melt pool. The pore undergoes contraction and spheroidization for about 120 µs into a nearly spherical shape before it is completely captured by the solid-liquid interface. In all the material substrates studied in this research, pore formation was frequently observed at the end of the laser track after the laser was removed. The experiment [Figure 4(i-l)] was repeated three times on the same substrate material (Al6061) under identical laser processing conditions. Pore

formation at the end of the track was only observed once. In two of the experiments, turning off the laser did not result in any pore formation.

3.3. Surface Fluctuation induced Pore

Two mechanisms of surface fluctuation induced pores were observed during the laser melting of a bare Ti-6Al-4V substrate, as shown in Figure 5. In the initial frame [Figure 5a, t₀], a protrusion emerges on the surface of the melt pool. Within 20 µs, the protrusion flattens and transforms into a dome shape, entraining a pore inside the melt pool [Figure 5(c-d)]. We hypothesize that the pore induced from ripples that formed on the surface during flattening of the surface protrusion.

As the laser moved forward, the second mechanism of pore formation from surface fluctuation was observed, as shown in Figure 5(e-h). At t_0 + 180 μ s [Figure 5e], a neck appears on the melt pool surface, located on the keyhole rim. This neck subsequently breaks up into a droplet (or spatter) with a 50 μ m diameter [Figure 5f, t_0 + 200 μ s], which is consistent with the behavior observed in previous studies [49,50]. The droplet falls back to the melt surface with the velocity of ~3 m/s [Figure 5g, t_0 + 220 μ s], and trapping two pores in the melt pool [Figure 5h, t_0 + 240 μ s]. The surface fluctuation induced pore formation was also observed in AlSi10Mg and Al6061. The mechanism of pore formation through surface fluctuation was frequently observed when there was significant fluctuation near the depression zone rim. We will discuss the possible mechanisms for these pore formation phenomena in the upcoming section.

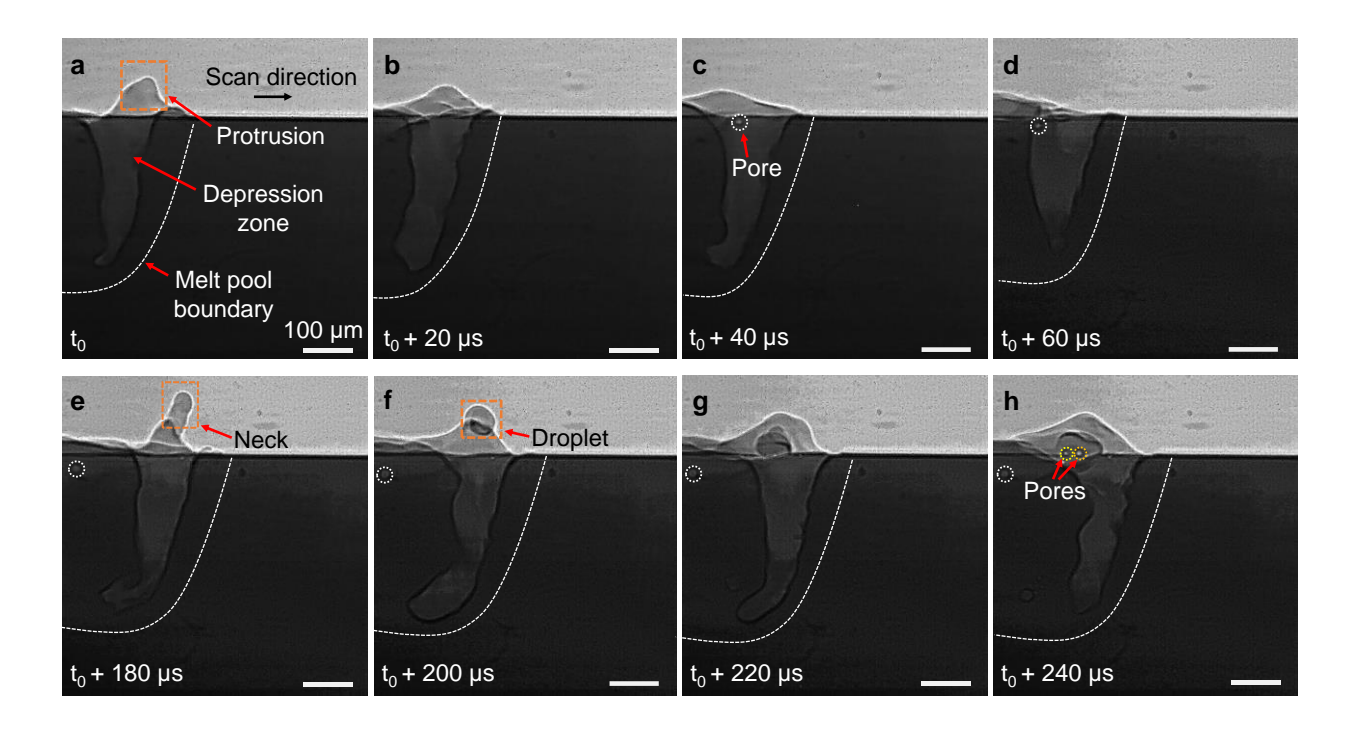


Figure 5. Pore trapped by surface fluctuation of molten pool. (a-d) Dynamic X-ray images showing the pore trapping mechanism by protrusion on the surface of the melt pool during the laser melting of Ti-6Al-4V. (e-h) Dynamic X-ray images showing the pore trapping mechanism by droplet during the laser melting of Ti-6Al-4V. Trapped pores are indicated by dotted circles. The laser power was 365 W and the laser scan speed 0.4 m/s.

3.3.1 Mechanisms of Pore Induced by Surface Fluctuation

A magnified view of the area near the depression zone rim, where surface protrusion traps pores inside the liquid melt pool, is shown in Figure 6(a-c) as a closer examination of Figure 5 (a-c). Figure 6b shows the formation of surface ripples after the protrusion starts to flatten. Drawing inspiration from surface wave-breaking phenomena [51], we speculate that the surface ripples (waves) that form on the melt pool surface trap pores using the mechanism illustrated in Figure 6d.

The schematic of the possible mechanism of gas entrapment under the impact of a droplet onto a pool surface has been shown in Figure 6(e-h). As the droplet approaches the liquid

surface, the pressure in the gap separating the droplet and the liquid surface increases (Figure 6e). The high-pressure gas pressing against the liquid creates a depression or dimple on the liquid surface (Figure 6f), which captures gas when the droplet touches the liquid surface (Figure 6g). Consequently, the trapped gas ruptures, leading to the formation of pores along the periphery of the droplet (Figure 6h). The details about these mechanisms, can be found in the previous studies [52].

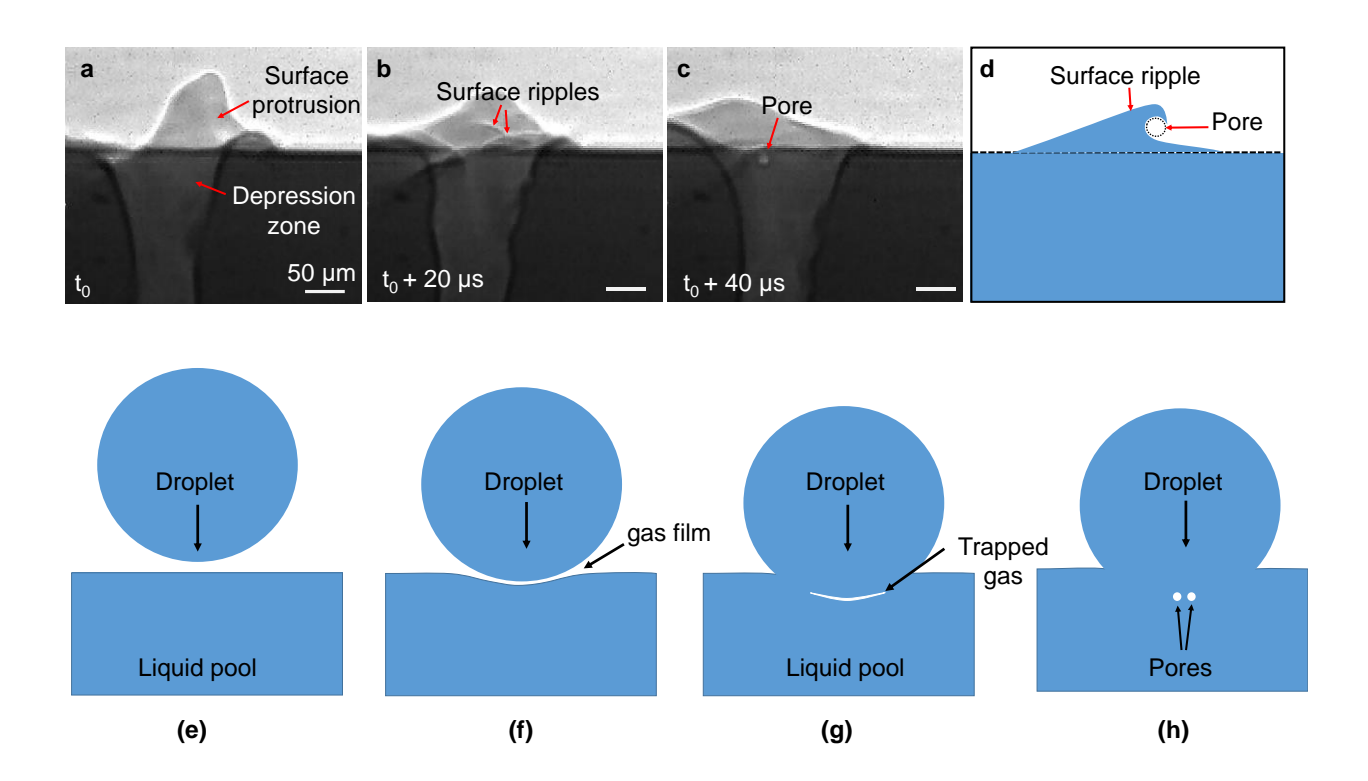


Figure 6. The mechanism of pore induced by surface fluctuation. (a-c) Dynamic X-ray images showing the pore trapped by surface protrusion during laser melting of Ti-6Al-4V, at a laser power of 365 W and the scan velocity of 0.4 m/s. (d) Mechanism of pore induced from surface ripple. (e-h) Schematic showing the mechanism of gas entrapment under an impact of a droplet onto a liquid pool.

3.4. Pore Formation from Shallow Depression Zone

The fourth pore formation mechanism was observed is the pore formation due to the depression zone fluctuation when the depression zone is shallow. Previous research

studies suggested that a keyhole pore can be avoided by reducing the laser power density to make the depression zone shallower [16]. We found that a shallow depression zone can also induce pores at a transition regime due to depression zone fluctuations. The pore formation mechanism at the transition regime, which was captured during laser scanning of a bare Al6061 substrate has been displayed in Figure 7(a-c). The depression zone in this experiment has an aspect ratio (depth over width) of less than 0.5, which indicates that the melting is in a transition regime [47]. The shallow depression zone is unstable and collapses at ($t_0 + 20 \mu s$), causing the formation of a small pore in the liquid melt pool. This pore formation mechanism was observed quite frequently during transition mode laser melting of aluminum alloys (AlSi10Mg and Al6061) but not in Ti-6Al-4V.

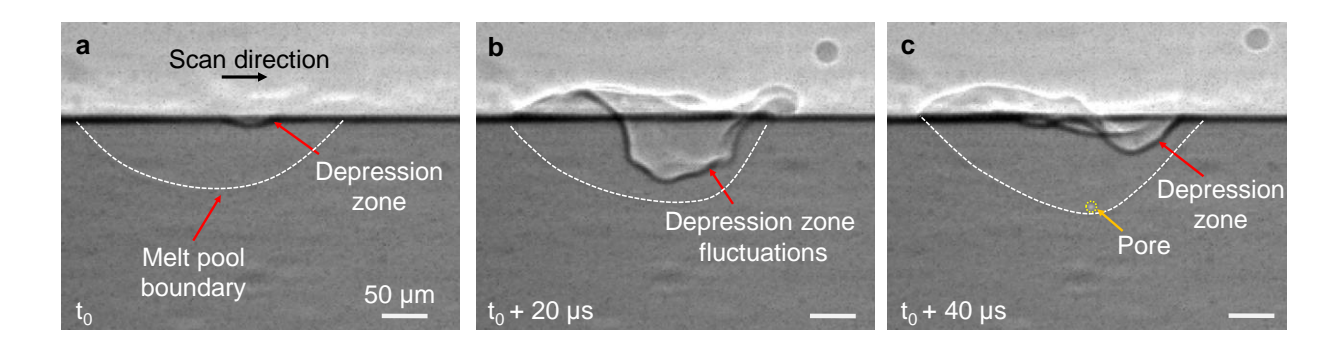


Figure 7. Pore formation due to depression zone fluctuation in transition regime. (a-c) Dynamic X-ray images showing g pore formation due to depression zone fluctuation during laser melting of Al6061 bare plate at 520 W laser power and 0.5 m/s scan speed. The pore is indicated by a dotted circle.

3.5. Crack Induced Pore

The fourth pore formation mechanism we observed is pore formation from a crack. Figure 8a shows the X-ray image of the cracks inside the Al6061 substrate. The crack was formed during the first time laser melting of the Al6061 substrate due to hot tearing [53,54]. Figure 8(b-d) display the dynamics of pore formation from the crack during

subsequent laser melting. When the melt pool encounters the crack, pores start to form from the crack [Figure 8b, t_0]. As a larger area of the crack is melted by the melt pool, the pores gradually detach as spherical pores into the melt pool [Figure 8c, t_0 + 105 μ s]. At t_0 + 203 μ s, the crack is entirely encompassed by the melt pool, resulting in the formation of multiple spherical pores in the melt pool [Figure 8d, t_0 + 203 μ s].

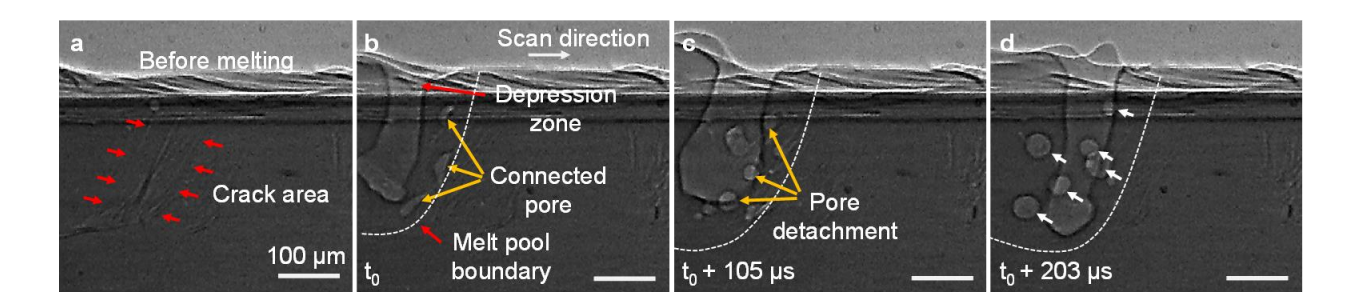


Figure 8. Pore formation from cracks. (a) X-ray image showing Al6061 substrate and a crack. (b-d) Dynamic X-ray images showing the pore formation from the crack. The cracks are delineated by red arrows in (a). In (d), spherical pores are indicated by white arrows. The laser power was 470 W, and the laser scan speed was 0.4 m/s.

The sample shown in Figure 8 was characterized after laser melting using scanning electron microscope (SEM), as shown in Figure 9. We observed that the crack was connected to the top surface but did not extend to the glassy carbon wall. During the laser melting process, it is possible that argon gas from the chamber flowed into the crack, resulting in the formation of pores inside the liquid melt pool.

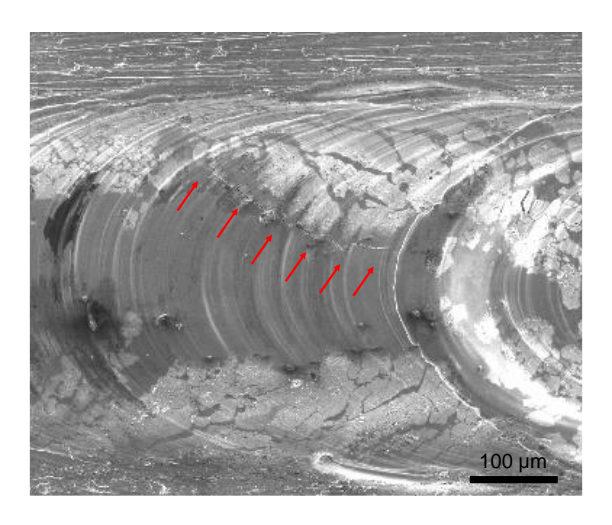


Figure 9. SEM image showing the top view of the sample with a crack after laser melting. The material is Al6061. The laser power was 310 W, and the laser scan speed was 0.4 m/s. Red arrows indicate the crack propagation on the top surface.

3.6. Pore Formation around the Melting Boundary during Laser Heating

The last pore formation mechanism was a pore formation around the melting boundary during laser heating. The dynamics of pore formation during laser melting along the melting boundary was captured by a series of ultrafast X-ray images (frame rate of 2 MHz) during the single-track laser melting of aluminum and its alloy. Here, pure aluminum (99.99%) was used to show the pore formation dynamics during laser melting. Figure 10(a-c) display X-ray image sequences from laser melting of pure aluminum substrate at 470 W laser power and 1 m/s scan speed. Pores form primarily along the melting boundary of the melt pool [Figure 10a, to], float in the liquid melt pool and move towards the depression front wall [Figure 10(b,c)]. Similar pore formation mechanism was observed at higher energy density when the depression zone was deeper, as shown in Figure 10(d-f). The pore formation mechanism in aluminum was also observed during stationary laser melting of aluminum substrate [Figure 10d]. The stationary laser experiment was also revealed that such pores could be trapped in the melt pool after the

laser was switched off, as shown in Figure 10(h,i). This pore formation mechanism is speculated that caused by vaporization of a volatile impurity substances or expansion of a tiny trapped gas in the material [55,56]. This pore formation mechanism was also observed in AlSi10Mg. As a result, it seems that this pore formation mechanism is material dependent.

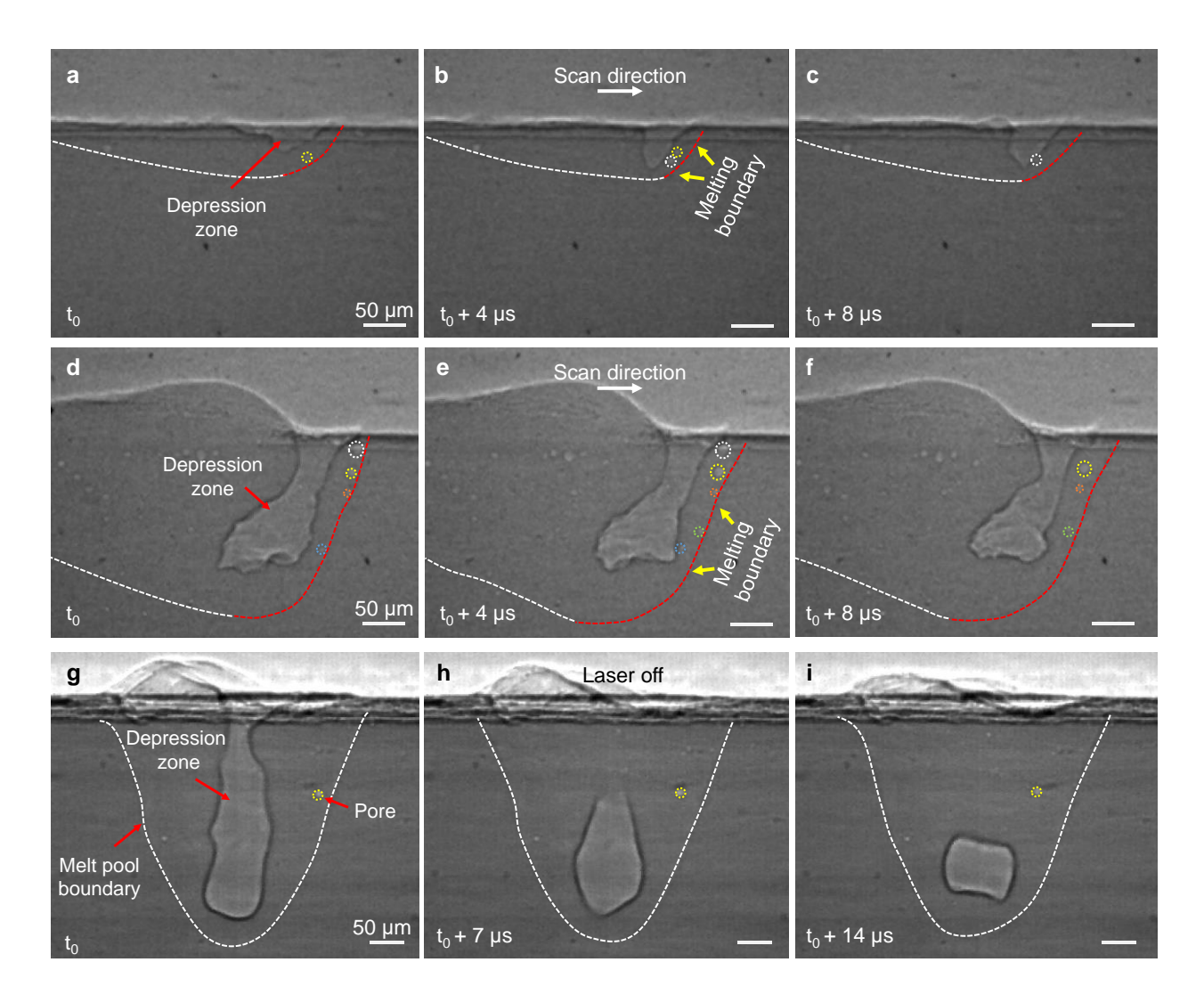


Figure 10. Pore formation at the melting boundary. (a-c) Ultra-fast (frame rate of 2 MHz) X-ray image sequence of laser melting of aluminum bare substrate showing the pore formation and growth along the melting boundary (indicated by red dotted line) at 470 W laser power and 1 m/s scan speed. (d-f) Ultra-fast (frame rate of 2 MHz) X-ray image

sequence of laser melting of aluminum bare substrate showing the pore formation and growth along the melting boundary (indicated by red dotted line) at 470 W laser power and 0.5 m/s scan speed. (g) Pore formation along the melting boundary and (h, i) pore trapping after the laser was switched off for stationary laser melting at 520 W laser power. Nucleated pores are indicated by dotted circles. The material was aluminum (99.99%).

3.7. Summary of Pore Formation Mechanisms

In this study, we utilized the in-situ high-speed high-energy X-ray imaging experiments to observe various types of pore formation mechanisms during the LPBF process. These mechanisms can be categorized into two broad categories: pores induced by the material and pores induced by the processing conditions. The first row of Figure 11 depicts pore formation induced by the material, while the second row illustrates pore formation induced by the processing conditions.

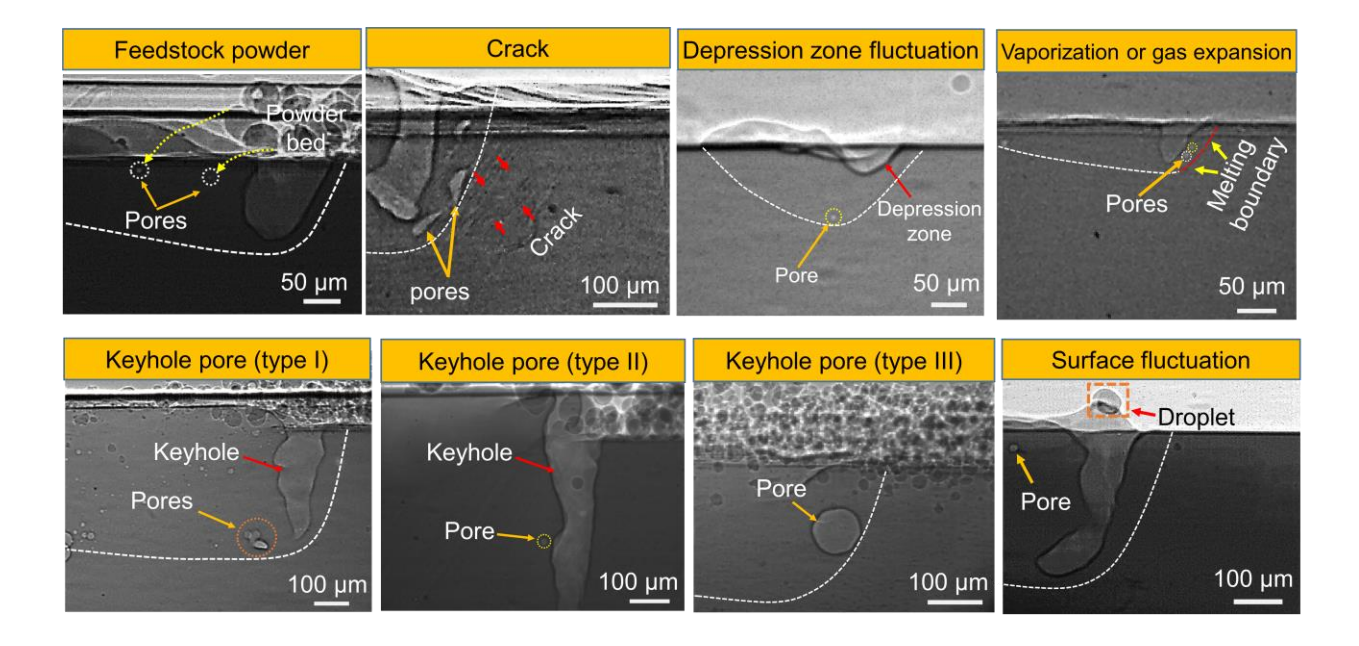


Figure 11. The summary of pore formation mechanisms observed in this work. The first row depicts the pore formation induced by the material and second row shows those induced by processing conditions.

In the first category, we observed four pore formation mechanisms, including (1) pore transferred from feedstock powder into the melt pool, (2) pore induced from solidification cracks, (3) pore induced from shallow depression zone fluctuations, and (4) pore from the vaporization of a volatile impurity substance or the expansion of a tiny, trapped gas. In the process-induced pore formation category, we observed two main categories, including (1) keyhole pore and (2) pore trapped by surface fluctuations. In the keyhole pore category, we observed three types of keyhole pore formation mechanisms: pore induced from the keyhole bottom due to sudden keyhole fluctuation (keyhole pore type I), pore induced from instability or bulge on the keyhole wall (keyhole pore type III), and pore at the end of the track when the laser was switched off (keyhole pore type III). Our results also showed two mechanisms of pore trapping by surface fluctuations: (1) pore trapped by surface protrusion and (2) pore trapped by a droplet.

Chapter 4: Pore Dynamics and Elimination

This chapter presents the results and discussions published in in the following work:

Hojjatzadeh, S.M.H. et al. Pore elimination mechanisms during 3D printing of metals.

Nature Communications 10, 3088 (2019) [21].

In the previous chapter, we identified various mechanisms that can cause pore formation due to the complex physical phenomena inside the melt pool. This suggests that pore formation is an inevitable part of the metal printing process. In this chapter, we present a detailed analysis of the dynamics of pores in the melt pool during the LPBF process and uncover the main driving force for pore motion and elimination. With this understanding, we devise an effective strategy to mitigate pore formation during the LPBF process. Finally, we demonstrate the successful implementation of this strategy in printing a pore-free part.

4.1. Experimental Design and Methods for Studying the Dynamics and Elimination of Pores in LPBF Process

4.1.1 Monitoring the Dynamics of Pore Evolution and Elimination

The experimental setup used to capture the dynamics of pore motion and elimination during LPBF is shown in Figure 12a. The details about the experiment setup can be found in section 2.1. To investigate pore motion throughout the entire melt pool, AlSi10Mg plate samples were manufactured using a commercial LPBF machine (Renishaw AM250) as substrates, with uniformly distributed pores ranging in diameter from 10 to 60 µm, as depicted in Figure 12b. A representative single-pulse X-ray image is depicted in Figure 12c. In-situ experiments were conducted under various processing conditions (i.e., various laser powers, scan speeds and layer thicknesses), and observed similar pore

motion behaviors. Here, the results were obtained under a laser power of 360 W, a laser scan speed of 1 m/s, and a layer thickness of 100 µm to demonstrate the dynamics and mechanisms of pore motion and elimination during the LPBF process.

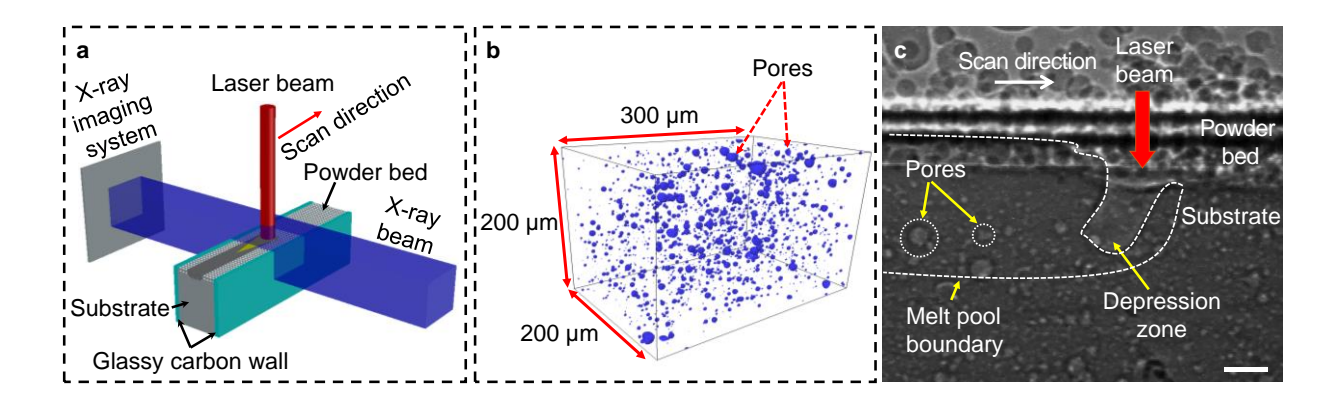


Figure 12. In-situ characterization of pore dynamics during LPBF process. (a) Schematic illustration of the in-situ high-speed X-ray imaging experiment. (b) Representative cuboid (300 μ m × 200 μ m) reconstructed from X-ray computed tomography data showing the size and distribution of pores inside an additively manufactured AlSi10Mg plate. (c) Representative single-pulse X-ray image revealing micro-pores as well as the melt pool and depression zone beneath the surface of the powder bed (laser power of 360 W, scan speed of 1 m s-1 and laser beam diameter (D4 σ) of 100 μ m). The boundaries of the melt pool and the depression zone are indicated by a white dashed line, and the position of the laser is indicated by a red arrow. The scale bar in (c) is 50 μ m.

4.1.2 Melt Flow Characterization to Estimate the Drag Force

The melt flow within the melt pool during the LPBF process was characterized using tracing particles. Tungsten microparticles (diameters of ≤10 µm) were embedded in AlSi10Mg powders by ball milling (planetary ball mill, PQ-N04, Across International). The velocities of the tungsten microparticles at different locations in the melt pool during the LPBF process were measured using high-speed X-ray imaging. Due to the large variation of melt flow velocities within the circulation domain, two sub-regions in the circulation

domain were identified and calculated separately: the melt pool close to the circulation-transition domain boundary and the melt pool tail. Twenty particles' velocities were measured to calculate the average velocity in each melt flow region.

4.1.3 Force Calculation

The main forces acting on pore in the liquid melt pool are buoyant force (F_b), melt flow induced drag force (F_d), and temperature gradient induced thermocapillary force (F_t). The equation for calculating each force is discussed below:

The buoyant force (Fb) is calculated by equation [57]:

$$F_b = \frac{4}{3}\pi r_p^3 \rho_f g \tag{1}$$

where rp is the pore radius, ρ_f is the melt density and g is the gravitational acceleration (g = 9.8 m/s).

The drag force (F_d) is induced by melt flow, which consists of a form drag and friction drag. When Reynold number is higher than unity, the drag force is calculated by the following equation [58]:

$$F_d = -\frac{1}{2}C_D \rho_f r_p^2 (U_p - U_f) |U_p - U_f|$$
 (2)

where r_p is the pore radius, ρ_f is melt density, U_p is the pore velocity vector, U_f is the melt flow velocity vector, and C_D is the drag coefficient (dimensionless) which depends on the melt flow regime and molten metal properties and is approximated by Schiller and Naumann equation:

$$C_D = \frac{24}{Re} (1 + 0.15Re^{0.687}) \tag{3}$$

where Re is Reynold number and is given by:

$$Re = \frac{2 r_p \rho_f |U_p - U_f|}{\mu} \tag{4}$$

where r_p is pore radius, U_p is the pore velocity vector, U_f is the melt flow velocity vector, ρ_f and μ are melt density and melt dynamic viscosity, respectively. We calculated the drag force exerted on the pore with zero velocity ($|U_p| = 0$) to construct the force map.

Thermocapillary force (F_0) is induced by the temperature gradient around the pore. Thermocapillary force is calculated by the following equation [59]:

$$F_t = 4 \pi r_p^2 \frac{\partial T}{\partial r} \frac{\partial \sigma}{\partial T}$$
 (5)

where $\frac{\partial T}{\partial r}$ and $\frac{\partial \sigma}{\partial T}$ are the temperature gradient at the location of the pore and the temperature coefficient of surface tension, respectively. Due to lack of data on the temperature coefficient of surface tension of AlSi10Mg alloy, the temperature coefficient of surface tension of Al88Si12 alloy ($\frac{\partial \sigma}{\partial T} = -0.31 \times 10^{-4} \text{ N m}^{-1} \text{ K}^{-1}$) was used [60]. The average temperature gradient obtained from the simulation results were estimated to be $6.5 \times 10^7 \text{ K m}^{-1}$ at the laser interaction area and $1 \times 10^6 \text{ K m}^{-1}$ and at circulation area.

4.1.4 Multi Physics Simulation

The temperature in the melt pool was simulated by multiphysics modelling with the laser parameters used in the experiments. The model was calibrated by experimental data (length and depth of melt pool and depth of depression zone). The initial powder bed packing configuration is generated using the Discrete Element Method, where the input powder size distribution follows the experimental measurements, and the simulated packing density agrees with experimental measurement. The powder bed geometry is then implemented into a thermal-fluid flow model to simulate the multiphysics

process of heat transfer, phase transformation, and molten fluid flow. The fully coupled governing equations, including continuity, momentum and energy conservation equations, are computed using the Finite Volume Method, while the free surfaces are tracked using the Volume of Fluid method. Flow is assumed to be incompressible, laminar, and Newtonian; laser energy absorption, thermal conduction, surface radiation and convection, and latent heats of melting and vaporization are incorporated for energy conservation. Major driving forces of the molten pool flow are implemented, including recoil pressure, surface tension, Marangoni effect, viscosity, buoyancy and gravity. The thermophysical properties of AlSi10Mg used for simulation are given in Appendix Table 1 and Appendix Table 2. Further details about these models can be found in the reference [61–63]¹.

4.1.5 X-Ray Micro Computed Tomography (μ-CT)

X-ray μ-CT was used to characterize the pore size and distribution in the AlSi10Mg substrate three dimensionally. The experiments were conducted at beamline 2-BM-A of the Advanced Photon Source at Argonne National Laboratory. A pink x-ray beam, with the energy centered at 25 keV penetrated through the sample and was converted to a visible light signal using a single crystalline scintillator (Lu3Al5O12:Ce, 20 μm thickness). Then, the visible light signal was captured using a CMOS camera (pco.edge camera, PCO AG, Kelheim, Germany) with a 10× objective lens. The effective pixel resolution is 650 nm. 1500 projection images were recorded over the 180° rotation of the sample, with an exposure time of 0.1 s for each image. The rotation speed of the stage was maintained

¹ The multiphysics simulation presented in Figure 13 was performed by Wantao Yan, from the Department of Mechanical Engineering at the National University of Singapore, 117575, Singapore.

at 1° per second. The through-the-thickness slices were reconstructed from the projections using an in-house software (Tomopy [64]). These slices were then stitched together using image processing software (Avizolite 9.4, FEI visualization Sciences Group) for the isosurface rendering.

4.2. Dynamics of Pore Motions within Melt Pool

The movements of individual pores in the melt pool were carefully traced, and it was found that the pores in different regions of the melt pool exhibited different moving patterns [Figure 13(a-d)]. In the region near the laser beam, the pores moved toward depression zone and escaped from the melt pool, hereafter referred to as the laser interaction domain [Figure 13d]. In the region at a certain distance away from the laser interaction domain, the pores circulate within the melt pool, hereafter referred to as the circulation domain [Figure 13a]. Between these two regions, the pores move in irregular patterns, i.e., sometimes moving toward the surface of the melt pool and escaping [Figure 13c], while sometimes circulating in the melt pool [Figure 13b], hereafter referred to as the transition domain. Similar pore moving behaviors were observed during the laser melting of AlSi10Mg bare substrates, as well as under other processing conditions.

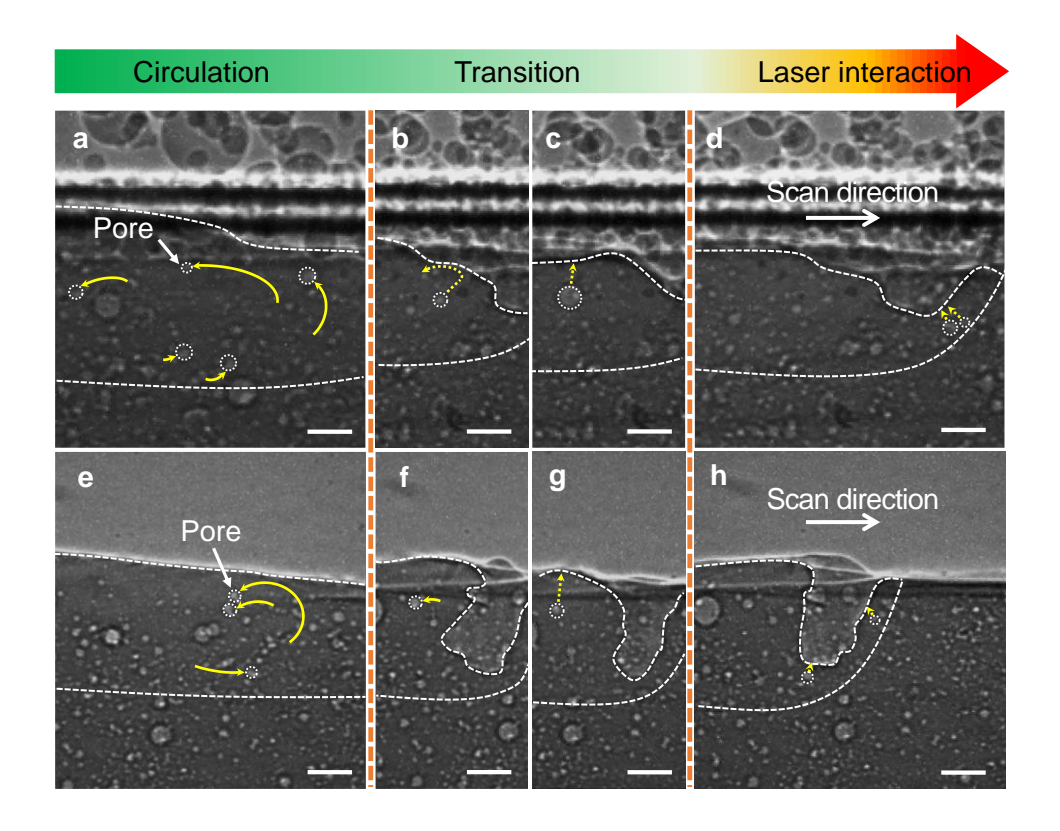


Figure 13. Dynamic pore motions within melt pool. (a-d) X-ray images showing pore dynamics during the LPBF process. The thickness of powder layer is $100 \, \mu m$. (e-h) X-ray images showing pore dynamics during laser melting of a bare substrate. Dotted arrows indicate the future trajectories of the pores (time $\leq 30 \, \mu s$), while solid arrows mark the history of pore trajectories (after time = $150 \, \mu s$). Pores follow circular patterns at the circulation domain (a, e), while pores in the laser interaction domain move toward depression zone and escape from the melt pool (d, h). In the transition domain (b, c, f and g), pores exhibit irregular moving behavior, sometimes moving toward the melt pool surface and escaping (c, g), and sometimes circulating in the melt pool (b, f). The laser beam diameter (D4 σ) is $100 \, \mu m$, the laser power is $360 \, W$, and the scan speed is $1 \, m \, s^{-1}$. All scale bars are $50 \, \mu m$.

4.3. Driving Forces for Pore Motion and Elimination

Two major forces acting on the pore motion are buoyant force and melt flow induced drag force [57,65]. The buoyant force was calculated directly based on the actual pore size measured from the X-ray images using equation (1). In order to measure the drag

force caused by the melt flow on pores, a particle tracing experiment was conducted to analyze the melt flow velocity inside the melt pool during the LPBF process of AlSi10Mg. The trajectories of the tracing particles were quantified at different location of the melt pool, as shown in Figure 14(a-c). The melt flow pattern within the circulation domain was identified as circulating in two sub-regions [Figure 14a]. The velocity average was found to be varied from 0.75 ± 0.2 m/s [mean \pm standard deviation (s.d)] near the boundary of the circulation-transition domain to 0.4 ± 0.1 m/s at the tail of the melt pool. To simplify the analysis, the melt flow velocity within the circulation domain was approximated by an average of 0.6 ± 0.2 m/s. In the laser interaction domain, the melt flows downward, along the front wall of the vapor depression zone with an average velocity of 1.9 ± 0.6 m/s [Figure 14c]. In the transition domain, the melt flow pattern is more complex due to the interplay of circulation and backward flow and exhibits an average velocity of 1.45 ± 0.5 m/s [Figure 14b].

Using equation (2) and the average melt flow velocity, the drag force was calculated at three different domains: circulation, laser interaction, and transition. The results indicate that the drag force is orders of magnitude higher than the buoyant force for the pore size range studied here (Figure 18a). Thus, it is expected that pores in the melt pool will move with the melt flow and have very limited opportunity to float up and escape by buoyancy. This can satisfactorily explain pore moving dynamics in the circulation domain. However, in the laser interaction domain, the pores move approximately perpendicular to the melt flow direction and manage to rapidly escape out from the melt pool, with a velocity of up to over 2 m/s, even though the melt flow velocity is the highest in this domain among all

locations in the melt pool. This is in contrary to pore motion behavior predicted based on buoyant force and melt flow induced drag force.

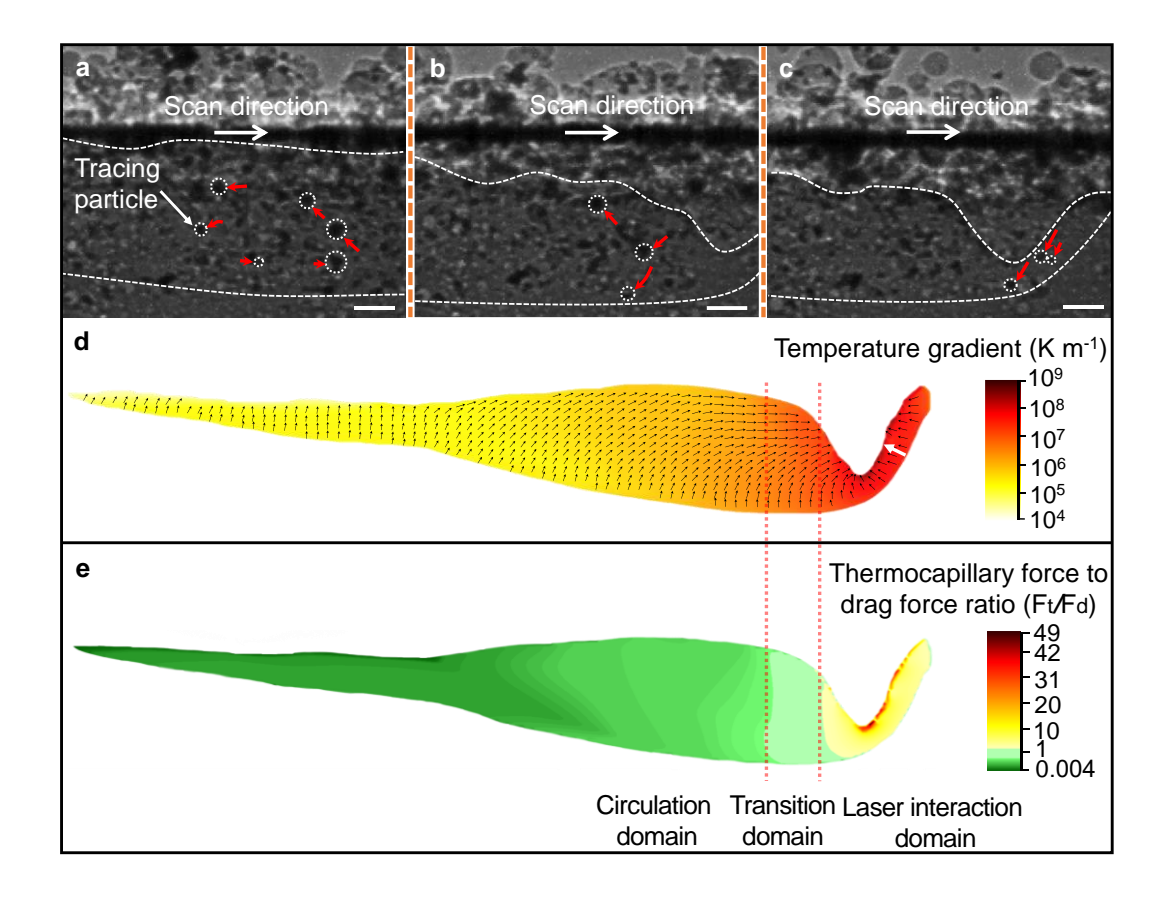


Figure 14. Driving forces for pore motion and elimination. (a-c) X-ray images showing trajectories (indicated by red arrows) of the tracing particles (tungsten microparticles, marked by white dotted circles), which indicate the melt flow at the circulation domain (a) transition domain (b) and laser interaction domain (c) inside the melt pool during the LPBF process. (d) Temperature gradient inside the melt pool during LPBF process, obtained by multiphysics modeling with laser processing parameters the same as the in-situ experiments in Figure 13. The magnitude and direction of temperature gradient are indicated by color and black arrows, respectively. The white arrow in d indicates the temperature gradient increases from the solid-liquid interface (melting front) to the depression zone front wall. (e) Ratio of thermocapillary force (F_t) to drag force (F_d) for a pore with a diameter of 10 μ m. In (a-c), the laser power is 360 W, the scan speed is 1 m/s and the thickness of powder layer is 100 μ m. Scale bars in (a-c) are 50 μ m.

After carefully analyzing the pore moving direction and the temperature gradient, it was hypothesize that the thermocapillary force [66] induced by the high temperature gradient in the laser interaction domain is the driving force for the unexpected pore elimination. For most metals and alloys, the temperature coefficient of surface tension is negative $(\partial \sigma / \partial T < 0)$. The thermocapillary force drives the liquid along the pore interface to flow from hot region to cold region. As a result, the pore experiences a thermocapillary force opposite to the flow direction and will move from cold to hot [67]. The schematic of pore movement inside the liquid due to thermocapillary effect has been shown in Figure 15.

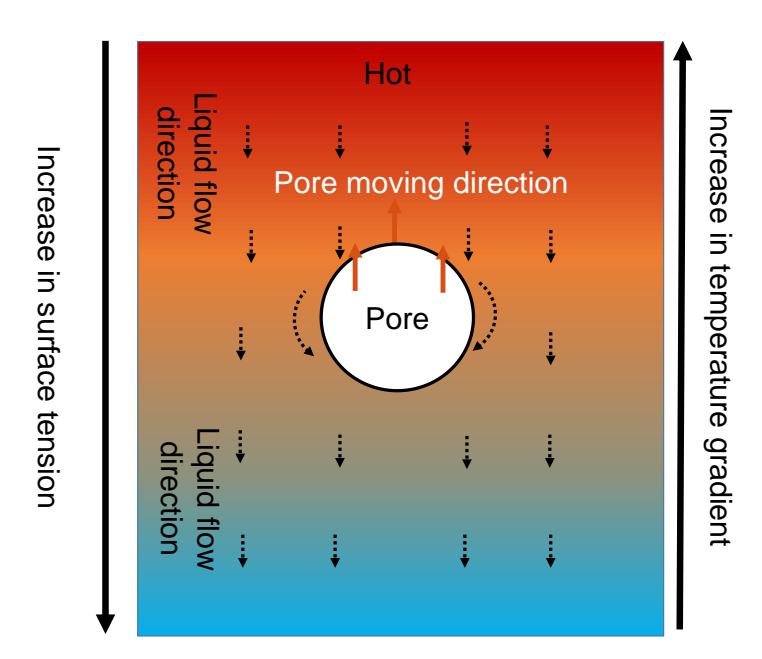


Figure 15. The mechanism of pore movement due to the temperature gradient inside the liquid. Solid red arrows indicate the direction of pore movement, while black dotted arrows indicate the direction of liquid. The color map illustrates the temperature gradient inside the liquid.

In order to calculate the thermocapillary force using equation (5), the temperature gradient in the melt pool was simulated by a multiphysics model (see section 4.1.4). In

the laser interaction domain, the temperature gradient has an average value of 6.5×10^7 K m⁻¹, as shown in Figure 14d. This gradient is directed approximately normal to the melt pool surface, as indicated by the small black arrows in Figure 14d. Such high temperature gradient results in a thermocapillary force that is at least three times higher than the melt flow induced drag force in the laser interaction domain. Therefore, the pores in the laser interaction domain move along the temperature gradient and escape from the melt pool. Detailed analysis reveals that the temperature gradient increases from the melting front to the vapor depression front wall, as shown in Figure 16a. This implies that the acceleration and velocity of a pore will increase when it moves toward the depression zone front wall. The predicted increase in velocity and acceleration increase was indeed observed, as shown in Figure 16(b-c). This observation further confirms the proposed thermocapillary force-driven pore elimination mechanism in this study.

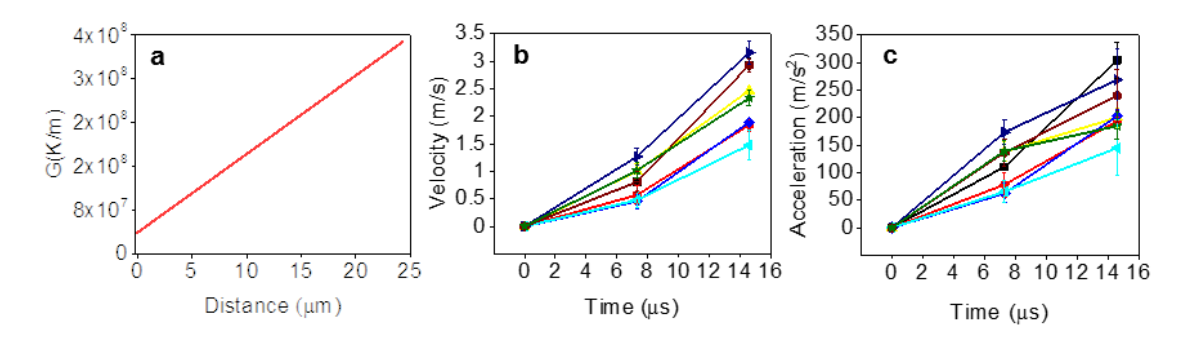


Figure 16. Increase of acceleration as pores move toward depression zone wall. a Variation of temperature gradient, G, from the melting front to the depression zone wall (indicated by the white arrow in Figure 14d). The temperature gradient increases towards the depression zone wall. (b) Velocity, as a function of time, as pores move toward depression zone wall. (c) Acceleration, as a function of time, as pores move toward depression zone wall. The data in (b and c) are collected during laser melting of an AlSi10Mg bare plate (laser power of 310 W, scan speed of 1 m/s).

To study the effect of thermocapillary force on pore dynamics in different locations of the melt pool, a force map based on the ratio of thermocapillary force to drag force (F_1/F_d)

was developed for a 10 μ m-dimeter pore, using the local temperature gradient and the average velocity of the melt flow (1.1 \pm 0.5 m/s), as shown in Figure 14(e). The buoyant force was neglected because it is orders of magnitude smaller than the thermocapillary force and the drag force for the pore size range studied here, as shown in Figure 18a-b. Figure 14(e) shows that, F_i/F_d varies significantly at different locations in the melt pool, which is due to significant variations in the temperature gradient. F_i/F_d ranges from the highest value of ~47 in the laser interaction domain to ~0.004 near the tail of the melt pool. Thus, the thermocapillary force is the dominating force in the laser interaction domain, which drives the pores to move in the direction of the temperature gradient, while the drag force controls pore motion in the circulation domain. In the transition domain, F_i and F_i are very close, which results in the irregular and ambivalent pore moving behavior.

4.4. Mechanisms of Pore Dynamics and Elimination

The dynamics and mechanisms of pore motion and elimination in the melt pool during the LPBF process is schematically summarized in Figure 17. The pore moving behavior is governed by competition of the temperature gradient induced thermocapillary force and the melt flow induced drag force. The buoyant force will play a more important role when the size of the pore becomes larger. However, our estimation shows that, for the buoyant force to become dominant, the sizes of the pores need to reach millimeters, even larger than the size of a typical melt pool in the LPBF process, as shown in Figure 18(c-d). Thus, the main driving force for pore elimination during the LPBF process is the thermocapillary force, instead of the commonly thought buoyant force.

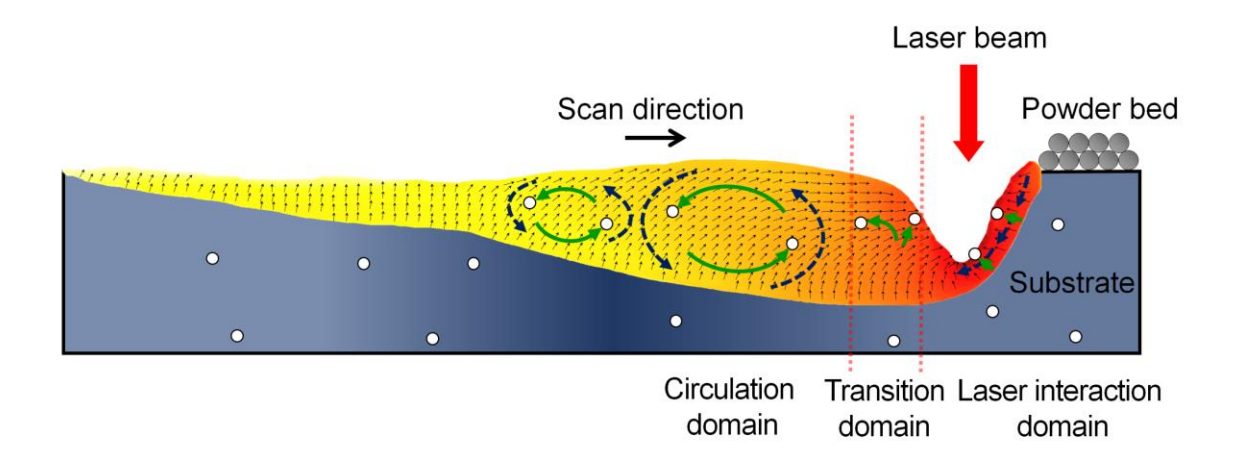


Figure 17. Mechanisms of pore dynamics and elimination. Schematic illustration showing the dynamics of pore motion and pore elimination within the melt pool during the LPBF process.

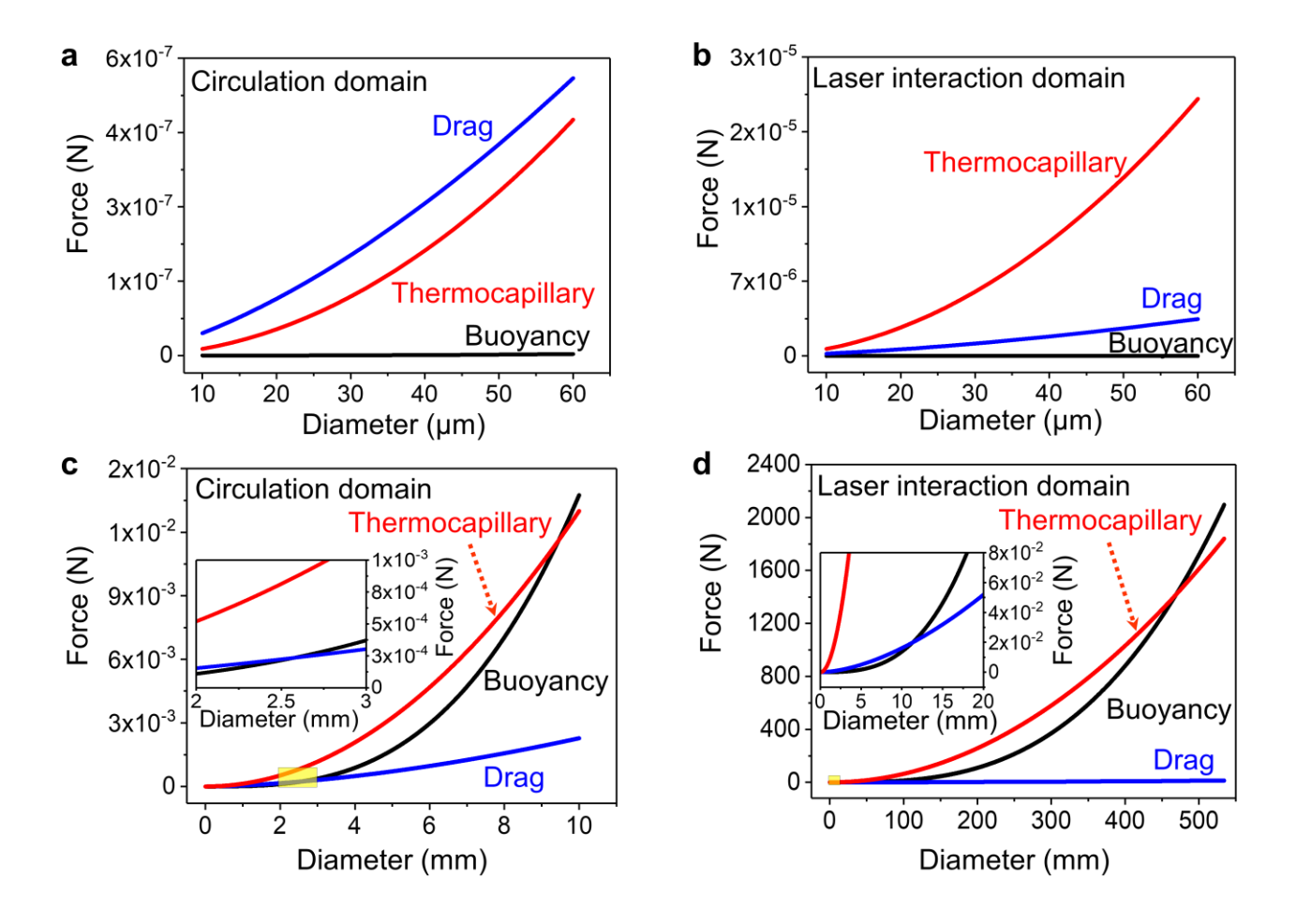


Figure 18. Force analysis. Comparison of drag force, buoyant force and thermocapillary force at the circulation domain (a) and the laser interaction domain (b) for the pore size range studied in this work. (c-d) Forces as a function of pore dimeter. The critical pore size for buoyant force to overcome drag force is 2.5 mm at the circulation domain (c) and 11 mm at the laser interaction domain (d), which are even larger than the size of a typical melt pool in the LPBF process. The critical pore size for the buoyant force to exceed the thermocapillary force is even larger, requiring a pore size of at least 10 mm in the circulation domain (c) and 500 mm at the laser interaction domain (d).

4.5. Eliminating Pores using Thermocapillary Force

The thermocapillary force driven pore elimination can serve as an effective approach to eliminating pores during the LPBF process. Here, two examples are presented as a proof of concept. First, Figure 19(a-d) show that the pores in the feedstock powders can

be eliminated by thermocapillary force under optimized laser processing conditions to achieve a pore-free track. Second, Figure 19(e-h) demonstrate that pores in the previously built layer can be eliminated by thermocapillary force during laser rescanning under appropriate laser scan parameters.

The following two general guidelines are used to determine the proper laser processing parameters. Firstly, the proper laser processing parameters are selected to ensure that the temperature gradient in the laser interaction domain is high enough to overcome the melt flow induced drag force. The temperature gradient around the laser interaction domain can be estimated by the difference between the boiling temperature (T_b) and melting temperature (T_m) of the material over the thickness [t, as indicated in Figure 19b] of the liquid layer around the depression zone, (T_b - T_m)/t. For a given material, a smaller (t) indicates a higher temperature gradient. Second, the area of the high temperature gradient region should be reasonably large to have a good opportunity to encounter pores. This means that a larger laser interaction domain is required, which can be estimated by the width (t) over depth (t) ratio of the depression zone, t0, as indicated in Figure 19b. However, the depression zone depth, (t0), cannot be too small. When (t0) is too small, the melt pool depth is too shallow, which may cause lack of fusion.

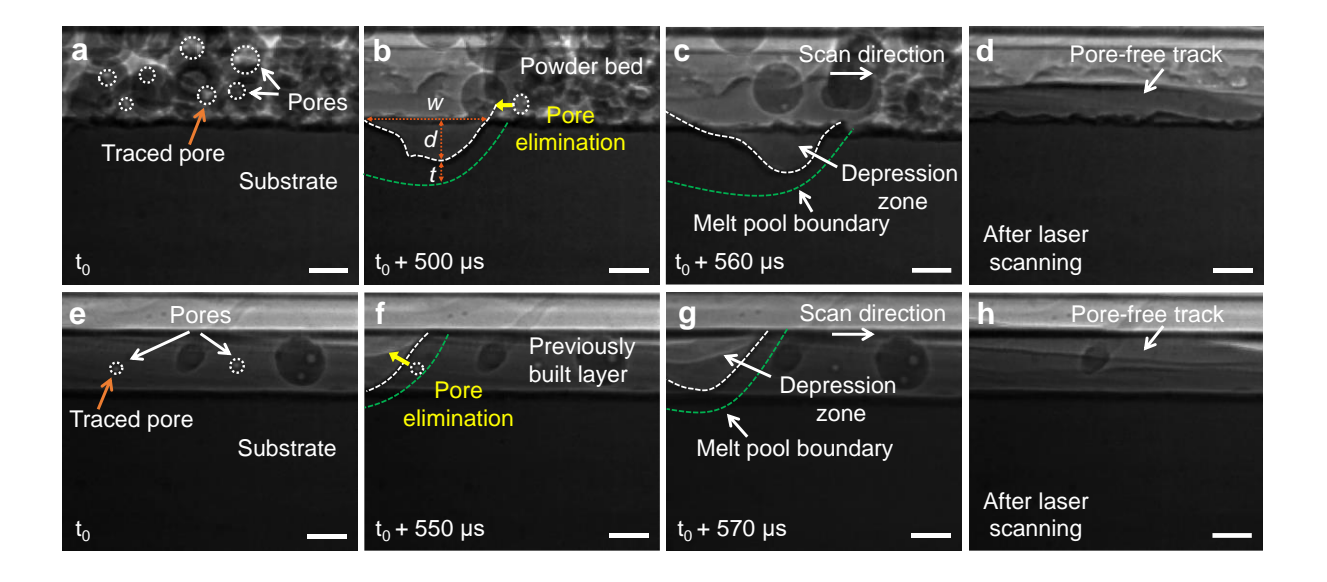


Figure 19. Eliminating pores using thermocapillary force. (a-d) Dynamic X-ray images showing elimination of pores in feedstock powders. The thickness of powder layer is 100 μm. In (b), w and d indicate the depression zone width and depth, respectively, and t represents the thickness of the liquid layer around the depression zone. (e-h) Dynamic X-ray images showing elimination of pores in the previously built layer. Traced pores are indicated by dotted circles. Pore moving trajectories are indicated by yellow arrows. The melt pool and depression zone boundaries are outlined by green and white dashed lines, respectively. Time indicated in the picture represents the time after laser turning on. The powder and substrate are Ti-6Al-4V. The laser beam diameter (D4σ), laser power, and scan speed are 75 μm, 210 W, and 0.6 m/s, respectively. All scale bars are 50 μm.

4.6. Printing a Pore-free Part

We designed the laser processing parameters to increase the effect of thermocapillary force-driven pore elimination in the build process to achieve a pore-free printed part. We tested our approach with our customized LPBF system because it allowed us to have more control over the laser parameters. We characterized the as-built samples using synchrotron x-ray computed tomography (CT) technique. The effective pixel resolution is 650 nm, much higher than that afforded by commercial x-ray CT machines, allowing micron-sized pores to be revealed. The results are shown in Figure 20. Using the same

powders (gas-atomized AlSi10Mg powders without preheating; preheating is a process to remove absorbed water on the surface of aluminum alloy powders), the samples we built, adopting the proposed pore elimination mechanism, had orders of magnitude fewer pores than the samples made by Honeywell Federal Manufacturing & Technologies LLC using a commercial LPBF system (Renishaw AM250) with the parameters developed by their engineer.

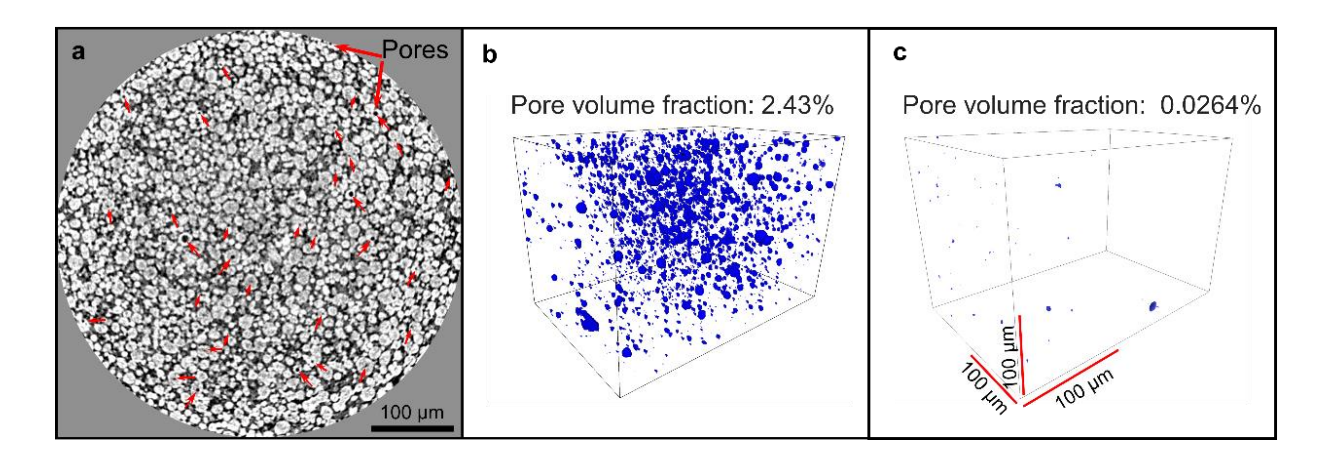


Figure 20. Pores distribution inside AlSi10Mg powders and as-printed AlSi10Mg samples. (a) One slice from x-ray tomography data showing pores inside AlSi10Mg powders. (b-c) Representative reconstructed x-ray computed tomography cuboids (300 μm × 200 μm × 200 μm) showing the size and distribution of pores inside the as-printed AlSi10Mg sample built by commercial machine (Renishaw AM250) (b) and our customized laser powder bed system using parameters designed based on thermocapillary force driven pore elimination mechanism (c). b and c share the same scale bar.

The reported levels of porosity in AlSi10Mg alloy printed with various commercial LPBF machines are shown in Table 1. The minimum porosity level achieved in AlSi10Mg alloy with different commercial LPBF machines is approximately 0.2 vol.%. However, we were able to achieve a significantly lower porosity level of 0.0264% without implementing a

preheating strategy, demonstrating the effectiveness of using thermocapillary pore elimination mechanism during printing.

Table 1. Pore volume fraction of as-printed AlSi10Mg reported in the literature.

Literature	Machine	Powder preheating	Pore volume fraction%
Read et al., Mater. Des. 65, 417–424 (2015) [68]	Concept Laser M2	-	0.29%-0.61%
Aboulkhair et al., Addit. Manuf. 1, 77–86 (2014) [9]	Realizer GmbH SLM- 50	Preheating	0.23%-4.4%
Thijs et al., Acta Mater. 61, 1809– 1819 (2013) [69]	Concept Laser M1	-	0.6%-1.8%
Weingarten et al., J. Mater. Process. Technol. 221, 112–120 (2015) [30]	Trumpf Trumaform LF250	Preheating	0.2%-7% (Only hydrogen pores were measured; lack of fusion pores were not included)
Wang et al., Opt. Laser Technol. 96, 88–96 (2017)[70]	Renishaw AM250	-	1%-3%

4.7. Summary of Pore Dynamics and Elimination Results

In summary, we demonstrated pore dynamics and pore elimination mechanisms in 3D printing of metals by combining in-situ X-ray experiments and multiphysics modeling, and achieved the following results:

(1) Pore was observed to circulate in the melt pool far from the depression zone and escape through the depression zone wall at the laser interaction area.

- (2) Thermocapillary force induced by the high temperature gradient is responsible to eliminate pores at laser interaction domain while drag force is responsible for pore circulation far from the hot regions of the melt pool.
- (3) We established the criteria for enhancing the thermocapillary effect during the LPBF process to eliminate pores from the powder layer and remove any remaining ones in the previously built layers. We then utilized optimized laser parameters to implement this approach in a customized LPBF machine, resulting in the printing of a part with a low volume fraction of porosity.

Chapter 5: Defects Prediction during Metal Additive Manufacturing

This chapter reports on the approach and methodology for predicting the keyhole pore and solidification crack. It is demonstrated that the keyhole pore can be predicted before it forms inside the melt pool by identifying keyhole fluctuations. Furthermore, the relationship between keyhole dynamics and solidification dynamics is identified, which will be used to determine the criteria for predicting solidification cracking.

5.1. Experiment Design

5.1.1 In-Situ X-Ray Experiment

In-situ synchrotron x-ray imaging under varying recording frame per second (*fps*=50, 100 and 140 kHz) was utilized to probe the dynamics of defects, pores and cracks, in real time during the LPBF process of Al6061 and Ti-6Al-4V. We utilized a combination of different laser powers (*P*), scan speeds (*v*) and laser beam sizes (*r*), to achieve a keyhole mode conditions within the keyhole depth (*d*) range of ~200-330 µm in Al6061 and 255-490 µm in Ti-6Al-4V substrate materials.

5.1.2 Image Processing

Figure 21 shows the workflow for automatic detection of the keyhole and pores and measuring their geometries. To reduce noise and enhance contrast, we subtracted the offset background (i.e., the X-ray image of the substrate with powder before laser melting) and applied a 2D Gaussian filter using ImageJ. Subsequently, we removed undesired areas from the X-ray image, including the powder layer and the lower part of the image outside the melt pool, to reduce noise and errors in future image segmentation (Figure 21b). To investigate the moving keyhole and pores within the substrate material and measure their geometries, we utilized the k-means clustering method on dynamic X-ray images using MATLAB [71]. Image segmentation using k-means clustering is an

unsupervised machine learning technique that involves dividing an image into multiple segments or regions based on similarities in color, intensity, or texture. The k-means clustering algorithm is applied to the pixels of the image, treating each pixel as a data point in a multidimensional space where each dimension corresponds to a color channel or an image feature. The result of image segmentation by k-means clustering is shown in Figure 21c. The image has been segmented into two colors, the purple for the pores and yellow for background. Next, the image was converted to binary image in order to use the in-built MATLAB functions, as shown in Figure 21d. To distinguish between the keyhole and pores, we calculated the area of each object in the binary image and identified the object with the largest area as the keyhole, as shown in Figure 21e. Next, the geometry of the keyhole, including the keyhole area, depth, top width, and aspect ratio (i.e., depth/width), was calculated in every frame. The uncertainty on measurement was ±2 µm. The result of automatic measurement of the keyhole geometry during the LPBF process of Ti-6Al-4V is displayed in Figure 22.

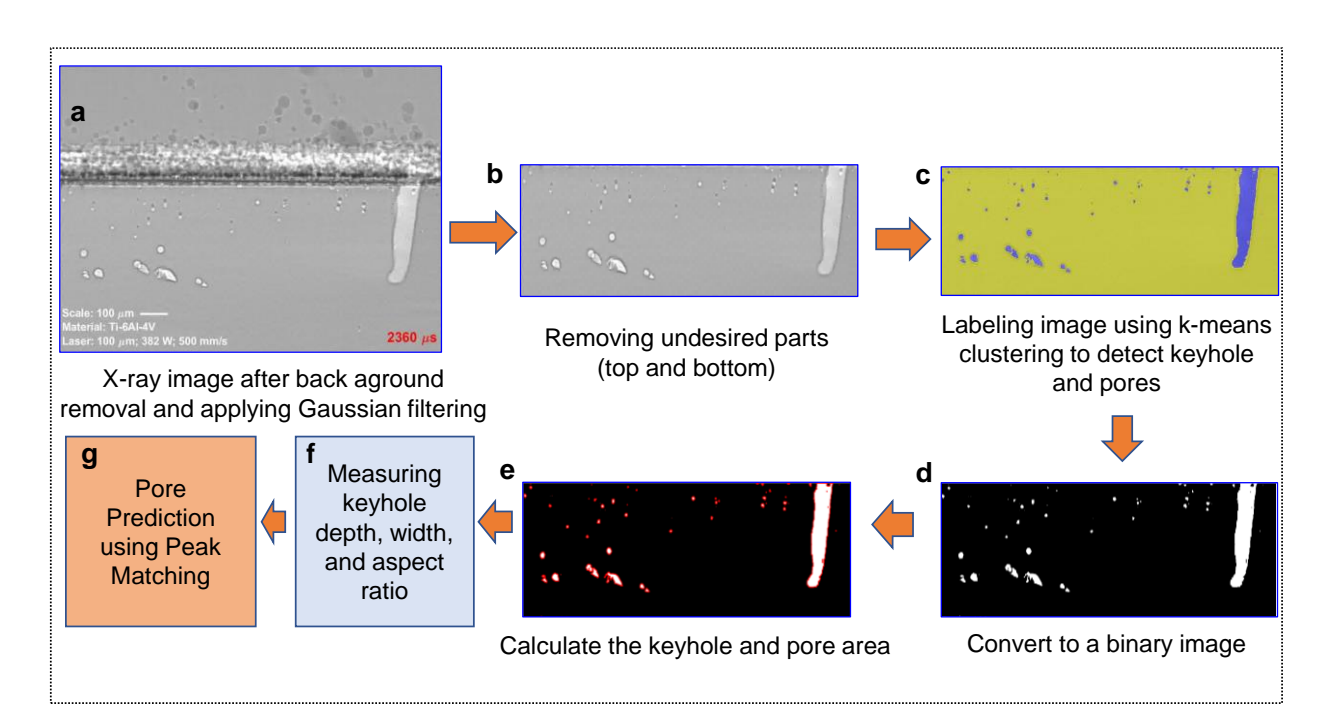


Figure 21. Workflow for automatic detection of the keyhole and pore and the prediction based on peak position matching. The Ti-6Al-4V experiment was cited from [72].

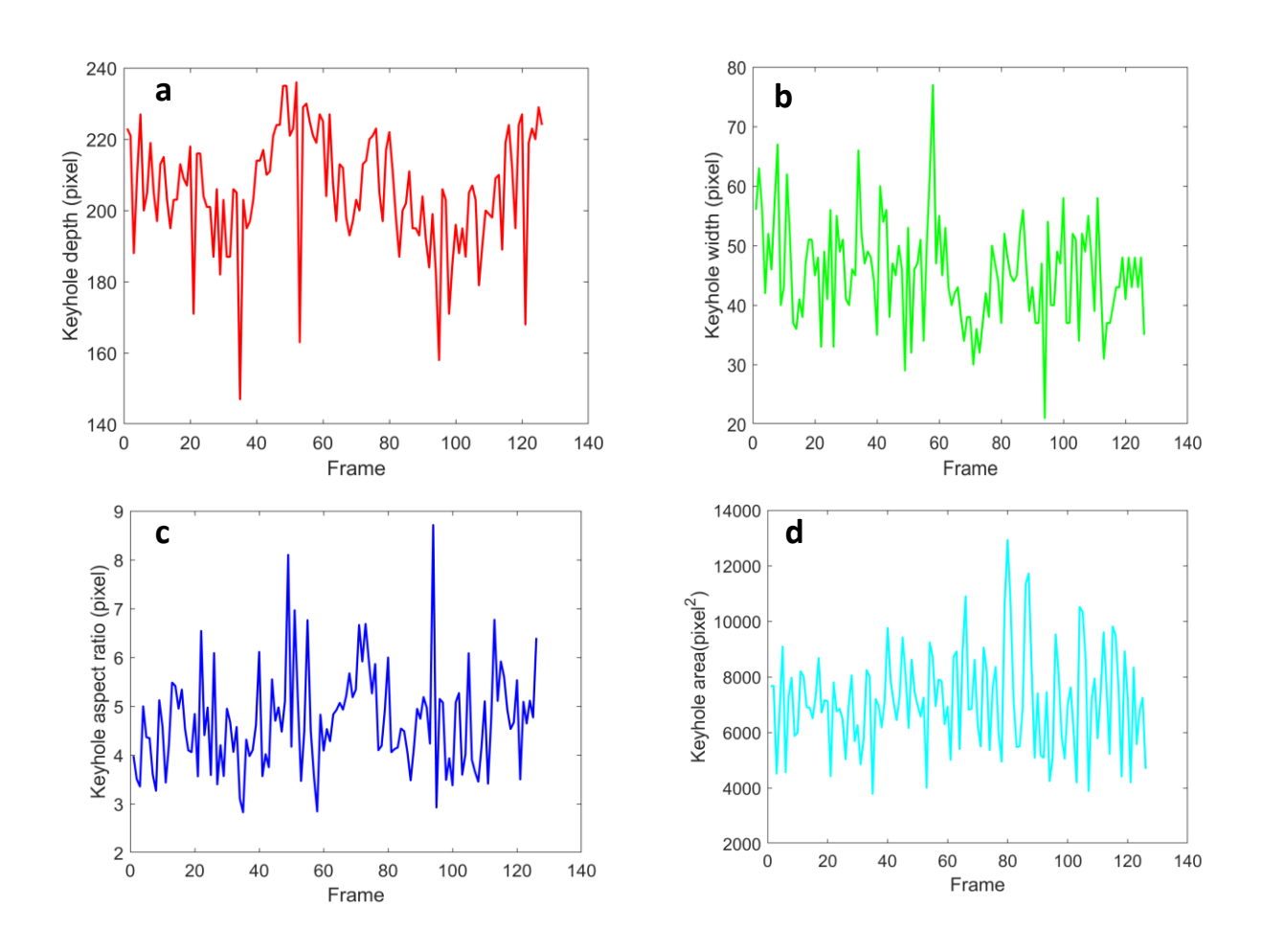


Figure 22. Measured keyhole geometries using image processing. The results of measurement for (a) keyhole depth, (b) width, (c) aspect ratio and (d) area.

5.1.3 Finding Peaks and Valleys

We used MATLAB's built-in findpeaks function to extract peaks and valleys from the keyhole width, depth, and aspect ratio signatures [73]. Specifically, we set the criteria to denote a peak in the aspect ratio signal as a difference greater than 0.09 between the data point at the peak and its neighboring points. We then developed a MATLAB algorithm

to identify similarities in the positions (timeframe) of peaks and valleys in keyhole signatures.

5.1.4 The Method to Capture Solidification Front Evolution during the LPBF Process

To quantify the solid-liquid interface, a small frame rate of 50 kHz was utilized since the trajectory of the interface was too small to be distinguished in every frame at higher frame rates. Figure 23 provides an overview of the methodology used to track the solidliquid interface and calculate the solidification rate during the LPBF process of Al6061 using high-speed X-ray imaging. Figure 23a shows the representative X-ray image captured during the LPBF process of Al6061. The solid-liquid interface is barely visible after adjusting the image threshold at time t. The original X-ray image underwent preliminary image processing using the method discussed in section 2.3. This involved using ImageJ to remove the background and reveal the solid-liquid boundary, as shown in Figure 23b. To analyze the solid-liquid interface during the melting process, the interface was manually tracked at each time frame using discontinuous scattered points. Subsequently, a ninth-order polynomial equation was used to fit the points, as shown in Figure 23c. The normal direction at any given point along the solid-liquid interface was then calculated using the first-order differentiation of the ninth-order fitted curve, as shown in Figure 23d. The solidification rate was determined by taking the distance the solidliquid interface travels divided by the corresponding time it takes to cover that distance. This calculation is given by the equation:

$$v_i = \frac{d_i}{t_i - t_{i-1}} \tag{6}$$

where i is the interface of interest, v_i is the solidification rate of interface i, d_i is the distance the solidification front travels from time t_{i-1} to time t_i .

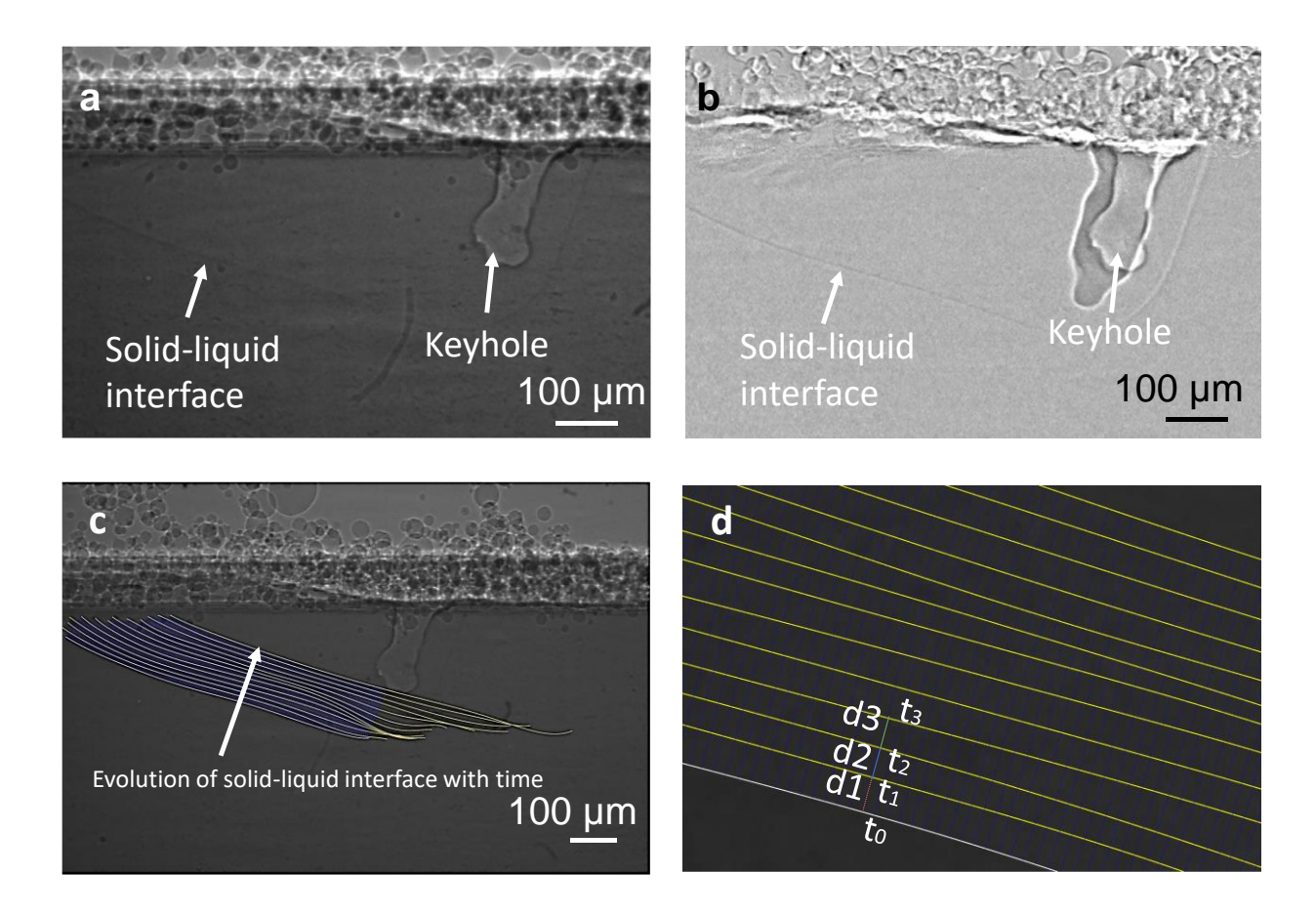


Figure 23. Solid-liquid interface evolution and method for determining the solidification rate. (a) Original X-ray image showing the keyhole and solid liquid interface during LPBF process of Al6061. (b) The result of image processing to reveal the melt pool boundary. (c) The result of curve fitting on the tracked solid-liquid interface using polynomial equation. (c) Higher magnification of (b) showing the growth trajectories of the solid-liquid interface from t_0 to t_3 .

5.1.5 Multiphysics Modelling

During laser powder bed fusion, laser/metal interactions were simulated using the FLOW-3D platform. The continuity, momentum, and energy transfer equations for incompressible laminar flow were discretized and solved using a forward time-stepping

approach. Due to significant vaporization during laser melting, it was necessary to monitor the fluid fraction and free surfaces using the VOF method. The split Lagrangian method was chosen for this setup, as it is known to produce the least amount of cumulative volume errors and numerical noise. Simulations were conducted using a multiple reflection model and incident absorption estimates based on Frensel's equations [74]. The model was calibrated using the in-situ X-ray experimental data on the length and depth of the melt pool and the depth of the depression zone. The incident laser had a circular shape with a power of 468 W, a beam size (*r*) of 90 μm, a Gaussian profile with an inflection point of 31.81 μm, and a scan speed of 0.4 m/s. The thermophysical properties used in the model were obtained from [74].

5.2. Pore Prediction

To clarify the basis for our pore prediction approach, we first reviewed the dynamics of pore formation from the keyhole. Figure 24a shows the pore formation dynamics captured during the LPBF process of Ti-6Al-4V substrate material under the frame rate of 140 kHz. At t₁, the keyhole has a low aspect ratio (depth/width) with a wide-open top, and the laser beam is directed towards the bottom of the keyhole. This directs the energy towards the bottom and causes an increase in the keyhole depth, resulting in the formation of multiple reflections at the keyhole bottom. Simultaneously, the stronger melt flow on the rear wall of the keyhole causes it to shrink, forming a *J*-shaped keyhole with a peak aspect ratio, as shown in Figure 24a, t₂. The amount of light that penetrates the keyhole is further limited, causing a decrease in the keyhole depth as well as a decrease in the keyhole aspect ratio (Figure 24a, t₃). The formation and growth of the newly born keyhole takes place within ~4 µs, which has also been observed under megahertz frame rates [34,72].

We observed the formation of a keyhole pore within the subsequent frame (Figure 24a, t₄), when the bottom part of the old keyhole with a lower temperature collapses as a spherical pore. We hypothesized that instances of pore formation can be predicted by capturing the fluctuations of the keyhole between time t₁ and t₃, during which the keyhole depth and aspect ratio reach their peaks at t₂. To this end, we developed an image processing technique to quantify the keyhole dimensions, including depth (*d*), width (*w*), and aspect ratio (*d*/*w*), in our X-ray experiments (Figure 24a, t₂). We then find the time at which the keyhole depth and aspect ratio peak at the same time (t₂), which is referred to peak position matching. The peak position matching approach has been shown in Figure 24b. The approach for prediction of solidification cracking based on the peak position matching will be discussed later.

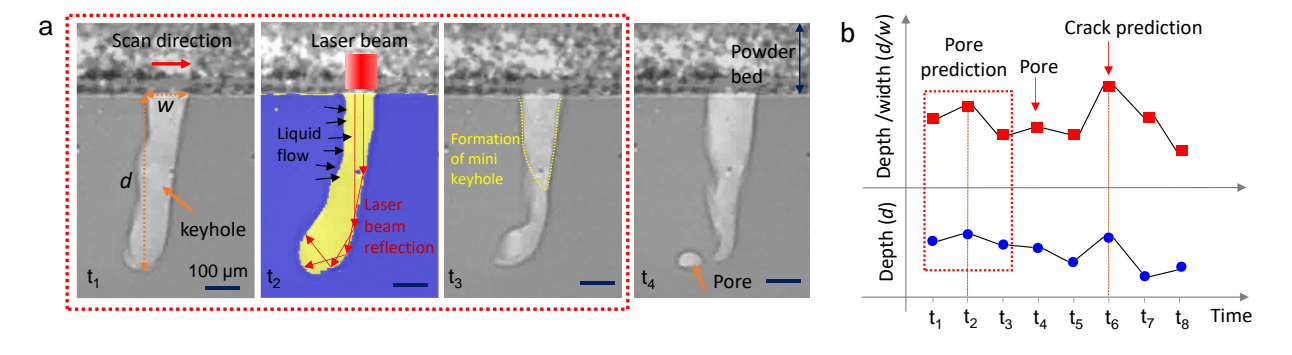


Figure 24. Defect Prediction during LPBF Process. (a) X-ray images capturing the keyhole dynamics during pore formation, showing the transition of the keyhole aspect ratio (depth/width) from a valley to a peak between time t_1 and t_3 . (b) Application of the peak position matching approach for predicting the occurrence of pores and cracks during the LPBF process. In (a, t_2) , the yellow-purple colors indicate the image processing using k-means clustering method that is overlaid on the original X-ray image. The experiment in (a) is the LPBF process of Ti-6Al-4V under laser power of 382 W, scan speed of 0.5 m/s, beam size of 90 μ m, and a frame rate of 50 kHz, which was cited from Zhao et al. (videos S1) [72].

Figure 25(a-c) depicts the measured keyhole depth, width and aspect ratio, obtained during an in-situ X-ray experiment of the LPBF process of Al6061. The experiment was conducted under the following conditions: P=501 W, v=0.4 m/s, r=100 μ m, fps=140 kHz, and an average keyhole depth of d≈218 μ m. The implementation of peak position matching technique for predicting the formation of pores has been shown in Figure 25d.

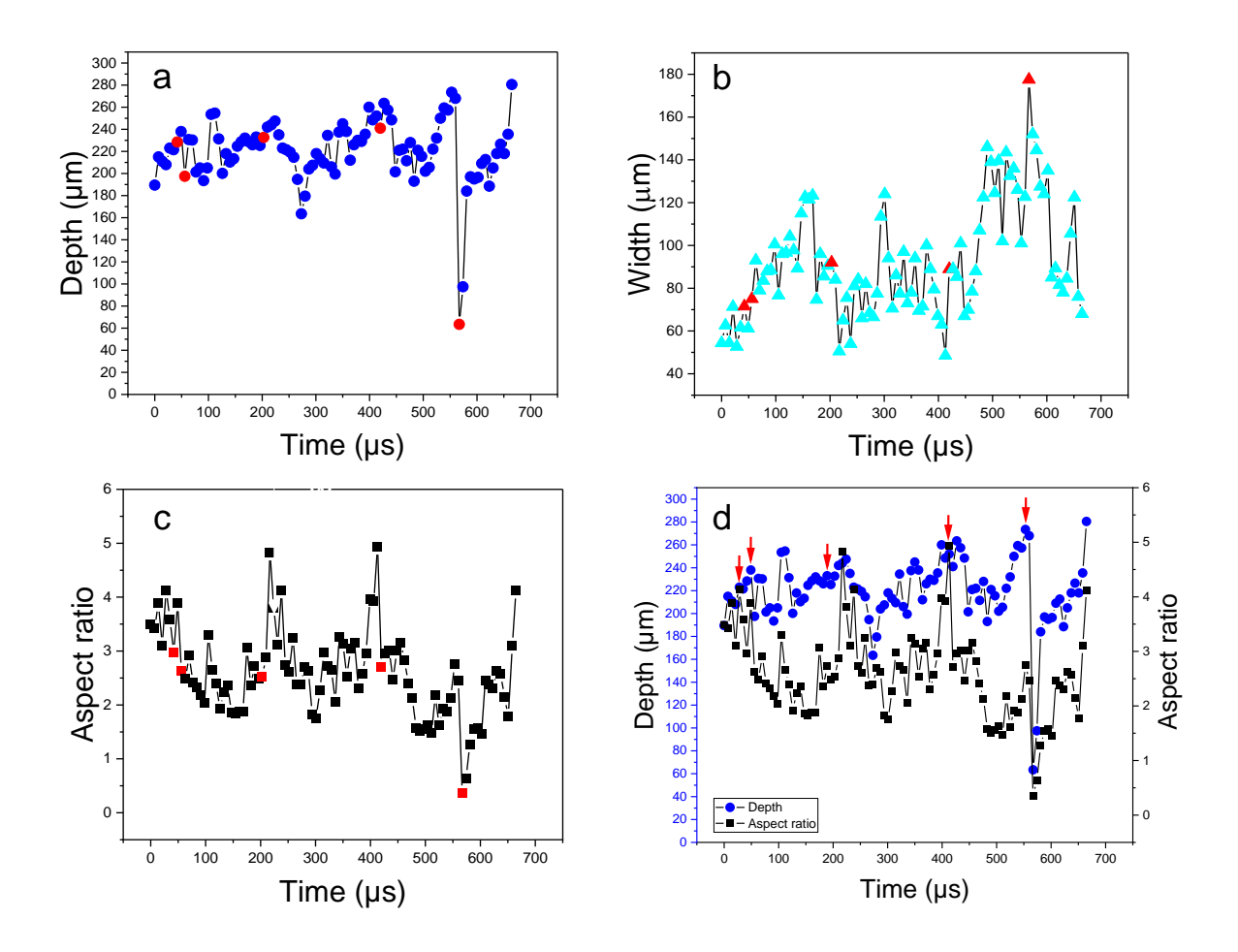


Figure 25. Keyhole geometry and peak position matching for pore prediction. Quantification of keyhole (a) depth, (b) width and (c) aspect ratio; (d) Implementation of the peak position matching. The in-situ X-ray experiment was captured during the LPBF process of Al6061, under a laser power of 501 W, scan speed of 0.4, beam size of 90 um, and frame rate of 140 kHz. The frames in which pores are observed are indicated

with red color in a-c. In (d), the arrows indicate the frames in which pores are predicted to form based on peak position matching.

The X-ray frames indicating the predicted pore moments based on peak position matching are displayed in panel (a) of Figure 26, while panel (b) displays the subsequent X-ray frame captured within 7-14 µs, in which the pore is observed.

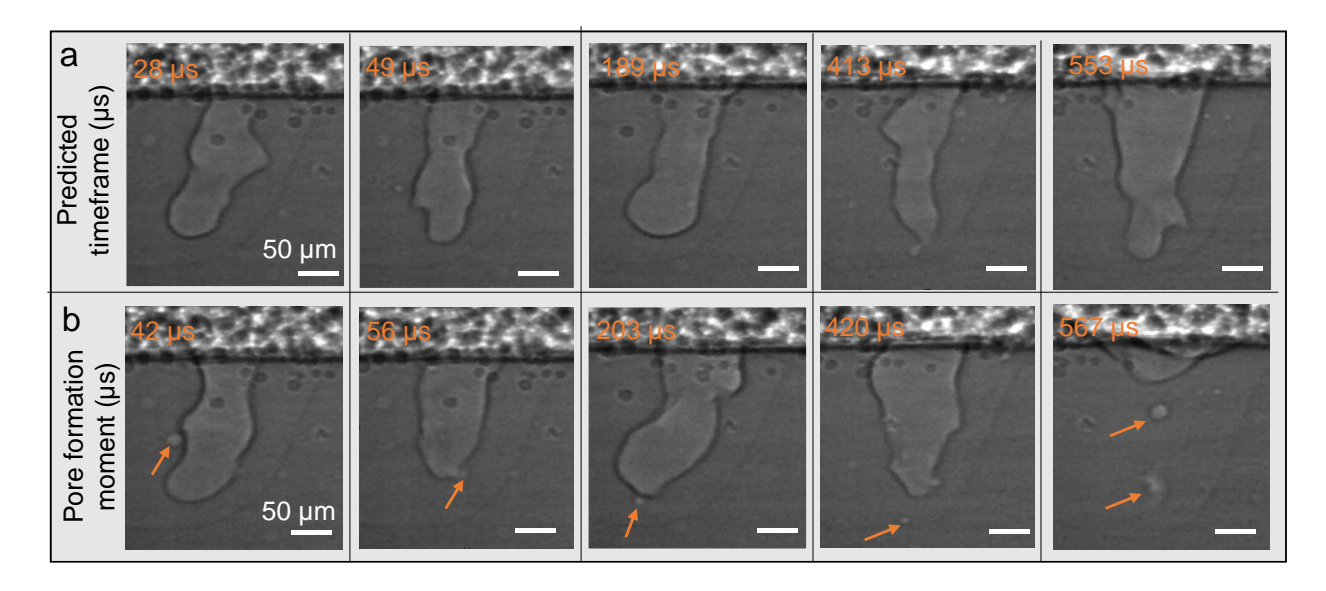


Figure 26. Pore prediction based on peak position matching. (a) X-ray frames of the predicted pore moments based on peak position matching; (b) X-ray frames on which the pore is observed. Pores are indicated by the arrows in the X-ray images. The experiment was captured during the LPBF process of Al6061, with a laser power of 501 W, scan speed of 0.4, beam size of 90 um, and frame rate of 140 kHz. All scale bars are 50 μm.

Our quantification showed that, in this case, we were able to predict pore formation with precision and recall values of 100%. We have also verified the effectiveness of the peak position matching technique for a similar average keyhole depth ($d = \sim 218 \,\mu\text{m}$) achieved under a smaller beam size ($r = 50 \,\mu\text{m}$) and different process parameters, including a laser power of 261 W, scan speed of 0.4 m/s, and frame rate of 140 kHz, as shown in Figure 27.

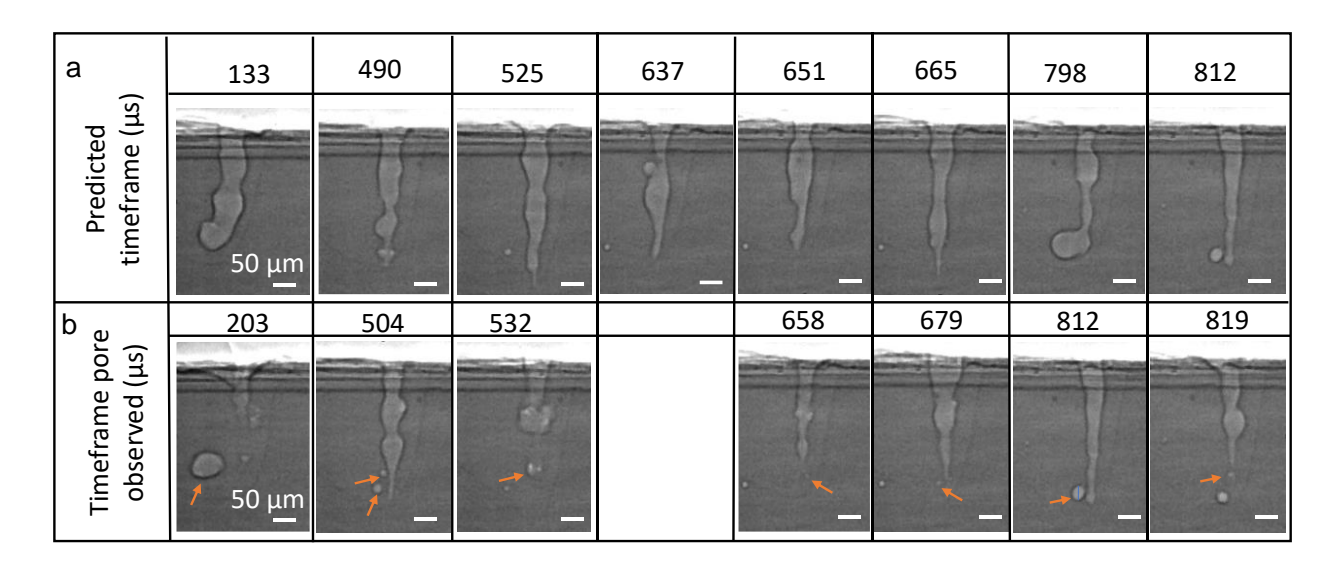


Figure 27. (a) In-situ X-ray images showing the frames where pore formation is predicted by peak position matching. (b) In-situ X-ray images showing the frames where pores are visible. The material used is Al6061, with laser power of 261 W, scan speed of 0.4 m/s, beam size of 50 μ m, and frame rate of 140 kHz. The arrows in (b) indicate the pores. The scale bar is 50 μ m.

The results showed that the precision and recall values were 87% and 100%, respectively. It is important to note that our prediction did not take into account the future evolution of the pore in the melt pool, such as subsequent pore elimination by keyhole interaction. We repeated the experiment shown in Figure 26 under the lower frame rates of 100 and 50 kHz. The results revealed a decrease in precision and recall values to approximately 60%. We plotted the precision and recall values as a function of frame rate for varying keyhole depths (*d*) during the LPBF process of Al6061, as shown in Figure 28.

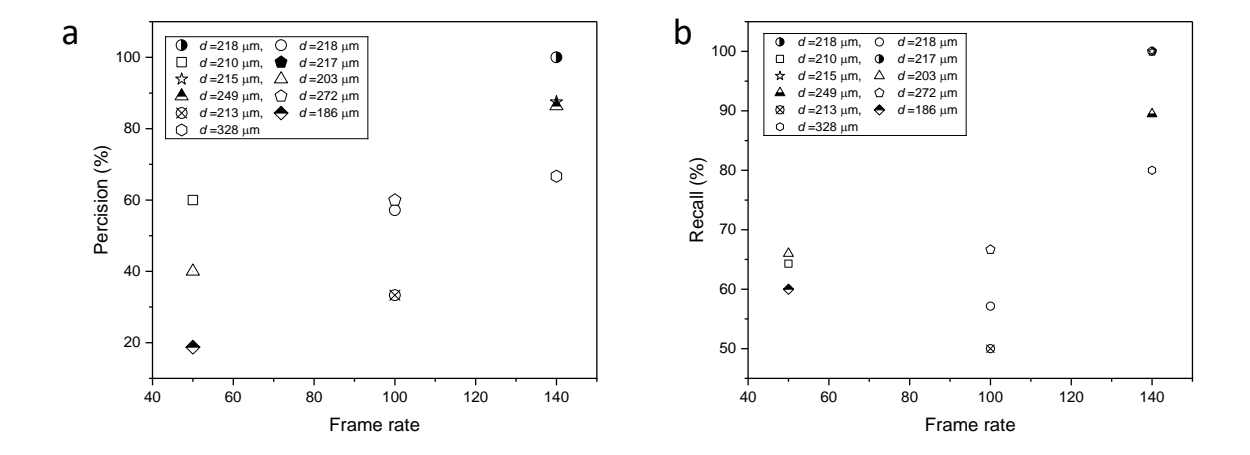


Figure 28. The accuracy of pore prediction based on peak position matching. (a) Precision and (b) recall values as function of frame rate calculated for different average keyhole depth (d) in Al6061 experiments.

Both precision and recall showed the highest values at a frame rate of 140 kHz, while there was no significant change in their values under 50 and 100 kHz frame rates. However, when the keyhole depth was at its largest value of *d*=328 µm, the accuracy of the prediction decreased because the pore separated from the keyhole, interacted with the keyhole tip again, and caused a change in the keyhole morphology. This condition has been shown in Figure 29.

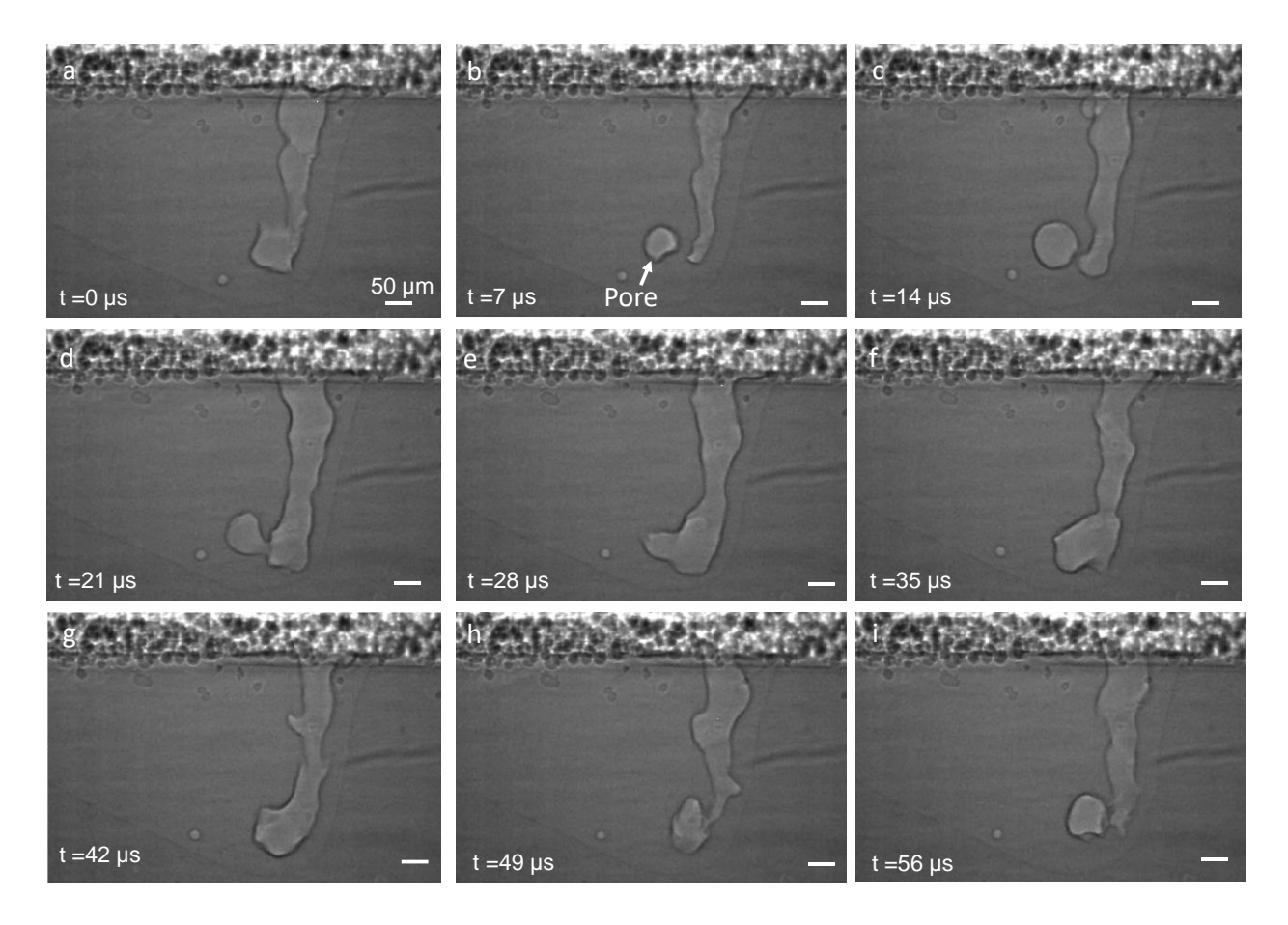


Figure 29. Pore formation and reattachment to the keyhole when the keyhole is deep. In this process, the keyhole pore is formed at $t=7~\mu s$ and then merges into the keyhole from t=14 to $t=21~\mu s$. The pore starts to detach from the keyhole again at $t=49~\mu s$. The experiment was captured during the LPBF process of Al6061 with a laser power of 600 W, scan speed of 0.4 m/s, beam size of 50 μm , and frame rate of 140 kHz. The scale bars in all images are 50 μm .

To evaluate the effectiveness of our technique, we combined our experimental data on Ti-6Al-4V with data from Zhao et al. (videos S1, S2, and S4 [72]), and conducted peak position matching at a frame rate of 50 KHz. Our quantitative analysis demonstrated that the peak position matching technique can predict pore formation in Ti-6Al-4V with precision and recall values between 55% to 85% at a frame rate of 50 kHz, as presented in Table 2. An example of pore prediction from experiment S3 is illustrated in Figure 30.

Table 2. The results of precision and recall for LPBF process of Ti6Al4V. S1, S2 and S3 were cited from [72].

Experiment	Frame rate	Precision	Recall	Material	keyhole depth (um)
S1	50	64	55	Ti-6Al-4V	442
S2	50	70	75	Ti-6Al-4V	433
S3	50	78	83	Ti-6Al-4V	580
S5	50	75	86	Ti-6Al-4V	491
S6	50	53	62	Ti-6AI-4V	366

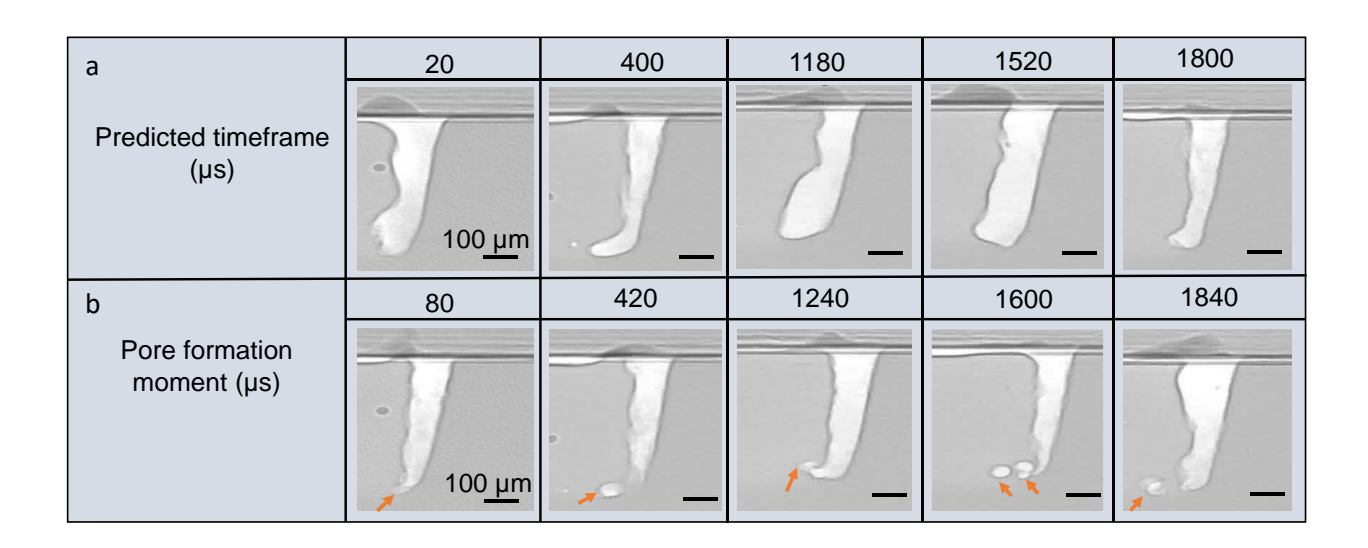


Figure 30. Pore prediction using peak position matching for Experiment S3. (a) In-situ X-ray images displaying the predicted pore frames based on peak position matching, and (b) in-situ X-ray images of the frames in which the pores are observed within the track. The in-situ X-ray experiment was conducted during the laser melting of Ti-6Al-4V at a laser power of 382 W, scan speed of 485 mm/s, beam size of 100 μm, and a frame rate of 50 kHz. The data was sourced from Zhao et al. [72]. In panel (b), the orange arrows show the pores.

5.3. Pore Size Prediction

Figure 31a shows the X-ray images of the keyhole dynamics when the keyhole aspect ratio changes from low (valley) to high (peak) captured during the LPBF process of Ti-6Al-4V (P=364 W, v=0.4 m/s, fps=140 kHz). Before pore formation, the keyhole shrinks

in width and increases in depth to form a pinched off cavity at the bottom that ultimately detaches as the pore. Figure 31d shows the change in the top width of the keyhole (w) and the average length (1) of the cavity at the keyhole bottom over time. As the keyhole aspect ratio changes from low to high, the keyhole width is observed to decrease at a constant ratio of $W_{t+1}/W_t \approx 0.9$ (Figure 31d). However, due to the changing balance between the downward traveling recoil pressure and the reverse backflow, the fluctuation in the length of the cavity at the bottom (I) is not constant [75]. We measured the velocity of the traveling recoil pressure to be approximately 14 m/s, and its impact location in each frame is indicated by blue arrows in Figure 31a. At the point where the keyhole has the lowest aspect ratio (Figure 31a, t=0 µs), the length of the keyhole's bottom is almost equal to the width of the keyhole's top. The keyhole begins to shrink within 7 µs, while the effect of the travelling recoil pressure is still at mid-keyhole depth (Figure 31a, t=7 µs). As the recoil pressure continues to travel downwards (Figure 31a, t=14 µs), the length of the cavity at the bottom increases to a value close to its primary length, due to the formation of multiple reflections within the cavity and the formation of the stagnation point [9]. At t=21 µs, the cavity begins to shrink again as the impact of the travelling recoil pressure dissipates. As the newborn keyhole emerges, the length of the bottom cavity increases slightly to a value close to the width of the keyhole at its top (Figure 31a, t=28 µs).

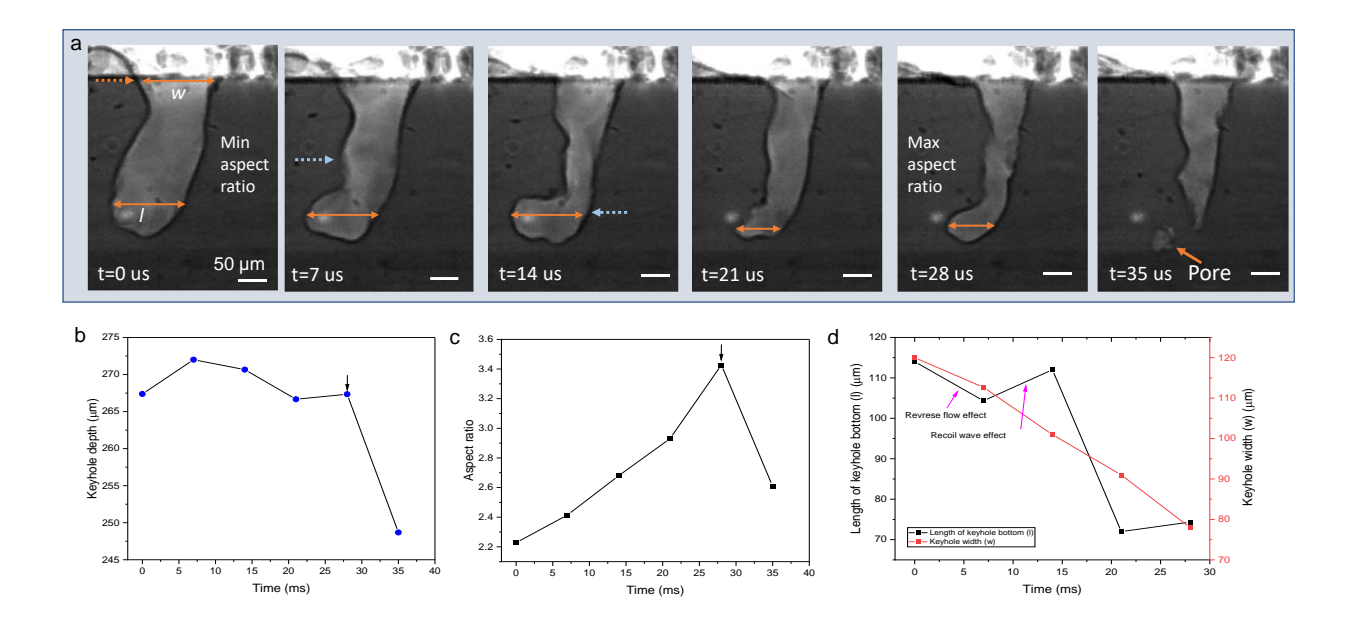


Figure 31. (a) The dynamic X-ray images showing the evolution of the keyhole from its minimum aspect ratio to the peak aspect ratio. The change in (b) keyhole depth, (c) keyhole aspect ratio, and (d) in keyhole topmost width and length (l) of the cavity at the bottom prior to pore formation. Blue arrows denote the approximate location of the traveling recoil pressure. The black arrows in b and c show the peak position matching for the pore formation. The experiment is the LPBF process of Ti-6Al-4V at laser power of 365 W, scan speed of 0.4 m/s and the frame rate of 140 kHz.

It is speculated that the ratio of the keyhole width at its valley (w_v) to the width at its peak (w_v) , represents the ratio of shrinkage in the lowermost cavity, which also corresponds to the horizontal diameter of the pore. As such, the ratio of depth at the keyhole aspect ratio peak (d_p) to the keyhole aspect ratio in the valley (d_v) , demonstrates the increase in the keyhole depth, which in turn corresponds to the vertical diameter of the pore. We defined the Peak Valley ratio (PVR) by calculating the ratio of the aspect ratio at the peak $(\frac{d_p}{w_p})$ to its nearest pervious aspect ratio at valley $(\frac{d_v}{w_v})$, for the observed pore instances in our LPBF experiments. The equivalent pore diameter was calculated using $\sqrt{\frac{4A}{\pi}}$, where A is the pore area measured directly from our X-ray images. Figure 32 demonstrate a linear

correlation between the keyhole parameter and the size of the keyhole pore for both the Al6061 and Ti-6Al-4V experiments. It is crucial to capture the size of the pore early as it separates from the keyhole, since the pore size continues to change until it is fully captured by the solid-liquid interface [76]. As a result, we speculate that curve fitting accuracy will improve and R² values will increase with the use of a higher frame rate.

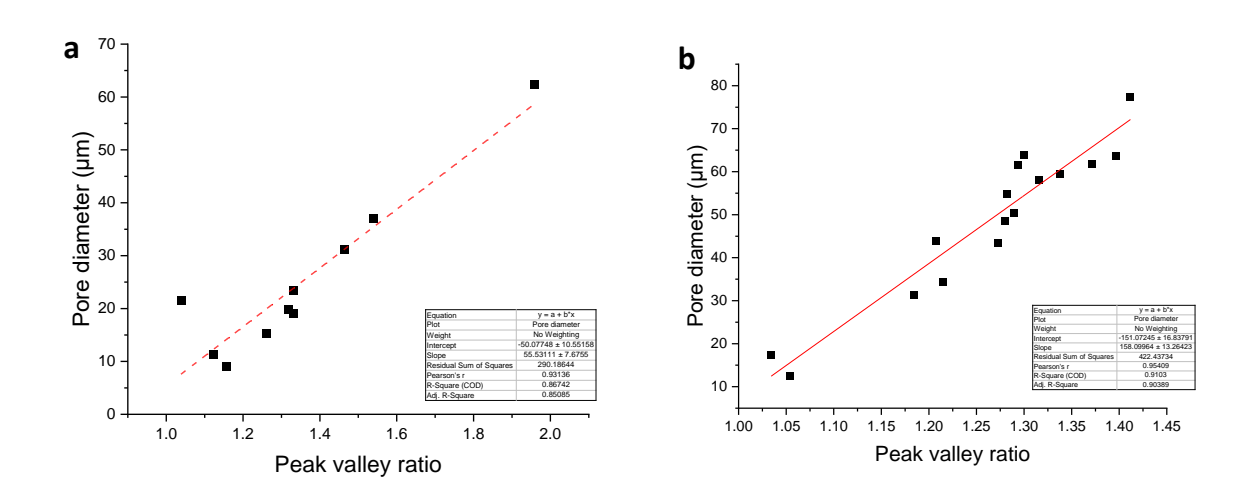


Figure 32. Relationship between pore diameter and Peak to Valley ratio (PVR) for keyhole pore instances observed during the in-situ X-ray experiment of LPBF process of (a) Al6061 and (b) Ti-6Al-4V as predicted by our analysis.

5.4. Solidification Cracking Dynamics

We studied the dynamics of the solid-liquid interface at the crack location during the insitu X-ray imaging of the LPBF process of Al6061. The process parameters used (P = 468 W, v=0.4 m/s, $r=90 \text{ }\mu\text{m}$, fps=50 kHz) resulted in a melt pool with an average keyhole depth of $d=213 \text{ }\mu\text{m}$, as presented in Figure 33a . The study of solidification dynamics was conducted in this research because there exists a direct correlation between crack susceptibility and solidification velocity [77].

During the LPBF process of Al6061, the crack initiates approximately 75 \pm 15 μ m normal distance from the solid-liquid interface and propagates at an angle of 16° from the reference line towards the top of the substrate Figure 33(a). We measured the velocity of the solid-liquid interface by calculating the normal distance it traveled along five equidistant points (P₁-P₅) within a 400 μ s time frame while passing from the future crack initiation point, as shown in Figure 33b. P₁ was specifically selected along the crack propagation direction. During the selected time frame, we observed that the solid-liquid interface coincided with the site of crack initiation at approximately t = 120 μ s.

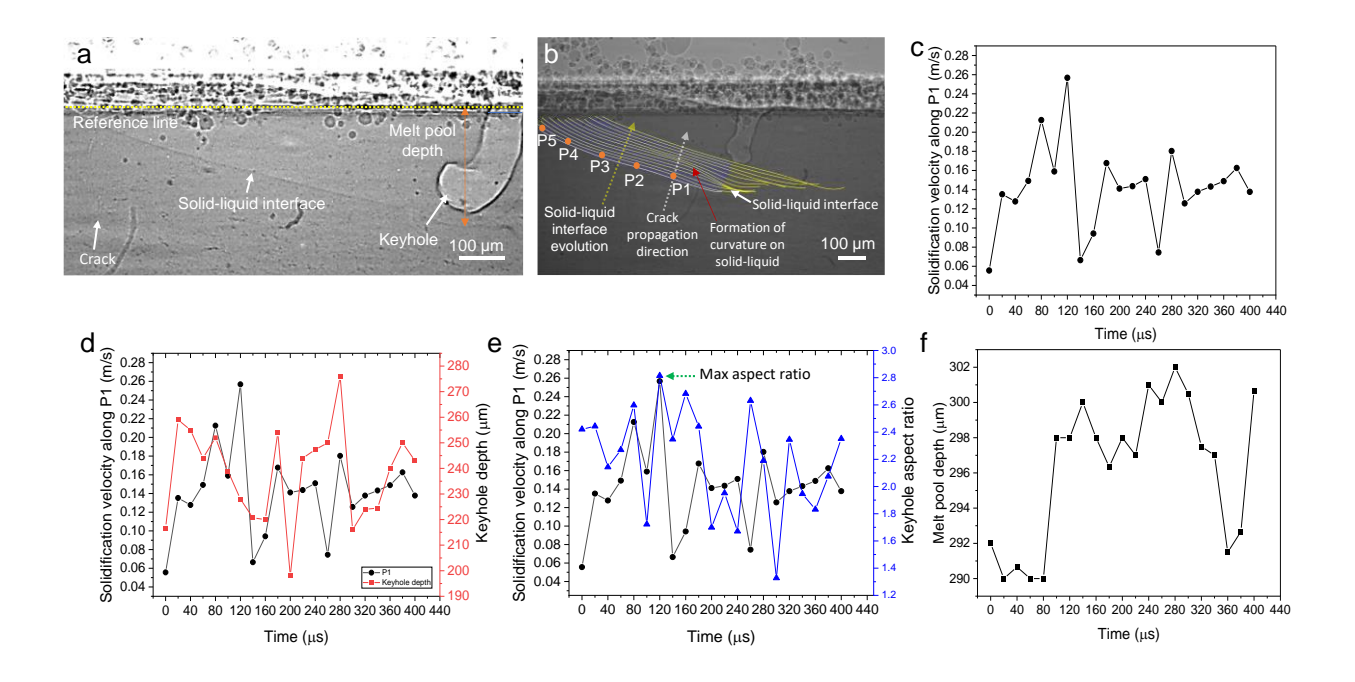


Figure 33. The dynamics of solid-liquid interface during solidification cracking. (a) X-ray image shows the formation of solidification crack after the solid-liquid interface has moved away from the crack initiation site. (b) Evolution of solid-liquid interface using the ninth-order polynomial fit. (c) Solidification velocity along P_1 . (d) Solidification velocity along P_1 and keyhole depth fluctuations. (e) Solidification velocity along P_1 and keyhole aspect ratio. (f) Melt pool depth as a function of time. The experiment is the LPBF process of

Al6061 at laser power of 468, scan speed of 0.4 m/s, laser beam size of 90 μ m, and frame rate of 50 kHz.

The solidification velocity along P₁ has been displayed in Figure 33c. Initially, at t=0 µs, the solidification velocity is low, at 0.05 m/s. As the solid-liquid interface advances from the crack initiation site, the solidification velocity increases and reaches a maximum value of 0.26 m/s. This occurs at a later time, specifically at t=120 µs. We have observed that the increase in solidification velocity coincided with the formation of curvature on the solidliquid interface, as demonstrated in Figure 33b. The analysis revealed an interesting relationship between solidification velocity along P₁ and changes in keyhole depth, as depicted in Figure 33d. Specifically, we observed nearly harmonic fluctuations between solidification velocity along P₁ and changes in keyhole depth. On the other hand, the solidification velocity along P₂-P₅ mimicked the keyhole fluctuations but with some delay, as shown in Figure 34. Furthermore, we found that the maximum solidification velocity was associated with the formation of the maximum keyhole aspect ratio, as shown in Figure 33e. The melt pool depth was also quantified withing the same time frame, as presented in Figure 33f. We observed a significant increase in melt pool depth at the time when the curve forms on the solid-liquid interface (Figure 33f, $t=80 \mu s$).

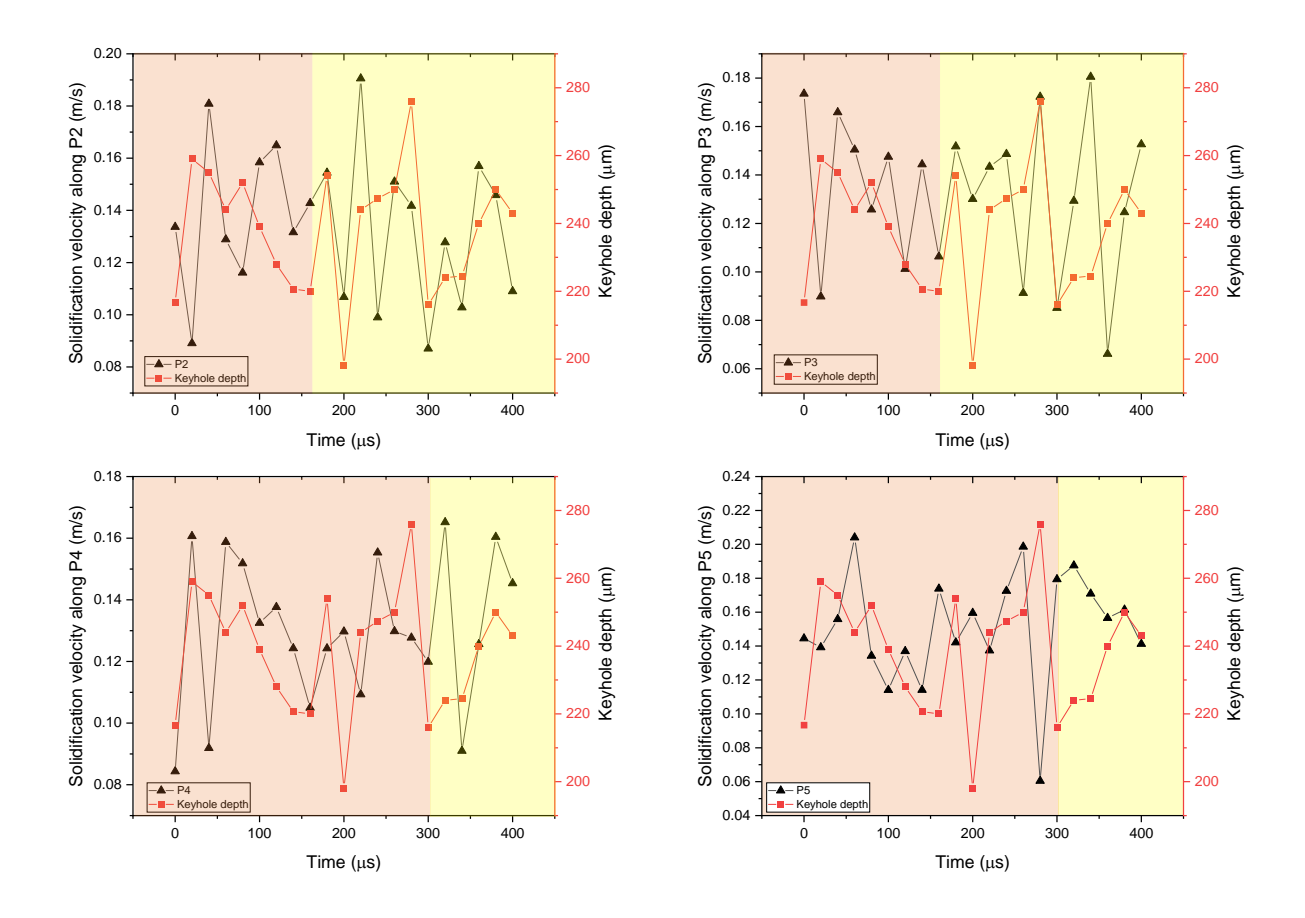


Figure 34. The variation of solidification velocity along P_2 - P_5 and fluctuation of keyhole depth over time. The highlighted area in pink shows the time when solidification velocity is not harmonious with the keyhole fluctuations, while the area highlighted in yellow shows the harmony between keyhole and solidification.

5.5. The Mechanism of Formation of a Curved Interface

To further investigate the mechanism behind the formation of a curved area on the solid-liquid interface, it is beneficial to analyze the trends in keyhole and melt pool fluctuations. The trends in keyhole and melt pool fluctuations every 80 μ s are presented in Figure 35. As shown in Figure 35a, the keyhole depth increased significantly from 215 μ m at t=0 μ s to around 252 μ m at t=80 μ s, which coincides with the time when the solidification velocity exhibited the first major peak. At this time, the distance between the tip of the keyhole

and the bottom of the melt pool (i.e., the difference between keyhole depth and melt pool depth) reached a minimum (Figure 35c). This marks the initiation of the curvature on the solid-liquid interface.

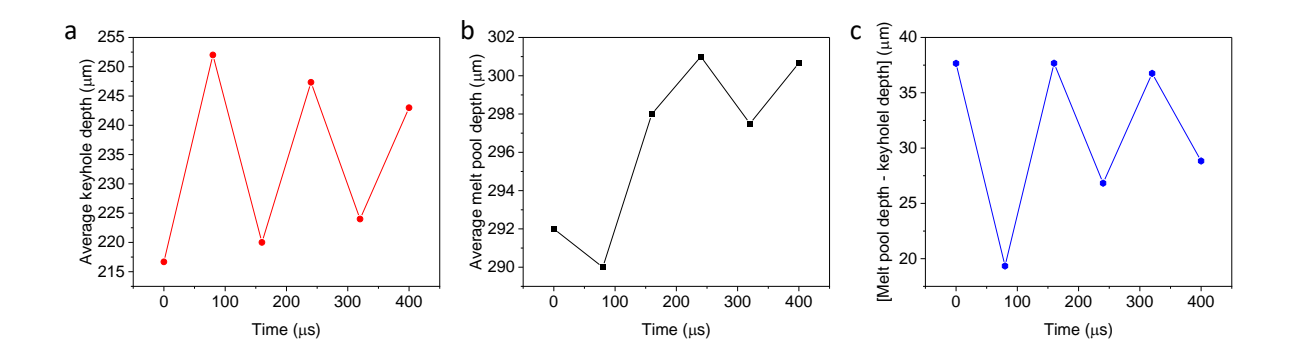


Figure 35. (a) The average keyhole depth (b) the average melt pool depth, and (c) the difference between the melt pool depth and keyhole depth. The in-situ X-ray experiment is the same experiment shown in Figure 33.

We conducted a multiphysics simulation using FLOW-3D to examine the melt flow dynamics during the transition of the keyhole from shallow to deep in the LPBF process of Al6061. The results are depicted in Figure 36.

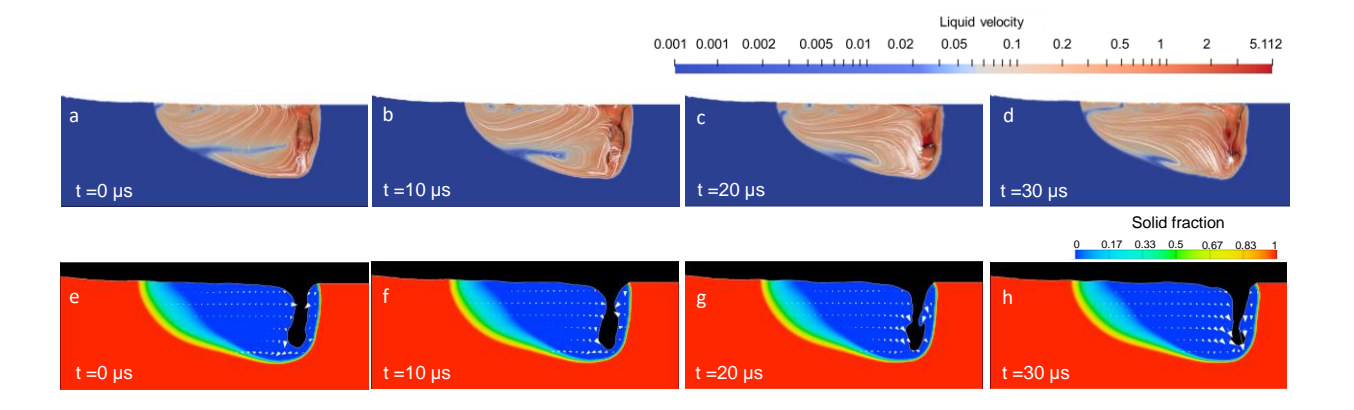


Figure 36. FLOW-3D multiphysics simulation of the LPBF process of Al6061 when the keyhole depth changes from shallow to deep. (a-d) The melt flow streamlines (shown in white lines) and the magnitude (shown with colormap) within the melt pool. (e-h) The

direction and magnitude of the melt flow (indicated with white arrows) and amount of solid fraction (indicated with color map) at different locations in the melt pool. The size of the arrows in e-h corresponds to the magnitude of the melt flow velocity. The laser parameters used for simulation and in-situ X-ray experiments were laser power of 368 W, scan velocity of 0.4 m/s, and beam size of 90 µm.

The simulation findings demonstrate that when the keyhole is still shallow, it drives the liquid melt flow downwards towards the bottom of the melt pool (Figure 36, t=0 μ s). The high-velocity hot liquid flow along the solid-liquid interface acts to maintain its smoothness. As the depth of the keyhole increases (Figure 36, t=10 μ s), the solid-liquid interface below the keyhole, i.e., melt pool depth, does not increase rapidly and is adjusted within 20 μ s (Figure 35b, t=80 μ s). At this stage, the increase in melt flow velocity behind the depression zone rear wall narrows the keyhole into a thin channel, resulting in the formation of a keyhole with a higher aspect ratio. Furthermore, the reduction in velocity of the backward flow that transports the high-temperature liquid along the interface causes variations in temperature gradient and the emergence of a region characterized by rapid solidification, as depicted in Figure 36 at t=20 μ s. As P1 is located closest to the keyhole, any decrease in flow velocity is first observed at this point.

5.6. Hot Cracking Sensitivity

Various models have been proposed for hot tearing in castings, and some of them have been applied to solidification cracking in welding. Eskin et al. [78] reviewed several hot tearing models proposed by various researchers, including stress-based models, strain-based models, and strain rate-based models. Stress-based models assume that a semisolid will crack when tensile stresses exceed their strength. Strain-based models, on the other hand, assume that a semisolid will crack when tensile strains are sufficient to

break the grain-boundary liquid films. However, recent studies have shown that the strain rate, rather than the strain itself, plays a critical role in cracking during solidification. Matsuda et al. [79] and Coniglio and Cross [80] confirmed the existence of a critical strain rate above which cracking occurs during solidification in welding experiments.

The model proposed by Prokhorov [81] mainly focuses on the thermomechanical factor of cracking, assuming that cracking can occur if the rate of strain accumulation with temperature drop $d\varepsilon/dT$ exceeds a critical value. On the other hand, Feurer's model [78] mainly focuses on the liquid feeding of the shrinking mushy zone. The model, in the form of an empirical formula, assumes that cracking can occur if volumetric shrinkage exceeds volumetric feeding. To include tensile deformation, Nasresfahani et al. [82] revised Feurer's model into another empirical formula that includes a uniaxial contraction stress measured during casting.

The RDG model, proposed by Rappaz, Drezet, and Gremaud [83], considers both uniaxial tensile deformation and shrinkage feeding and has a physically sound basis [84]. It has been widely used to predict crack sensitivity in laser welding of alloys [85]. The RDG model is schematically shown in Figure 37. The model assumes the growth of columnar dendritic grains in one direction, with tensile deformation acting normal to the growth direction and liquid feeding in the opposite direction. The model proposes that cracking occurs when the pressure within the interdendritic liquid of the mushy zone drops below the cavitation pressure, leading to the formation of voids. The nucleation of cavities in the presence of thermal strains can eventually cause hot cracking as the liquid has no mechanical resistance.

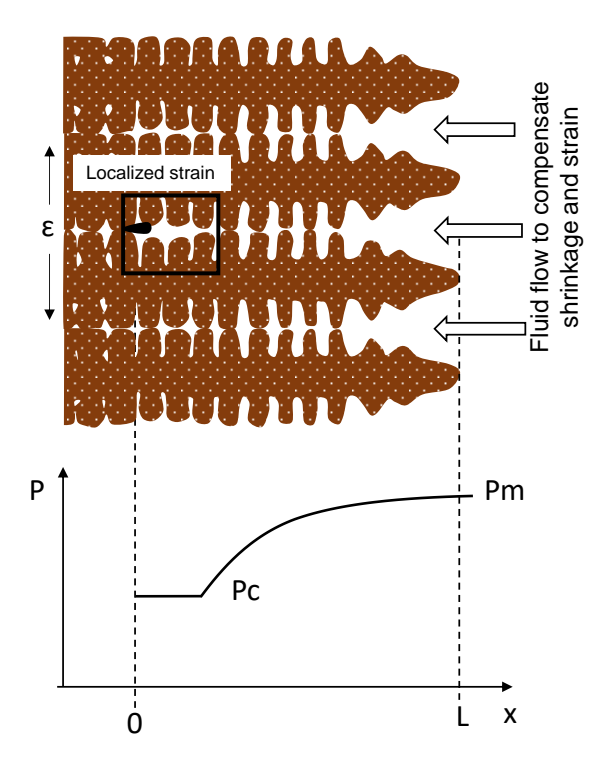


Figure 37. Schematics of the RDG model showing the formation of hot tear in between columnar dendrites. The figure in [83] was used as a basis for reproducing this figure.

Based on the RDG model, the total pressure drop, Δp_{total} , is the result of two contributions:

$$\Delta p_{total} = \Delta p_{deformation} + \Delta p_{shrinkage} = \Delta p_c = p_m - p_c \tag{7}$$

where, $\Delta p_{deformation}$ is the pressure drop contribution associated with solid deformation, $\Delta p_{shrinkage}$ is the pressure drop contribution associated with liquid shrinkage, $p_{\rm m}$ is the metallostatic pressure, $p_{\rm c}$ is the cavitation pressure and $\Delta p_{\rm c}$ is the cavitation depression of the liquid.

 $\Delta p_{total} \, \mathrm{can}$ be calculate using the following equation:

$$\Delta p_{total} = \frac{180}{\lambda^2} \frac{(1+\beta)\mu}{G} \int_{T_s}^{T_l} \frac{E(T)f_s(T)^2}{(1-f_s(T))^3} dT + \frac{180}{\lambda^2} \frac{v\beta\mu}{G} \int_{T_s}^{T_l} \frac{f_s(T)^2}{(1-f_s(T))^2} dT$$
 (8)

with
$$E(T) = \int_{T_s}^{T_l} f_s (T) \dot{\varepsilon}(T) dT$$
 (9)

where, β is the solidification shrinkage coefficient, μ is dynamic viscosity, $f_s(T)$ is fraction of solid as a function of temperature, G is temperature gradient, v is solidification front velocity, T_1 is the liquidus temperature and T_s , also known as coalescence temperature, is the temperature at the end of solidification beyond which feeding problems are no longer considered. $\dot{\varepsilon}(T)$ is strain rate in the solid dendrites normal to growth direction which is assumed to be temperature dependent and is given by [86]:

$$\dot{\varepsilon} = \alpha G v \ (s^{-1}) \tag{10}$$

where, α is thermal expansion coefficient and λ is primary dendrite arm spacing (PDAS) and can be calculated by [87]:

$$\lambda = 43.2 \times 10^{-6} \times (Gv)^{-0.324} \tag{11}$$

We used (RDG) model to calculate the amount of pressure drop at the crack location during the LPBF process. The constants required for implementing the RDG criterion include the shrinkage factor (β) and dynamic viscosity (μ). The shrinkage factor is calculated as $\beta = \frac{\rho_s}{\rho_t} - 1$, where ρ_s and ρ_t represent the density of solid and liquid, respectively. In this study, the values of β and μ were set to 0.065 and 1.4×10⁻³ Pa.s, respectively, as reported in reference [77]. The average temperature gradient at the crack area was estimated using multiphysics simulation. We estimated the average temperature gradient at the curvature location (P₁) to be 1.7×10⁻⁶ K/m. The $f_s(T)$ data for Al6061 was obtained from [84]. According to our simulation results, the change in liquid pressure within the mushy zone occurs approximately at a solid fraction of f_s =0.25, at a

temperature of T=916 K. We have designated this temperature as Ti. In addition, we have considered the coalescence temperature (Ts) to be 867 K, based on the experimental evidence that coalescence occurs at a solid fraction of fs=0.97 [77].

Using the RDG model, we have estimated the pressure drop at P_1 to be 1.7×10^7 Pa when the solidification velocity is 0.26 m/s and the temperature gradient is 1.7×10^6 K/m. In contrast, when the average solidification velocity is 0.13 m/s, the pressure drop is estimated to be 6.7×10^6 Pa, which is approximately 2.5 times smaller than the pressure drop at the higher solidification velocity. It is worth noting that estimating the threshold pressure drop at which cavity formation occurs is challenging because the model relies on average values taken along the mushy zone from the simulation data.

5.7. Peak Position Matching for Crack Prediction

By examination of crack formation at a higher frame rate of 140 kHz, we have discovered that the peak position matching technique can also be used to predict the formation of cracks. The phenomenon is exemplified in Figure 26a at 413 μs, where the curvature forms when the maximum aspect ratio peak of the keyhole coincides with a peak in depth. As predicted by peak position matching, the pore forms at 420 μs, which eventually resided near the future crack area, as shown in Figure 38. This may provide an explanation for the presence of pores observed at crack locations in previous studies [88].

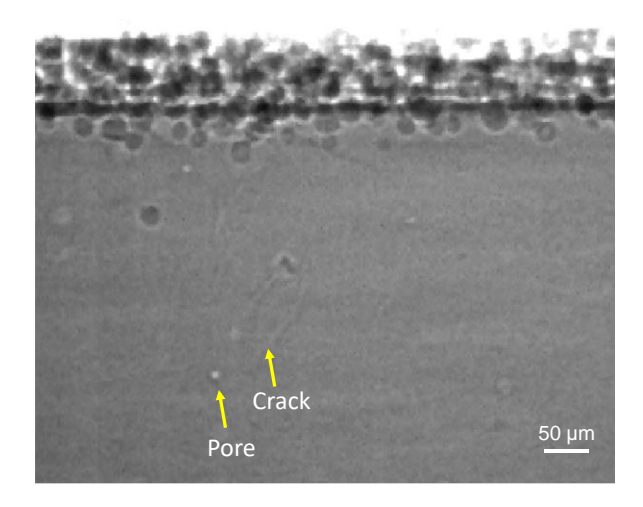


Figure 38. The formation of pore near the crack area captured during the in-situ X-ray experiment of the LPBF process of Al6061, under a laser power of 501 W, laser scan speed of 0.4 m/s, beam size of 90 um, and frame rate of 140 kHz.

5.8. Summary of Defects Prediction during Metal Additive Manufacturing

In our study, we utilized the in-situ X-ray monitoring technique to investigate melt pool and keyhole dynamics and develop innovative methods for predicting keyhole pores and solidification cracks. The following results were obtained:

- (1) We developed an approach to predict keyhole pore formation by analyzing keyhole dynamics during the pore formation moment. The approach involves finding a match between the keyhole depth peak and the keyhole aspect ratio peak, and demonstrated remarkable accuracy in forecasting pore formation, particularly at higher frame rates.
- (2) We developed a dimensionless Peak to Valley Ratio (PVR) number that reflects the extent of variation in keyhole aspect ratio before the formation of keyhole pores. This number can be used as a predictor of pore size for various alloy systems.
- (3) We studied the solidification dynamics during the LPBF process to identify the correlation between solidification velocity, melt pool, and keyhole dynamics. We observed

rapid solidification near the keyhole at the crack initiation point, which was linked to the formation of curvature on the solid-liquid interface. This phenomenon occurred when the keyhole aspect ratio reached its maximum value throughout the data.

(4) The correlation between defect formation and melt pool signatures is critical for the development of closed-loop control systems. Such systems can anticipate the need for local variation during the build process, ultimately improving the quality of the final product.

Chapter 6: Conclusions of this work

Laser powder bed fusion (LPBF) is a metal additive manufacturing (AM) technology that has revolutionized the parts manufacturing industry. Unlike conventional manufacturing techniques, LPBF prints materials and parts directly from a computer-aided design file, which offers unique advantages of design freedom for complex geometries without the need for tooling. However, the extreme thermal conditions involved in the printing process can trigger transient phenomena and complex structural dynamics, inducing defects such as porosity and cracks that can deteriorate the mechanical performance of the printed parts. Studying subsurface dynamics is unfortunately challenging due to the nontransparency of metals to visible light. This challenge can induce uncertainty in understanding the mechanisms behind defect formation, making it difficult to mitigate them effectively. This dissertation utilizes the in-situ high-energy synchrotron X-ray imaging as the core process-monitoring technique to overcome the challenges mentioned above. With high temporal resolution (up to 1 MHz) and high spatial resolution (down to 1 µm pixel size), this technique is used to study pore formation dynamics in Chapter 3, pore evolution and pore mitigation dynamics in Chapter 4, and develop a model for predicting defects such as keyhole pores and solidification cracks in Chapter 5.

In Chapter 3, pore formation dynamics was studied by conducting over 1000 in-situ X-ray experiment. Overall, 6 pore formation mechanisms were observed: the identified mechanisms include pore formation from feedstock powders, keyhole pore, pore induced by surface fluctuations, pore due to shallow depression zone fluctuations, pore from the crack and pore due to vaporization or expansion of tiny gas element. Each mechanism was described in detail with accompanying figures and results from experiments

conducted on various materials and processing parameters. Out of the six categories mentioned, four types of pores (pores from feedstock, pore induced by crack, pore induced by shallow depression fluctuations and gas pores due to vaporization or expansion) are caused by materials, while the other two are induced by processing parameters. Gas pores inside the melt pool are primarily caused by the presence of gas pores in the feedstock powder. Our research showed that these gases can be captured by the strong melt flow and transferred into the melt pool, making it difficult for them to escape. Therefore, selecting high-quality raw materials is crucial to avoid the formation of these types of gases. Additionally, our results emphasized the need to identify effective mechanisms for removing pores from the powder layer before they are captured into the melt pool, which was discussed in Chapter 4.

Chapter 3 also presented our findings on the three mechanisms by which the deepnarrow depression zone, known as the keyhole, can cause pore formation. Type I, in which a keyhole can fluctuate and induce pores from its tip, seems to be the most frequent type of keyhole pore formation. This is because the keyhole can fluctuate multiple times and causes multiple pores within the melted track. Therefore, it is crucial to develop a prediction model to determine the location and size of these pores in the printed layer, as discussed in Chapter 5.

Furthermore, our research discussed the formation of pores from cracks, such as solidification cracks. It was revealed that cracks, which are one of the primary defects in the printed parts, can also cause other defects, such as pores. Therefore, understanding the dynamics of crack formation during metal additive manufacturing is necessary to predict their formation, as discussed in Chapter 5.

In Chapter 4, we studied the dynamics of pore movements inside the melt pool to understand the governing forces on pore movements in the LPBF process. Our findings showed that pore movement inside the microscale melt pool varies with location. We identified two main regions: the circulation domain, where pores circulate, and the laser interaction domain, where pores can mostly escape from the keyhole front wall. Complementary melt flow tracing experiments highlighted the magnitude and direction of the melt flow at different locations of the melt pool. It was found that the area near the laser interaction region had the highest melt flow speed, and the melt flow decreased as it moved towards the tail. Simulation also demonstrated the magnitude of the temperature gradient inside the melt pool. The area near the laser interaction region had the highest magnitude of temperature gradient, with the direction normal to the front wall of the depression zone. By comparing the direction of pore movement with the direction of temperature gradient, we discovered that the thermocapillary force governs the pore movement at the laser interaction region, while the drag force is dominant behind the depression zone. In conclusion, we have demonstrated the effectiveness of the thermocapillary force pore elimination mechanism through experiments and by printing a part, which effectively removed pores from the melt pool and powder layer.

In Chapter 5, by quantifying the change in keyhole geometry, a prediction model for keyhole pore type I was introduced. In particular, it was found that pore formation proceeds when the keyhole has a peak in aspect ratio (depth/width) and depth at the same time. The method was proved that it can predict pore formation with high precision specifically under high frame rate. Furthermore, we found that the change in keyhole aspect ratio prior to pore formation is correlated with the size of the resulting pore.

Another goal in Chapter 5, was to identify the precursors responsible for the formation of solidification cracks during the LPBF process by quantification of the solidification dynamics and keyhole geometries. Our findings indicated that the initiation point of cracks is associated with rapid solidification, which is manifested in the form of curvature on the solid-liquid interface near the keyhole. Upon further analysis of the keyhole depth, we discovered that a high solidification velocity is triggered when the keyhole depth exceeds a certain threshold. By employing a commonly used model for estimating solidification crack sensitivity, we have shown that the pressure drop required for cavity formation in the mushy zone is higher at crack initiation site with higher solidification velocity, as compared to the point with lower solidification velocity.

Chapter 7: Recommendations for Future Work

This dissertation offers insights into the formation and evolution of defects, pores, and cracks during the LPBF process. However, there are several opportunities for future work.

In Chapter 3, we investigated different mechanisms that lead to pore formation on various substrate materials. To accurately determine the severity and size of pores formed by each mechanism on different substrate materials, it is, however, essential to conduct further statistical quantification analysis. For example, it is crucial to compare the quantity and size of pores generated under surface fluctuations with those formed from the keyhole collapse (keyhole type I and II). In this chapter, we have also categorized pore formation mechanisms into material-induced and processing-induced mechanisms. An important potential study will be to investigate the correlation between these two categories. For example, it is important to determine the number and severity of pores transferred from the powder layer to the melt pool under different laser processing conditions, including conduction or keyhole mode. This can help in identifying the dominant pore formation mechanism and optimizing the laser processing parameters to reduce the number and severity of pores in the final printed part.

In Chapter 4, we identified the thermocapillary force pore elimination mechanism as the dominant approach for eliminating pores and enabling the production of pore-free parts in the LPBF process. We successfully printed a high-density aluminum alloy part using our in-house built machine, which provided us with the flexibility to adjust the laser parameters. However, commercially available printing machines may have more limited options for adjusting these parameters. Therefore, a future study could explore the implementation of this pore-elimination approach in such machines.

In Chapter 5, we developed a defect prediction model based solely on keyhole geometry, particularly the keyhole top width and depth. The next valuable research step in this regard would be to implement this model in closed-loop monitoring systems. Currently, significant progress has been made in developing prediction models based on measuring the keyhole width using thermal images from near-infrared (NIR) cameras. Additionally, some research groups have achieved success in exploring methods for measuring the keyhole depth from the top surface using optical interferometry or inline coherent imaging (ICI). Combining the capabilities of these monitoring systems will be a crucial step towards implementing this prediction model in 3D printing systems.

In Chapter 5, we discussed how the rapid solidification induced by the keyhole fluctuations on solid-liquid interface can lead to solidification cracking. We demonstrated this through the RDG model, which showed the formation of a large local pressure drop due to fast solidification. A potential avenue for future research would be to conduct microstructural simulations during the LPBF additive manufacturing process to estimate the threshold pressure drop in the mushy zone at which cracking begins. This approach could provide valuable insights into the mechanisms behind solidification cracking and aid in the development of strategies to mitigate it.

Studying the relationship between solidification velocity at various locations within the melt pool and resulting microstructural variations could be an important research topic in the context of solidification dynamics. Additionally, investigating the impact of these microstructural variations on solidification cracking during the LPBF process would be a highly relevant and valuable research topic.

References

- [1] M. Mani, B.M. Lane, M.A. Donmez, S.C. Feng, S.P. Moylan, A review on measurement science needs for real-time control of additive manufacturing metal powder bed fusion processes, Int. J. Prod. Res. 55 (2017) 1400–1418.

 https://doi.org/10.1080/00207543.2016.1223378.
- [2] G. Vastola, Q.X. Pei, Y.W. Zhang, Predictive model for porosity in powder-bed fusion additive manufacturing at high beam energy regime, Addit. Manuf. 22 (2018) 817–822. https://doi.org/10.1016/j.addma.2018.05.042.
- [3] T. DebRoy, H.L. Wei, J.S. Zuback, T. Mukherjee, J.W. Elmer, J.O. Milewski, A.M. Beese, A. Wilson-Heid, A. De, W. Zhang, Additive manufacturing of metallic components process, structure and properties, Prog. Mater. Sci. 92 (2018) 112–224. https://doi.org/10.1016/j.pmatsci.2017.10.001.
- [4] W.J. Sames, F.A. List, S. Pannala, R.R. Dehoff, S.S. Babu, The metallurgy and processing science of metal additive manufacturing, Int. Mater. Rev. 61 (2016) 315–360.
- [5] D. Herzog, V. Seyda, E. Wycisk, C. Emmelmann, Additive manufacturing of metals, Acta Mater. 117 (2016) 371–392. https://doi.org/10.1016/j.actamat.2016.07.019.
- [6] T. DebRoy, T. Mukherjee, J.O. Milewski, J.W. Elmer, B. Ribic, J.J. Blecher, W. Zhang, Scientific, technological and economic issues in metal printing and their solutions, Nat. Mater. 18 (2019). https://doi.org/10.1038/s41563-019-0408-2.
- [7] C. Zhao, N.D. Parab, X. Li, K. Fezzaa, W. Tan, A.D. Rollett, T. Sun, Critical instability at moving keyhole tip generates porosity in laser melting, Science (80-.). 370 (2020) 1080– 1086. https://doi.org/10.1126/science.abd1587.
- [8] G. Kasperovich, J. Haubrich, J. Gussone, G. Requena, Correlation between porosity and processing parameters in TiAl6V4 produced by selective laser melting, Mater. Des. 105

- (2016) 160–170. https://doi.org/10.1016/j.matdes.2016.05.070.
- [9] N.T. Aboulkhair, N.M. Everitt, I. Ashcroft, C. Tuck, Reducing porosity in AlSi10Mg parts processed by selective laser melting, Addit. Manuf. 1 (2014) 77–86. https://doi.org/10.1016/j.addma.2014.08.001.
- [10] A. Bauereiß, T. Scharowsky, C. Körner, Defect generation and propagation mechanism during additive manufacturing by selective beam melting, J. Mater. Process. Technol. 214 (2014) 2497–2504. https://doi.org/10.1016/j.jmatprotec.2014.05.002.
- [11] S. Leuders, M. Thöne, A. Riemer, T. Niendorf, T. Tröster, H.A. Richard, H.J. Maier, On the mechanical behaviour of titanium alloy TiAl6V4 manufactured by selective laser melting: fatigue resistance and crack growth performance, Int. J. Fatigue. 48 (2013) 300–307. https://doi.org/10.1016/j.ijfatigue.2012.11.011.
- [12] A. Fatemi, R. Molaei, S. Sharifimehr, N. Phan, N. Shamsaei, Multiaxial fatigue behavior of wrought and additive manufactured Ti-6Al-4V including surface finish effect, Int. J. Fatigue. 100 (2017) 347–366. https://doi.org/10.1016/j.ijfatigue.2017.03.044.
- [13] S. Tammas-Williams, P.J. Withers, I. Todd, P.B. Prangnell, Porosity regrowth during heat treatment of hot isostatically pressed additively manufactured titanium components, Scr. Mater. 122 (2016) 72–76. https://doi.org/10.1016/j.scriptamat.2016.05.002.
- [14] R. Cunningham, A. Nicolas, J. Madsen, E. Fodran, E. Anagnostou, M.D. Sangid, A.D. Rollett, Analyzing the effects of powder and post-processing on porosity and properties of electron beam melted Ti-6Al-4V, Mater. Res. Lett. 5 (2017) 516–525. https://doi.org/10.1080/21663831.2017.1340911.
- [15] G. Kasperovich, J. Hausmann, Improvement of fatigue resistance and ductility of TiAl6V4 processed by selective laser melting, J. Mater. Process. Technol. 220 (2015) 202–214.

- https://doi.org/10.1016/j.jmatprotec.2015.01.025.
- [16] R. Cunningham, S.P. Narra, C. Montgomery, J. Beuth, A.D. Rollett, Synchrotron-based x-ray microtomography characterization of the effect of processing variables on porosity formation in laser power-bed additive manufacturing of Ti-6Al-4V, JOM. 69 (2017) 479–484. https://doi.org/10.1007/s11837-016-2234-1.
- [17] W.E. King, H.D. Barth, V.M. Castillo, G.F. Gallegos, J.W. Gibbs, D.E. Hahn, C. Kamath, A.M. Rubenchik, Observation of keyhole-mode laser melting in laser powder-bed fusion additive manufacturing, J. Mater. Process. Technol. 214 (2014) 2915–2925. https://doi.org/10.1016/j.jmatprotec.2014.06.005.
- [18] M. Bayat, A. Thanki, S. Mohanty, A. Witvrouw, S. Yang, J. Thorborg, N.S. Tiedje, J.H. Hattel, Keyhole-induced porosities in Laser-based Powder Bed Fusion (L-PBF) of Ti6Al4V: High-fidelity modelling and experimental validation, Addit. Manuf. 30 (2019) 100835. https://doi.org/10.1016/j.addma.2019.100835.
- [19] N.D. Parab, C. Zhao, R. Cunningham, L.I. Escano, K. Fezzaa, W. Everhart, A.D. Rollett, L. Chen, T. Sun, Ultrafast X-ray imaging of laser–metal additive manufacturing processes, J. Synchrotron Radiat. 25 (2018) 1467–1477. https://doi.org/10.1107/S1600577518009554.
- [20] Q. Guo, C. Zhao, L.I. Escano, Z. Young, L. Xiong, K. Fezzaa, W. Everhart, B. Brown, T. Sun, L. Chen, Transient dynamics of powder spattering in laser powder bed fusion additive manufacturing process revealed by in-situ high-speed high-energy x-ray imaging, Acta Mater. 151 (2018) 169–180. https://doi.org/10.1016/j.actamat.2018.03.036.
- [21] S.M.H. Hojjatzadeh, N.D. Parab, W. Yan, Q. Guo, L. Xiong, C. Zhao, M. Qu, L.I. Escano,
 X. Xiao, K. Fezzaa, W. Everhart, T. Sun, L. Chen, Pore elimination mechanisms during
 3D printing of metals, Nat. Commun. 10 (2019) 3088. https://doi.org/10.1038/s41467-019-

- 10973-9.
- [22] Q. Guo, C. Zhao, M. Qu, L. Xiong, S.M.H. Hojjatzadeh, L.I. Escano, N.D. Parab, K. Fezzaa, T. Sun, L. Chen, In-situ full-field mapping of melt flow dynamics in laser metal additive manufacturing, Addit. Manuf. 31 (2019) 100939.
 https://doi.org/10.1016/J.ADDMA.2019.100939.
- [23] C.L.A. Leung, S. Marussi, R.C. Atwood, M. Towrie, P.J. Withers, P.D. Lee, In situ X-ray imaging of defect and molten pool dynamics in laser additive manufacturing, Nat. Commun. 9 (2018) 1355. https://doi.org/10.1038/s41467-018-03734-7.
- [24] N.D. Parab, L. Xiong, Q. Guo, Z. Guo, C. Kirk, Y. Nie, X. Xiao, K. Fezzaa, W. Everheart, W.W. Chen, L. Chen, T. Sun, Investigation of dynamic fracture behavior of additively manufactured Al-10Si-Mg using high-speed synchrotron X-ray imaging, Addit. Manuf. 30 (2019) 100878. https://doi.org/10.1016/j.addma.2019.100878.
- [25] C. Zhao, K. Fezzaa, R.W. Cunningham, H. Wen, F. De Carlo, L. Chen, A.D. Rollett, T. Sun, Real-time monitoring of laser powder bed fusion process using high-speed X-ray imaging and diffraction, Sci. Rep. 7 (2017) 3602. https://doi.org/10.1038/s41598-017-03761-2.
- [26] A.A. Martin, N.P. Calta, J.A. Hammons, S.A. Khairallah, M.H. Nielsen, R.M. Shuttlesworth, N. Sinclair, M.J. Matthews, J.R. Jeffries, T.M. Willey, J.R.I. Lee, Ultrafast dynamics of laser-metal interactions in additive manufacturing alloys captured by in situ X-ray imaging, Mater. Today Adv. 1 (2019) 100002. https://doi.org/10.1016/j.mtadv.2019.01.001.
- [27] A.A. Martin, N.P. Calta, S.A. Khairallah, J. Wang, P.J. Depond, A.Y. Fong, V. Thampy, G.M. Guss, A.M. Kiss, K.H. Stone, C.J. Tassone, J. Nelson Weker, M.F. Toney, T. van Buuren, M.J. Matthews, Dynamics of pore formation during laser powder bed fusion

- additive manufacturing, Nat. Commun. 10 (2019) 1–10. https://doi.org/10.1038/s41467-019-10009-2.
- [28] R. Cunningham, C. Zhao, N. Parab, C. Kantzos, J. Pauza, K. Fezzaa, T. Sun, A.D. Rollett, Keyhole threshold and morphology in laser melting revealed by ultrahigh-speed x-ray imaging, Science (80-.). 363 (2019) 849–852.
 https://doi.org/10.1126/science.aav4687.
- [29] A. Bobel, L.G. Hector, I. Chelladurai, A.K. Sachdev, T. Brown, W.A. Poling, R. Kubic, B. Gould, C. Zhao, N. Parab, A. Greco, T. Sun, In situ synchrotron x-ray imaging of 4140 steel laser powder bed fusion, Materialia. 6 (2019) 100306.
 https://doi.org/10.1016/j.mtla.2019.100306.
- [30] C. Weingarten, D. Buchbinder, N. Pirch, W. Meiners, K. Wissenbach, R. Poprawe, Formation and reduction of hydrogen porosity during selective laser melting of AlSi10Mg, J. Mater. Process. Technol. 221 (2015) 112–120. https://doi.org/10.1016/j.jmatprotec.2015.02.013.
- [31] R. Clift, J.R. Grace, M.E. Weber, Bubbles, drops, and particles, Academic, New York, 1978.
- [32] S.A. Khairallah, A.T. Anderson, A. Rubenchik, W.E. King, Laser powder-bed fusion additive manufacturing: physics of complex melt flow and formation mechanisms of pores, spatter, and denudation zones, Acta Mater. 108 (2016) 36–45. https://doi.org/10.1016/j.actamat.2016.02.014.
- [33] S. Tammas-Williams, P.J. Withers, I. Todd, P.B. Prangnell, Porosity regrowth during heat treatment of hot isostatically pressed additively manufactured titanium components, Scr. Mater. 122 (2016) 72–76. https://doi.org/10.1016/j.scriptamat.2016.05.002.

- [34] Z. Ren, L. Gao, S.J. Clark, K. Fezzaa, P. Shevchenko, A. Choi, W. Everhart, A.D. Rollett, L. Chen, T. Sun, Machine learning-aided real-time detection of keyhole pore generation in laser powder bed fusion, Science. 379 (2023) 89–94.
 https://doi.org/10.1126/science.add4667.
- [35] S.C. Altıparmak, V.A. Yardley, Z. Shi, J. Lin, Challenges in additive manufacturing of high-strength aluminium alloys and current developments in hybrid additive manufacturing, Int. J. Light. Mater. Manuf. 4 (2021) 246–261. https://doi.org/10.1016/j.ijlmm.2020.12.004.
- [36] N. Wang, S. Mokadem, M. Rappaz, W. Kurz, Solidification cracking of superalloy singleand bi-crystals, Acta Mater. 52 (2004) 3173–3182. https://doi.org/10.1016/j.actamat.2004.03.047.
- [37] J.H. Martin, B.D. Yahata, J.M. Hundley, J.A. Mayer, T.A. Schaedler, T.M. Pollock, 3D printing of high-strength aluminium alloys, Nature. 549 (2017) 365–369. https://doi.org/10.1038/nature23894.
- [38] B. Mondal, T. Mukherjee, T. DebRoy, Crack free metal printing using physics informed machine learning, Acta Mater. 226 (2022) 117612. https://doi.org/10.1016/j.actamat.2021.117612.
- [39] Z. Smoqi, A. Gaikwad, B. Bevans, M.H. Kobir, J. Craig, A. Abul-Haj, A. Peralta, P. Rao, Monitoring and prediction of porosity in laser powder bed fusion using physics-informed meltpool signatures and machine learning, J. Mater. Process. Technol. 304 (2022) 117550. https://doi.org/10.1016/j.jmatprotec.2022.117550.
- [40] S.A. Shevchik, C. Kenel, C. Leinenbach, K. Wasmer, Acoustic emission for in situ quality monitoring in additive manufacturing using spectral convolutional neural networks, Addit. Manuf. 21 (2018) 598–604. https://doi.org/10.1016/j.addma.2017.11.012.

- [41] F.E. Pfefferkorn, N.A. Duffie, X. Li, M. Vadali, C. Ma, Improving surface finish in pulsed laser micro polishing using thermocapillary flow, CIRP Ann. Technol. 62 (2013) 203–206. https://doi.org/10.1016/j.cirp.2013.03.112.
- [42] R. Vilar, Laser cladding, J. Laser Appl. 11 (1999) 64–78.
- [43] J.L. Huang, N. Warnken, J.-C. Gebelin, M. Strangwood, R.C. Reed, On the mechanism of porosity formation during welding of titanium alloys, Acta Mater. 60 (2012) 3215–3225. https://doi.org/10.1016/j.actamat.2012.02.035.
- [44] P. Todeschini, G. Champier, F.H. Samuel, Production of Al-(12-25).wt % Si alloys by rapid solidification: melt spinning versus centrifugal atomization, J. Mater. Sci. 27 (1992) 3539–3551.
- [45] N. Zuber, The dynamics of vapor bubbles in nonuniform temperature fields, Int. J. Heat Mass Transf. 2 (1961) 83–98. https://doi.org/10.1016/0017-9310(61)90016-3.
- [46] T.J. Lin, K. Tsuchiya, L.S. Fan, Bubble flow characteristics in bubble columns at elevated pressure and temperature, AIChE J. 44 (1998) 545–560.
 https://doi.org/10.1002/aic.690440306.
- [47] Q. Guo, C. Zhao, M. Qu, L. Xiong, L.I. Escano, S.M.H. Hojjatzadeh, N.D. Parab, K. Fezzaa, W. Everhart, T. Sun, L. Chen, In-situ characterization and quantification of melt pool variation under constant input energy density in laser powder bed fusion additive manufacturing process, Addit. Manuf. 28 (2019) 600–609. https://doi.org/10.1016/j.addma.2019.04.021.
- [48] S.M.H. Hojjatzadeh, N.D. Parab, Q. Guo, M. Qu, L. Xiong, C. Zhao, L.I. Escano, K. Fezzaa, W. Everhart, T. Sun, L. Chen, Direct observation of pore formation mechanisms during LPBF additive manufacturing process and high energy density laser welding, Int.

- J. Mach. Tools Manuf. 153 (2020) 103555.https://doi.org/10.1016/j.ijmachtools.2020.103555.
- [49] C. Zhao, Q. Guo, X. Li, N. Parab, K. Fezzaa, W. Tan, L. Chen, T. Sun, Bulk-Explosion-Induced Metal Spattering during Laser Processing, Phys. Rev. X. 9 (2019) 21052. https://doi.org/10.1103/PhysRevX.9.021052.
- [50] H. Nakamura, Y. Kawahito, K. Nishimoto, S. Katayama, Elucidation of melt flows and spatter formation mechanisms during high power laser welding of pure titanium, J. Laser Appl. 27 (2015) 032012. https://doi.org/10.2351/1.4922383.
- [51] P. Lubin, H. Chanson, Are breaking waves, bores, surges and jumps the same flow?, Environ. Fluid Mech. 17 (2017) 47–77. https://doi.org/10.1007/s10652-016-9475-y.
- [52] P.A. Elmore, G.L. Chahine, H.N. Oguz, Cavity and flow measurements of reproducible bubble entrainment following drop impacts, Exp. Fluids. 31 (2001) 664–673. https://doi.org/10.1007/s003480100320.
- [53] P.J. Chiang, R. Jiang, R. Cunningham, N. Parab, C. Zhao, K. Fezzaa, T. Sun, A.D. Rollett, In Situ Characterization of Hot Cracking Using Dynamic X-Ray Radiography, in: J. Nakano, P.C. Pistorius, C. Tamerler, H. Yasuda, Z. Zhang, N. Dogan, W. Wang, N. Saito, B. Webler (Eds.), Miner. Met. Mater. Ser., Springer International Publishing, Cham, 2019: pp. 77–85. https://doi.org/10.1007/978-3-030-06143-2_8.
- [54] M. Miyagi, Y. Kawahito, H. Wang, H. Kawakami, T. Shoubu, M. Tsukamoto, X-ray phase contrast observation of solidification and hot crack propagation in laser spot welding of aluminum alloy, Opt. Express. 26 (2018) 22626. https://doi.org/10.1364/oe.26.022626.
- [55] M. Simonelli, C. Tuck, N.T. Aboulkhair, I. Maskery, I. Ashcroft, R.D. Wildman, R. Hague, A Study on the laser spatter and the oxidation reactions during selective laser melting of

- 316L stainless steel, Al-Si10-Mg, and Ti-6Al-4V, Metall. Mater. Trans. A. 46 (2015) 3842–3851. https://doi.org/10.1007/s11661-015-2882-8.
- [56] M. Tang, P.C. Pistorius, Oxides, porosity and fatigue performance of AlSi10Mg parts produced by selective laser melting, Int. J. Fatigue. 94 (2017) 192–201. https://doi.org/10.1016/j.ijfatigue.2016.06.002.
- [57] R. Manica, E. Klaseboer, D.Y.C. Chan, The hydrodynamics of bubble rise and impact with solid surfaces, Adv. Colloid Interface Sci. 235 (2016) 214–232. https://doi.org/10.1016/j.cis.2016.06.010.
- [58] E. Delnoij, F.A. Lammers, J.A.M. Kuipers, W.P.M. Van Swaaij, Dynamic simulation of dispersed gas-liquid two-phase flow using a discrete bubble model, Chem. Eng. Sci. 52 (1997) 1429–1458. https://doi.org/10.1016/S0009-2509(96)00515-5.
- [59] N.O. Young, J.S. Goldstein, M.J. Block, The motion of bubbles in a vertical temperature gradient, J. Fluid Mech. 6 (1959) 350. https://doi.org/10.1017/S0022112059000684.
- [60] H. Kobatake, J. Brillo, J. Schmitz, P.Y. Pichon, Surface tension of binary Al-Si liquid alloys, J. Mater. Sci. 50 (2015) 3351–3360. https://doi.org/10.1007/s10853-015-8883-6.
- [61] W. Yan, W. Ge, J. Smith, S. Lin, O.L. Kafka, F. Lin, W.K. Liu, Multi-scale modeling of electron beam melting of functionally graded materials, Acta Mater. 115 (2016) 403–412. https://doi.org/10.1016/j.actamat.2016.06.022.
- [62] W. Yan, W. Ge, Y. Qian, S. Lin, B. Zhou, W.K. Liu, F. Lin, G.J. Wagner, Multi-physics modeling of single/multiple-track defect mechanisms in electron beam selective melting, Acta Mater. 134 (2017) 324–333. https://doi.org/10.1016/j.actamat.2017.05.061.
- [63] W. Yan, S. Lin, O.L. Kafka, Y. Lian, C. Yu, Z. Liu, J. Yan, S. Wolff, H. Wu, E. Ndip-Agbor,M. Mozaffar, K. Ehmann, J. Cao, G.J. Wagner, W.K. Liu, Data-driven multi-scale multi-

- physics models to derive process–structure–property relationships for additive manufacturing, Comput. Mech. 61 (2018) 521–541. https://doi.org/10.1007/s00466-018-1539-z.
- [64] D. Gürsoy, F. De Carlo, X. Xiao, C. Jacobsen, TomoPy: A framework for the analysis of synchrotron tomographic data, J. Synchrotron Radiat. 21 (2014) 1188–1193. https://doi.org/10.1107/S1600577514013939.
- [65] E. Loth, Drag of non-spherical solid particles of regular and irregular shape, Powder Technol. 182 (2008) 342–353. https://doi.org/10.1016/j.powtec.2007.06.001.
- [66] L. Rapoport, M. Sullivan, C. Harrison, Radially ejected bubbles driven by thermocapillarity in equilibrated vapor-liquid mixtures, Langmuir. 33 (2017) 4435–4443. https://doi.org/10.1021/acs.langmuir.7b00628.
- [67] S.C. Hardy, The motion of bubbles in a vertical temperature gradient, J. Colloid Interface Sci. 69 (1979) 157–162. https://doi.org/https://doi.org/10.1016/0021-9797(79)90090-0.
- [68] N. Read, W. Wang, K. Essa, M.M. Attallah, Selective laser melting of AlSi10Mg alloy: Process optimisation and mechanical properties development, Mater. Des. 65 (2015) 417–424. https://doi.org/10.1016/j.matdes.2014.09.044.
- [69] L. Thijs, K. Kempen, J.P. Kruth, J. Van Humbeeck, Fine-structured aluminium products with controllable texture by selective laser melting of pre-alloyed AlSi10Mg powder, Acta Mater. 61 (2013) 1809–1819. https://doi.org/10.1016/j.actamat.2012.11.052.
- [70] L. zhi Wang, S. Wang, J. jiao Wu, Experimental investigation on densification behavior and surface roughness of AlSi10Mg powders produced by selective laser melting, Opt. Laser Technol. 96 (2017) 88–96. https://doi.org/10.1016/j.optlastec.2017.05.006.
- [71] imsegkmeans, K-means clustering based image segmentation, (n.d.).

- https://www.mathworks.com/help/images/ref/imsegkmeans.html.
- [72] C. Zhao, N.D. Parab, X. Li, K. Fezzaa, W. Tan, A.D. Rollett, T. Sun, Critical instability at moving keyhole tip generates porosity in laser melting, Science (80-.). 370 (2020) 1080– 1086. https://doi.org/10.1126/science.abd1587.
- [73] MATLAB, Find local maxima—MATLAB, (2021).
 https://www.mathworks.com/help/signal/ref/findpeaks.html.
- [74] M. Qu, Q. Guo, L.I. Escano, A. Nabaa, S.M.H. Hojjatzadeh, Z.A. Young, L. Chen, Controlling process instability for defect lean metal additive manufacturing, Nat. Commun. 13 (2022) 1–8. https://doi.org/10.1038/s41467-022-28649-2.
- [75] S.A. Khairallah, T. Sun, B.J. Simonds, Onset of periodic oscillations as a precursor of a transition to pore-generating turbulence in laser melting, Addit. Manuf. Lett. 1 (2021) 100002. https://doi.org/10.1016/j.addlet.2021.100002.
- [76] Y. Huang, T.G. Fleming, S.J. Clark, S. Marussi, K. Fezzaa, J. Thiyagalingam, C.L.A. Leung, P.D. Lee, Keyhole fluctuation and pore formation mechanisms during laser powder bed fusion additive manufacturing, Nat. Commun. 13 (2022) 1170. https://doi.org/10.1038/s41467-022-28694-x.
- [77] A. Sonawane, G. Roux, J.J. Blandin, A. Despres, G. Martin, Cracking mechanism and its sensitivity to processing conditions during laser powder bed fusion of a structural aluminum alloy, Materialia. 15 (2021) 100976. https://doi.org/10.1016/j.mtla.2020.100976.
- [78] D.G. Eskin, Suyitno, L. Katgerman, Mechanical properties in the semi-solid state and hot tearing of aluminium alloys, Prog. Mater. Sci. 49 (2004) 629–711. https://doi.org/10.1016/S0079-6425(03)00037-9.
- [79] F. Matsuda, H. Nakagawa, K. Nakata, O. Hitoshi, The VDR Cracking Test for

- Solidification Crack Susceptibility on Weld Metals and Its Application to Aluminium Alloys, Trans. JWRI. 8 (1979) 85–95.
- [80] N. Coniglio, C.E. Cross, Mechanisms for solidification crack initiation and growth in aluminum welding, Metall. Mater. Trans. A Phys. Metall. Mater. Sci. 40 (2009) 2718– 2728. https://doi.org/10.1007/s11661-009-9964-4.
- [81] N.N. Prokhorov, Resistance to hot tearing of cast metals during solidification, Russ. Cast. Prod. 2 (1962) 172–75.
- [82] M.R. Nasresfahani, B. Niroumand, A new criterion for prediction of hot tearing susceptibility of cast alloys, Metall. Mater. Trans. A Phys. Metall. Mater. Sci. 45 (2014) 3699–3702. https://doi.org/10.1007/s11661-014-2341-y.
- [83] M. Rappaz, J.M. Drezet, M. Gremaud, A new hot-tearing criterion, Metall. Mater. Trans. A Phys. Metall. Mater. Sci. 30 (1999) 449–455. https://doi.org/10.1007/s11661-999-0334-z.
- [84] S. Kou, A criterion for cracking during solidification, Acta Mater. 88 (2015) 366–374. https://doi.org/10.1016/j.actamat.2015.01.034.
- [85] T. Böllinghaus, H. Herold, C.E. Cross, J.C. Lippold, Hot cracking phenomena in welds II, 2008. https://doi.org/10.1007/978-3-540-78628-3.
- [86] J.M. Drezet, M.S.F. Lima, J.D. Wagnière, M. Rappaz, W. Kurz, Crack-free aluminium alloy welds using a twin laser process, Weld. World. 52 (2008) 87–94.
- [87] K. Chattopadhyay, A.P. Ramineni, P. Ramachandrarao, Estimation of cooling rates in rapid solidification from eutectic cell spacing, J. Mater. Sci. 15 (1980) 797–799. https://doi.org/10.1007/BF00551752.
- [88] N. Kouraytem, P.-J. Chiang, R. Jiang, C. Kantzos, J. Pauza, R. Cunningham, Z. Wu, G. Tang, N. Parab, C. Zhao, K. Fezzaa, T. Sun, A.D. Rollett, Solidification crack propagation

and morphology dependence on processing parameters in AA6061 from ultra-high-speed x-ray visualization, Addit. Manuf. 42 (2021) 101959. https://doi.org/10.1016/j.addma.2021.101959.

[89] P. Wei, Z. Wei, Z. Chen, Y. He, J. Du, Thermal behavior in single track during selective laser melting of AlSi10Mg powder, Appl. Phys. A. 123 (2017) 1–13. https://doi.org/10.1007/s00339-017-1194-9.

Appendices

Appendix A - Copyright Permissions

Chapter 3: includes materials previously published in [48]. The permissions for using those materials are displayed in Appendix Figure-1.



Direct observation of pore formation mechanisms during LPBF additive manufacturing process and high energy density laser welding

Author:

S. Mohammad H. Hojjatzadeh,Niranjan D. Parab,Qilin Guo,Minglei Qu,Lianghua Xiong,Cang Zhao,Luis I. Escano,Kamel Fezzaa,Wes Everhart,Tao Sun,Lianyi Chen

Publication: International Journal of Machine Tools and Manufacture

Publisher: Elsevier Date: June 2020

© 2020 Elsevier Ltd. All rights reserved.

Journal Author Rights

Please note that, as the author of this Elsevier article, you retain the right to include it in a thesis or dissertation, provided it is not published commercially. Permission is not required, but please ensure that you reference the journal as the original source. For more information on this and on your other retained rights, please visit: https://www.elsevier.com/about/our-business/policies/copyright#Author-rights

BACK CLOSE WINDOW

Appendix Figure-1. Copyright permission for the material of [44].

Appendix B – Extended Data

Appendix Table 1. Thermophysical properties of AlSi10Mg alloy [60,89].

Material property	Value	Unit	
Solidus temperature, T _s	830.15	K	
Liquidus temperature, <i>T</i> ∟	870.15	K	
Boiling temperature, T_b	2743	K	
Density, $ ho$	2680	kg m⁻³	
Temperature coefficient of surface tension, $\frac{\partial \sigma}{\partial T}$	-0.31×10^{-4}	$N m^{-1} K^{-1}$	
Surface tension at liquidus temperature, σ_L	0.824	$N m^{-1}$	
Latent heat of fusion, ΔH_f	389×10^{3}	J kg⁻¹	
Latent heat of vaporization, ΔH_{ν}	10700×10^3	J kg⁻¹	
Linear thermal expansion coefficient, α_L	23×10^{-6}	K ⁻¹	
Convective heat transfer coefficient, hc	82	$W m^{-2} K^{-1}$	
Radiation emissivity, ε	0.4		
Energy absorptivity, η	0.52		

Appendix Table 2. Temperature-dependent thermophysical properties of AlSi10Mg alloy [89].

Material property	Temperature (K)	Value
	875	0.0022
\';' '(D)	1000	0.00125
Viscosity, v (Pa s)	1450	0.0007
	1850	0.00058
	2250	0.00045
	2700	0.0004
	300	160
	400	160
	500	160
	600	160
	700	160
Thermal conductivity, k (W m ⁻¹ K ⁻¹)	830	110
	870	90
	1200	100
	1500	110
	1800	115
	2100	120
	300	900
	375	960
	575	1020
Specific heat, C_p (J kg ⁻¹ K ⁻¹)	775	1125
	940	1040
	960	1040
	1100	1075
	1562	1075